EES Catalysis

REVIEW ARTICLE

View Article Online
View Journal | View Issue

Cite this: *EES Catal.*, 2023, 1, 832

A chemist's guide to photoelectrode development for water splitting – the importance of molecular precursor design

Thom R. Harris-Lee, [ab] Frank Marken, [a] Cameron L. Bentley, [b] Jie Zhang *[b] and Andrew L. Johnson *[a]

Photoelectrochemical (PEC) water splitting is a promising method for generating green hydrogen as a solar fuel, overcoming the issues associated with unreliability and periodicity of renewable technologies. While research in this field is growing, there is a distinct gap between complex device development and fundamental synthesis of the individual materials. For optimal device fabrication we need materials scientists and engineers to create complex multicomponent photoelectrodes, but also inorganic chemists to design bespoke precursors tailored to produce highly efficient, specifically designed photoelectrode materials. The success of precursor design for semiconductors in fields such as microelectronics has proven the significant impact of the precursor, however, this approach has yet to be used extensively in device fabrication for PEC water splitting. This review acts as a guide towards bespoke precursor development for the fabrication of tailored thin films; particularly how to design the structure and composition of the precursor to promote and enhance the most desired properties, including solubility, volatility, and thermal decomposition. The key areas of focus for device design are outlined, including both single thin film performance and overall device modifications and additions to create a high-performance PEC water splitting electrode. There is a specific emphasis towards chemical vapour deposition techniques due to the suitability for scale-up and commercial application compared to alternatives, and importantly, the significant influence of the molecular precursor on the deposition, and hence its link to synthetic chemistry. We aim to direct more synthetic chemists towards the field of PEC water splitting, encouraging collaboration to connect these two areas and bring the target of a commercially and industrially viable PEC system ever closer.

Received 22nd July 2023,
Accepted 21st September 2023

DOI: 10.1039/d3ey00176h

rsc.li/eescatalysis

Broader context

Renewable technologies are contributing more towards global electricity production each year; however the intermittency and periodicity of renewable energy supply prevents these technologies from completely replacing fossil fuels unless a suitable method for energy storage is available. Storage of energy as hydrogen, one of the most promising fuels for the future, through coupling photovoltaics with electrolysis (PV–E) is the most technologically-ready green hydrogen production method, however the current technology relies on the use of high-cost crystalline silicon for light harvestings. Direct water splitting through photoelectrochemical catalysis (PEC) or photocatalysis (PC), which utilise low grade and hence low-cost semiconductors, is therefore seen as the ultimate target, however its low technological readiness level means research should focus on improving the overall device fabrication and optimisation process. One significant part of the fabrication process that is mostly ignored is the bespoke design of precursors to tailor towards desired thin film properties. This review acts as a guide towards how precursors can be specifically designed to make effective water splitting photoelectrodes from a molecular chemistry bottom-up approach, encouraging a more interdisciplinary method towards efficient PEC water splitting, and promoting collaboration and a greater involvement of inorganic chemists into this expanding and essential field of research.

1. The need for photoelectrode materials in the hydrogen economy

The urgent need to combat climate change and environmental pollution through the transition from fossil-based to renewable

[a] *Department of Chemistry, University of Bath, Claverton Down, Bath, BA2 7AY, UK. E-mail: chsalj@bath.ac.uk*
[b] *School of Chemistry, Monash University, Clayton, Vic 3800, Australia. E-mail: jie.zhang@monash.edu*

energy sources is more apparent than ever. However, while the use of renewables is at an all-time high, it is still dwarfed by the consumption of oil, coal, and natural gas.[1] The solar energy available for harnessing at the Earth's surface far surpasses the global energy demand,[2] however, it is not possible for solar energy to replace fossil fuels without viable methods of long-term energy storage. The intermittent and unreliable nature of solar power results in peak production and peak demand rarely being aligned, both on a short term (day/night cycle) and long term (seasonal) period. There is therefore an essential requirement to store excess energy, which can then be transported and conveniently converted back into electricity when demand exceeds production.

Batteries are an obvious candidate for storage given their high round-trip efficiencies and technological readiness level, but unfortunately are unsuited to long-term storage for large-scale energy production due to their high running costs, large required facility size, significant charge leakage over long time periods, and issues associated with the recycling of potentially toxic, explosive, and environmentally damaging elemental components at end of life.[3,4] Further, the cost of lithium-ion batteries, the current standard in battery technologies, is high and constantly increasing, with a predicted shortage of lithium and other transition metal constituents in the future.[5] Finally, the storage capacity of batteries is currently insufficient for large scale operations such as grid-level storage, as limitations are already commonly encountered in relatively small-scale operations such as the travel range of electric vehicles.[6]

The production of solar fuels represents an alternative storage method whereby energy is stored in chemical bonds, which can be converted back to electricity directly using a fuel cell.[7] Solar radiation can be converted directly into a solar fuel *via* photoelectrochemical (PEC) catalysis and photocatalysis (PC), or indirectly *via* photovoltaics coupled to electrolysis (PV–E). Direct conversion has the potential for greater efficiency due to lower material costs and intrinsic thermal management, however, it currently has a far lower technological readiness level.

Among the range of possible solar fuel options, hydrogen is the most promising for a fully sustainable system due to its large energy density by weight (142 MJ kg^{-1}, 3 times larger than gasoline),[8] sourcing from water, as well as many other potential feedstocks, and zero emissions at point of use, with oxygen and water the only by-products upon hydrogen generation and back conversion into electricity respectively.[9] However, despite its foremost energy density by weight compared to alternatives, hydrogen has the lowest energy density by volume of all common fuels, meaning storage and transport are challenging aspects for creating an economy that uses hydrogen as a fuel.[10] Comparisons between hydrogen and current standard fossil and biofuels for energy densities by weight and volume are shown in Fig. 1.

Industrial hydrogen production presently relies on fossil fuels *via* steam methane reforming due to the low cost per kg, in comparison to green hydrogen alternatives. It is therefore important to consider how PV–E, PEC, and PC methods can be made more economically efficient.[12] Certain PEC anode materials

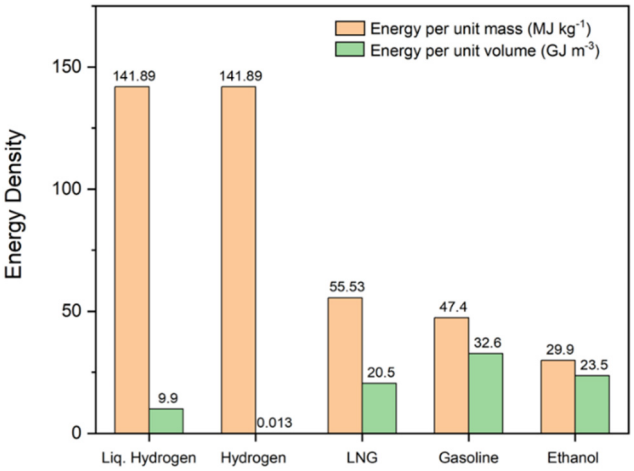

Fig. 1 Comparison between the energy density by weight and energy density by volume of hydrogen and common standard fuels. Data obtained from ref. 11.

can selectively oxidise a non-water/hydroxide species, while the cathode still evolves hydrogen, a common example of this being the oxidation of chloride ions to chlorine gas and hypochlorite ions, products used in disinfectant production.[13] Producing important commercial products required in large scales at both electrodes (rather than oxygen at the anode, as in conventional PEC water splitting) without increased equipment or running costs would further increase the economic viability of PEC,[14,15] and reduce the significant price gap between solar hydrogen production and fossil fuel methods.[12]

PEC water splitting is a multi-disciplinary topic that has been the subject of many reviews, ranging from in-depth studies of photoelectrode materials and properties, to the photophysical processes that occur, to political and socio-economic implementation strategies.[4,16–26] One major gap that has not been addressed is the nature of material fabrication, specifically the use of novel molecular precursors systematically designed for the deposition of designer PEC electrode materials. At present, it is commonplace to use readily available precursors that are not tailored for the deposition of PEC materials specifically. While some highly performing electrodes have been reported using this approach, there is also an abundance of poor or average performing electrodes, and the information gained towards future photoelectrode development from such an approach is limited. This review will discuss how to design bespoke molecular precursors for a systematic and informed approach to photoelectrode design, targeting both the structural precursor properties that promote effective use in deposition techniques, and the resulting deposited film properties that are known to enhance PEC performance.

2. Fundamental aspects of photoelectrodes

2.1 Photoelectrochemical water splitting

PEC devices split water in a two-step process: (1) photoabsorption followed by (2) redox catalysis. These steps can either both

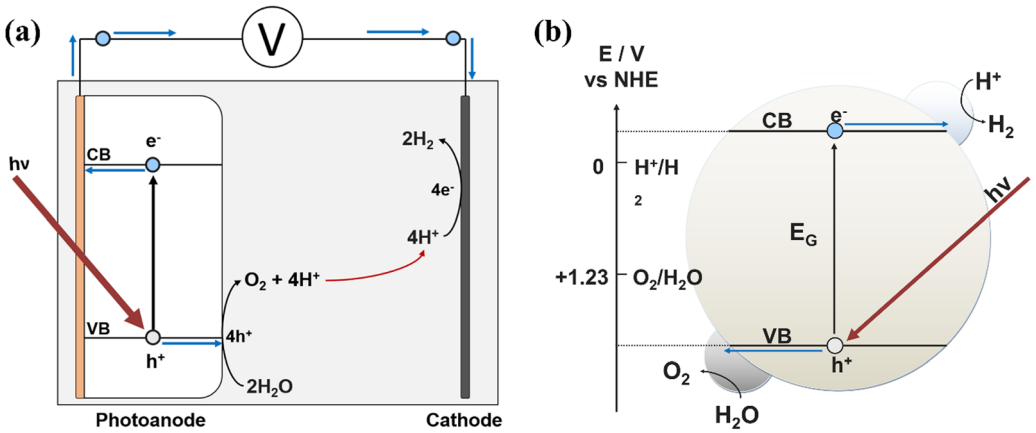

Fig. 2 Schematics depicting (a) a simple photoanode-based PEC device, and the redox processes occurring at each electrode after photon absorption, and (b) a PC nanoparticle with both HER and OER taking place, where $h\nu \geq E_G$.

occur in a single semiconducting material, or be split among different distinct materials deposited onto one another. A typical PEC setup (Fig. 2a) consists of an anode and a cathode, where either one or both will be photoactive. When sunlight is incident on a photoelectrode, photons with an energy equal to or greater than the bandgap of the material are absorbed, causing excitation of an electron (e^-) from the valence band (VB) into the conduction band (CB), leaving behind a hole (h^+). The electron and hole are still in a 'pair', each feeling the others attractive influence, favouring recombination to return to the lower energy state of electron in the VB. The time duration before this recombination event occurs is known as the excited state lifetime, which must be greater than the total time required for consumption of the charge carriers in the water splitting reaction, otherwise no charge carriers will be available for use in this redox process.[22,24,26–28]

To improve the efficiencies of charge carrier separation and interfacial charge transfer, a bias potential can be applied to the system. In a photoanode, the photoexcited electrons transport to the conductive back-contact where they leave the anode and flow to the cathode, while the holes diffuse to the electrode–electrolyte interface where they are consumed for use in oxidation reactions. Ideally, photo-water splitting would operate without the application of an external bias potential (*i.e.* a PC device), for example, using freely suspended semiconducting particles with loaded electrocatalysts that facilitate both the oxygen evolution reaction (OER) and hydrogen evolution reaction (HER) simultaneously from the photo-generated holes and electrons respectively, depicted in Fig. 2b. While developments in photoelectrodes for PEC are discussed herein, the methods could also apply to a PC device.

During water splitting, four photons are required for every oxygen molecule, and every two hydrogen molecules, evolved. The reactions taking place at each electrode are:

$$\text{Photoelectrode} \quad 4h\nu \rightarrow 4h^+ + 4e^- \tag{1}$$

$$\text{Anode} \quad 2H_2O + 4h^+ \rightarrow 4H^+ + O_2\uparrow \tag{2}$$

$$\text{Cathode} \quad 4H^+ + 4e^- \rightarrow 2H_2\uparrow \tag{3}$$

$$\text{Overall} \quad 2H_2O + 4h\nu \rightarrow O_2\uparrow + 2H_2\uparrow \tag{4}$$

The rate-limiting reaction in (photo)electrochemical water splitting is the OER, taking place at the anode, hence the focus of most PEC research is on developing high efficiency photoanodes.[29,30] In practical applications, both a photoanode and photocathode would be used in a tandem cell setup, where they can be placed on top of each other if one has a smaller bandgap and is transparent to greater energy photons, or parallel if they both absorb from the same wavelength of the solar spectrum, or both lack transparency to smaller wavelengths (Fig. 3).[4,31]

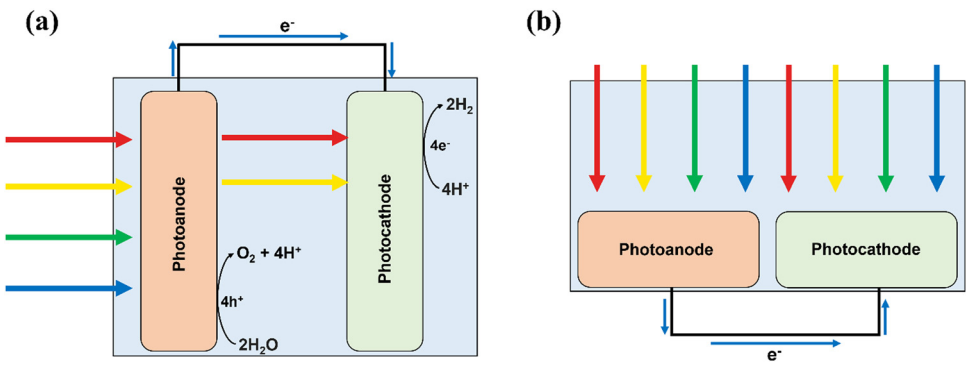

Fig. 3 Schematics showing PEC setups for (a) conventional tandem and (b) parallel configurations.

There are 5 main parameters that should be investigated to determine the efficiency of a PEC cell: (i) photon absorption; (ii) electron–hole pair separation; (iii) carrier diffusion/transport; (iv) catalytic efficiency; (v) mass transfer of reactant/product (*e.g.* the electrolyte ions, O_2 and H_2 gas *etc.*). The first 4 parameters all contribute towards the available charge carrier density, which is the abundance of charge carriers produced by the device that are available for use in water splitting.[21]

One major hurdle for PEC research is its difficulty in reproducibility due to the abundance of variables that can have significant impact on any of the parameters listed above, and hence the overall device activity and efficiency.[32] Research must, therefore, strictly control all variables that can be reasonably controlled (*e.g.* annealing conditions, accidental dopant/impurity addition, and synthesis/deposition protocols *etc.*) to reduce the impact of those that are more difficult to control.

2.2 Semiconductor energy bands

The detailed physics of how semiconductor bands function and behave is beyond the scope of this review, however, the most important fundamentals are covered, and for additional information the reader is directed to ref. 33–36.

The energy difference between the VB and CB (analogous to highest occupied molecular orbital (HOMO) and lowest unoccupied molecular orbital (LUMO) respectively for the case of a single molecule) must be smaller than or equal to the energy of an incident light photon to generate an electron–hole pair. In the solar spectrum at the Earth's surface, UV radiation (up to 380 nm, ~3.26 eV) makes up a maximum of 3.3%, compared to visible light (380–800 nm, 3.26–1.55 eV) which can reach values >35% on clear days.[21,37] Thus, even an electrode that absorbs up to 600 nm (2.07 eV) in the visible spectrum will still only be accessing 17.8% of the total incident radiation.[38]

Note that infrared radiation is generally not considered for absorption in PEC water splitting despite its >50% composition in the solar spectrum. This is because PEC water splitting requires a minimum bandgap of at least 1.23 eV, or more realistically of ~1.5 eV, to overcome the separation between the H^+/H_2 and O_2/H_2O redox potentials, which is not possible with infrared light.[39,40] In other words, for water splitting to occur on a single semiconducting material, the CB must be positioned more negatively than the H^+/H_2 reduction potential such that it will donate electrons to H^+ ions. Additionally, the VB must be positioned more positively than the O_2/H_2O potential for photogenerated holes in the semiconductor to oxidise H_2O.[26]

Fig. 4 presents cases where different semiconductors have band positions allowing (a) both HER and OER, (b) only HER, (c) only OER.[41] In the case where only one of the redox reactions can occur, it is possible for high performance electrocatalysts with a more suited energy level to be deposited onto the surface of the photocatalyst, thus separating the photoabsorption and electrocatalysis processes between two components of an overall photoelectrode (rather than a single semiconducting film providing both functions).[42,43] A photoelectrode material only requires band positions suitable for both OER and HER if it is to be used as both the photoanode and photocathode, or as a photocatalyst. If the semiconductor will only be used as a photoanode, it only needs a suitable valence band maxima (VBM) position, and similarly for a photocathode, only the conduction band minima (CBM) must be located at a suitable relative energetic position. The relative positions of the CBM and VBM are also important for heterojunction formation (Section 6.1).

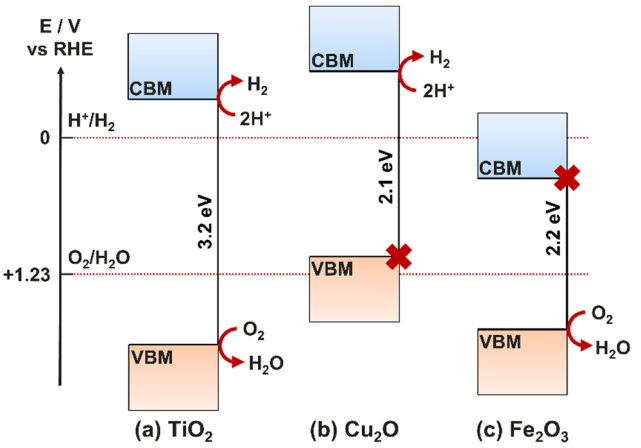

Fig. 4 Bandgap energy levels for three semiconductor examples at pH 0 relative to HER and OER redox potentials. (a) TiO_2 electrode: both HER and OER allowed, (b) Cu_2O electrode: HER allowed, OER forbidden, (c) Fe_2O_3 electrode: HER forbidden, OER allowed.

Bandgap size is one of the most significant influences on the PEC activity for a single material, for example, TiO_2 is one of the most promising semiconductors for water splitting applications, however, its large bandgap (3–3.2 eV) limits its use to multi-component devices, where photon absorption can be achieved through other semiconductor layers or sensitizers.[44] Tuning the bandgap is challenging, and can only reliably be achieved for a given material using dopants, which introduce dopant energy levels between the CB and VB of the bulk material, hence increasing the charge carrier density and decreasing the minimum energy required for exciton generation (Section 4.3). Combining multiple materials of different bandgaps in tandem is another effective method for increasing the efficiency of charge carrier generation, maximising photon absorption and minimising efficiency loss due to vibrational relaxation after high energy (relative to the band gap) electron excitations.[45]

Semiconductors can exist as either p-type or n-type depending on whether the majority charge carriers are holes or electrons, respectively. An excess of one charge carrier can be formed intrinsically by lattice vacancies, or extrinsically by substitution of lattice atoms with dopant atoms, hence p-type and n-type semiconductors can be manufactured by doping with atoms that act as electron acceptors or electron donors relative to the initial lattice. In silicon (Si) for example, n-type Si can be produced by substituting Si atoms in the lattice with phosphorous (P). The excess electron in each P atom will orbit the dopant atom with low binding energy such that it can be readily removed by thermal fluctuations and promoted to the CB to produce an

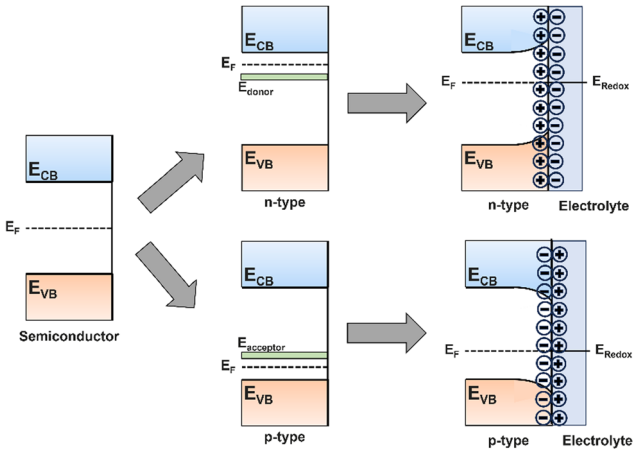

Fig. 5 Schematic showing the bandgap for a pure semiconductor, Fermi levels in n- and p-type semiconductors, and the origin of band bending when a semiconductor is put in contact with an electrolyte.

electron excess. The vacuum level of the dopant is therefore set as the CBM of the semiconductor, resulting in the donor ground state being positioned just below the CB (Fig. 5). The reverse is true to p-type Si, doping with a relatively electron deficient atom, such as aluminium, forms a dopant energy level at an energy above the VBM equal to the binding energy of the weakly bound orbiting hole, resulting in electron deficiency, or hole excess.[33,46]

So far, this section has assumed an isolated semiconductor, whereas in a real PEC system the semiconductor is in contact with an electrolyte, which itself has a specific redox potential (E_{redox}). In the case of 'flat bands' as described so far, the Fermi level (E_F), the energy at which there is a 50% probability of a state being occupied, is exactly halfway between the full VB and empty CB. In this case, when an electron–hole pair is generated by photon absorption, and no intrinsic electric field exists to drive carriers towards the semiconductor interface, rapid nonradiative recombination will occur, giving rise to no photocurrent. Upon immersion of the semiconductor in an electrolyte, the difference between E_F and E_{redox} results in a transfer of electrons across the interface, forming a depletion on one side and excess on the other – an electric field is formed within the near-surface region of the semiconductor, known as a space-charge region.

For n-type semiconductors, E_F will be greater than E_{redox}, hence electrons will transfer from higher to lower energy by injection from the semiconductor into the electrolyte, forming an electron depletion layer which forces an upward bending of the bands, decreasing E_F to the value of E_{redox} and forming an equilibrium (Fig. 5). The opposite is true for p-type semiconductors, where an electron accumulation layer will bend bands downwards. Now, when an electron–hole pair is generated within the space-charge region, the intrinsic electric field will drive the carriers either towards or away from the interface, promoting mobility and facilitating catalysis at the surface. Any carriers generated within the bulk of the semiconductor, unaffected by the space-charge field, will move slowly, by only diffusion due to the absence of any electric field influence, towards the electrolyte interface or conductive back contact.

The amount of band bending can be controlled through the application of a bias potential, which shifts the Fermi level. The band energy within the bulk of the semiconductor (outside the depletion region) can shift with applied potential, but the degree of band bending will vary to compensate for this shift, maintaining the same band edge positions relative to the redox potentials of the electrolyte. The application of a bias potential therefore increases the efficiencies of charge carrier separation and interfacial charge transfer, but does not alter the band gap or band edge positions.[36]

2.3 Performance indicators for photoelectrochemical cells

Quantitative PEC data is required for determining the relative performance of an electrode, and standard measurements allow for effective comparison between reports. This chapter covers the most essential benchmarking metrics to effectively evaluate PEC performance, requiring minimal specialist equipment or training. It should be noted that this chapter is aimed to introduce these techniques to any unfamiliar readers, and that for a complete study there are many more experiments that should be carried out, including (but not limited to) electrochemical impedance spectroscopy (EIS), Mott Schottky analysis, UV/Vis spectroscopy, and charge carrier quenching studies.

For detailed information on the design of an electrochemical setup should it be required, including choosing a suitable electrolyte, and counter and reference electrodes, the reader is directed towards the text by Chen *et al.*[47]

2.3.1 Photocurrent density. The most important and essential measurement for any PEC system is a photocurrent density (j_{photo}) *vs.* bias potential voltammogram (Fig. 6), recording the photocurrent density variations with increasing bias potential under chopped 1 sun AM 1.5G illumination (100 mW cm^{-2}). Chopping is required to reveal the dark background currents, as the current observed under constant irradiation must have the dark baseline subtracted to obtain the true photocurrent. Whatever the reference electrode used, during PEC water splitting it is customary to report the potential *versus* the reversible hydrogen electrode (RHE), converting using eqn (5):

$$E_{RHE} = E_{ref} + E_{ref\,vs.\,SHE} + 0.059\text{pH} \quad (5)$$

where E_{RHE} is the converted potential relative to the RHE, E_{ref} is the experimentally measured potential with respect to the reference electrode used, and $E_{ref\,vs.\,SHE}$ is the electrode potential of the reference electrode used with respect to the standard hydrogen electrode (SHE) at 25 °C, values for which can be readily found elsewhere.

Often, the intrinsic electric field from the space charge region is not sufficient to support carrier transport and interfacial charge transfer rates high enough for catalysis to occur before recombination. An external potential bias is applied to enhance both properties and support facile catalysis at the electrode surface. The onset potential (V_{on}), seen in a photocurrent density voltammogram as a current onset (Fig. 6a), is the minimum bias required to prevent generated charge carriers from complete recombination before surface catalysis, or other detrimental processes such as self-oxidation, occur.[36] In a tandem PEC system, the potentials at which

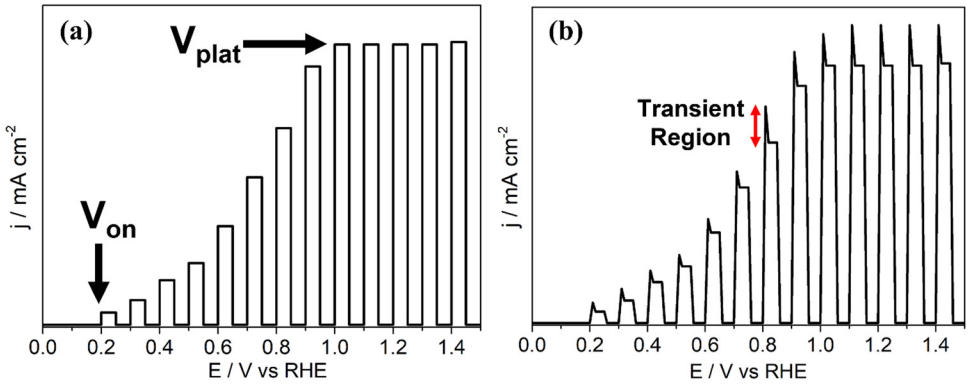

Fig. 6 Photocurrent density (j–V) graphs for example systems under chopped light showing (a) onset potential, V_{on}, and plateau potential, V_{plat}, (b) photocurrent transients.

HER and OER occur can overlap, in which instance V_{on} is the bias at which the photoanodic current (from OER) is equal in magnitude to the photocathodic current (from HER). In practice, V_{on} is a combination of the energy required for sufficient charge separation and interfacial transfer, and the intrinsic overpotential of the half reaction taking place at the electrode surface. After V_{on}, further increasing the bias improves electron–hole lifetimes and accelerates the rate of interfacial charge transfer, yielding greater photocurrents until the device is operating at maximum energetic efficiency and the current plateaus (V_{plat}, Fig. 6a). After reaching V_{plat}, j_{photo} is limited by carrier generation and/or the availability of the target species reaching active sites (*i.e.* mass transport in the electrolyte), and not charge carrier separation or surface electrocatalysis.

In practice, j_{photo}–V_{bias} voltammograms will have anodic and cathodic transients, observed as 'spikes' at each photocurrent onset corresponding to the light source being chopped on, as indicated in Fig. 6b. An anodic transient on a photoanode results from photogenerated holes becoming trapped in deep electronic energy levels due to the existence of detrimental surface states at the electrode–electrolyte interface, and/or defects in the bulk. Trapping of photogenerated carriers (in this case, holes) prevents recombination and hence allows a transient current to flow until all surface states are filled, after which charge recombination resumes as expected. When the illumination is stopped, these surface-trapped holes are discharged and reduced, resulting in a cathodic transient.[48] Larger transients are therefore an indication of the presence of a greater number of surface states (minimised by surface passivation and/or electrocatalyst loading, Section 4.2), and/or the presence of deep electronic traps in the bulk due to defect formation, either by design or intrinsically. In the latter case, these transients show the potential photocurrents that could be achieved if the traps were shallow instead of deep (*i.e.* charge carriers could be promoted and relaxed rapidly through them). Hence, observation of such phenomena using chopped light provides identification of the depth of traps produced, as discussed in Section 4.3.[49–51]

2.3.2 Efficiencies. The efficiency of the electrode in converting incident photons to oxygen and hydrogen gases is another key assessment, however, there are many different efficiencies that can be calculated.

Faradaic efficiency (FE). FE is a useful tool for identifying whether measured photocurrent is due to desired water splitting, or side reactions and/or photocorrosion. FE is expressed in eqn (6):

$$\mathrm{FE} = \frac{\text{Experimental Gas Evolution}}{\text{Theoretical Gas Evolution}} \tag{6}$$

where the theoretical gas evolution is calculated as the expected amount of O_2 evolved based on the charge passed, and the experimental gas evolution is the actual amount evolved determined using an accurate O_2 sensing technique.[25,47]

Incident photon to current conversion efficiency (IPCE). IPCE is a measure of the total photocurrent generated per unit incident photon flux as a function of the incident photon wavelength.[25,52] It provides an invaluable insight into how the material functions, combining efficiencies from photon absorption, charge transport from excitation point to electrode–electrolyte interface, and the efficiency of interfacial transfer. The main limitation of IPCE is that it requires the assumption of 100% FE, where all electrons measured as current are used in the water splitting reaction, with no losses to side-reactions or photocorrosion.[47] IPCE is expressed in eqn (7):

$$\mathrm{IPCE}(\lambda) = \frac{\left|j\,(\mathrm{mA\ cm^{-2}})\right| \times 1239.8\,(\mathrm{V\ nm})}{P_{\mathrm{mono}}\,(\mathrm{mW\ cm^{-2}}) \times \lambda\,(\mathrm{nm})} \tag{7}$$

where j is the measured photocurrent density, 1239.8 is h (Planck constant) multiplied by c (speed of light in a vacuum) in units of V nm, P_{mono} is the total power flux of the monochromatic light source, and λ is the wavelength of incident photons.

Solar to hydrogen conversion efficiency (STH). STH provides the 'truest' efficiency representation of the material, as it defines the efficiency with no applied bias potential and only when exposed to broadband AM 1.5G solar simulation (100 mW cm^{-2}); calculated as in eqn (8):

$$\mathrm{STH} = \left[\frac{r_{\mathrm{H_2}}\,(\mathrm{mmol\ H_2\ s^{-1}}) \times \Delta G_{298}\,(\mathrm{J\ mol^{-1}})}{P_{\mathrm{total}}\,(\mathrm{mW\ cm^{-2}}) \times A\,(\mathrm{cm^2})}\right]_{\mathrm{AM1.5G}} \tag{8}$$

where r_{H_2} is the rate of hydrogen production, ΔG_{298} is the change in Gibbs free energy per mole at 298 K, P_{total} is the total

solar incident power flux (commonly 100 mW cm^{-2}), and A is the illuminated photoelectrode area.[47,52]

2.3.3 Operational stability. However exceptional a photoelectrodes performance may be at the lab scale, it will not be commercially viable unless it remains both chemically and physically stable over a practical operational period. The most common stability issues result from: (i) photocorrosion due to self-oxidation or reduction, which can be prevented by improving the rate of charge carrier injection across the electrode–electrolyte interface, usually by electrocatalyst loading (see Section 4.5); (ii) (electro)chemical dissolution of the material or individual atoms within the lattice, which can be minimised by coating with a more stable material to act as a protective layer, or by implementing different bias potential and/or electrolyte conditions.[16,53–57] FE is a good indicator of whether the instability is due to photocorrosion (FE will be low as most carriers will be lost to parasitic self-redox reactions) or material dissolution, or both.

Photostability is typically measured *via* chronoamperometry of the photoanode while under constant illumination for prolonged periods. The measurement is usually run for 24–72 hours at lab scale, however, for more technologically ready electrodes that are targeting commercialisation, durations can be as long as 5000 hours.[47] These tests should be repeated at multiple biases, chosen as those that provide photocurrents expected within commercial PEC operation (1–10 mA cm^{-2}),[47] and re-characterisation of the electrode, both physically and photoelectrochemically, should be performed after each stability test.

3. Photoelectrode materials

There is an abundance of text already published that give in depth discussion of various materials for photoelectrodes,[4,57–61] hence only a brief outline of the most common and promising materials will be given here. A list of the materials discussed in this section, including their key properties, advantages, and limitations, is given in Table 1.

3.1 Photoanodes

Photoanodes are typically made from n-type metal oxide materials due to the positive position of the VB above the O_2/H_2O redox reaction potential, and the intrinsically high stability towards electrode oxidation. Here, the properties of four of the most common metal oxide photoanodes will be summarised.

3.1.1 TiO_2. The very first discovery of PEC water splitting was reported by Fujishima and Honda in 1972 using TiO_2 as a photoanode.[62] Since then, TiO_2 has remained a popular semiconductor option due to its number of desirable properties, including: (i) high photostability; (ii) low cost; (iii) non-toxicity; (iv) high catalytic activity; (v) suitable band edge positioning.[63–65] Using TiO_2 in conjunction with other materials with traits that lack in one or more of these areas also improves the viability of that material for PEC water splitting, achieving a decreased overall cost and increased stability of the composite electrode.[66]

Research has proven the ability to control the dimensionality of the TiO_2 nanostructure, with published syntheses for zero-dimensional (0D), one-dimensional (1D), two-dimensional (2D), and three-dimensional (3D) nanostructures. Of these, 0D and 1D are the more useful for application in PEC water splitting. 0D usually takes the form of quantum dots, used to decorate a photocatalyst and improve light absorption and carrier separation.[67] 1D usually takes the form of nanorods or nanotubes which feature high surface areas for redox catalysis to occur on as well as small distances for photoexcited carriers to reach the electrode–electrolyte interface.[68,69] The choice between nanotubes and nanorods will depend on the kinetics of the charge transport in the semiconductor and the efficiency of redox catalysis at the surface. If the device activity is limited by the number of carriers available for catalysis at the surface, then nanorods are the more effective morphology as there is more material for light absorption and hence more charge carrier generation. On the other hand, if the limitation is the rate at which reactants in the electrolyte can reach the active sites on the electrode, nanotubes are more effective as they have a far greater surface area with a greater number of available active sites.[70,71]

Table 1 A summary of the most common and promising current materials used in photoelectrodes for PEC water splitting

Material	Photoelectrode	E_g/eV	Key advantages	Key limitations
TiO_2	Photoanode	3.0–3.2	High stability, low cost, non-toxic, moderate carrier diffusion length	Large bandgap
α-Fe_2O_3	Photoanode	2.0–2.2	High stability, low cost, non-toxic, good bandgap	Short carrier diffusion length
Fe_2TiO_5	Photoanode	2.2	High stability, non-toxic, good bandgap, moderate carrier diffusion length	High temperature synthesis, often impure films
$BiVO_4$	Photoanode	2.4	High stability, non-toxic, good bandgap	High surface recombination, poor bulk carrier transport, requires pH control
WO_3	Photoanode	2.5	High stability (acidic pH), non-toxic, moderate bandgap	Poor surface/interfacial carrier transfer, poor stability in non-acidic pH
Cu_2O	Photoanode	2.0–2.1	Low cost, non-toxic, good bandgap	Poor photostability
SnS	Photocathode	1.1–1.3	Good bandgap, low cost, high carrier mobility	Secondary phases act as deep hole traps, poor stability
CdS	Photocathode	2.4	Good bandgap, low cost, high catalytic activity,	Toxic, poor photostability, rapid carrier recombination
ZnS	Photocathode	3.7	Good stability, low cost, non-toxic, good catalytic activity	Very large bandgap
Sb_2Se_3	Photocathode	1.2	Good bandgap, high bulk carrier mobility	Poor stability

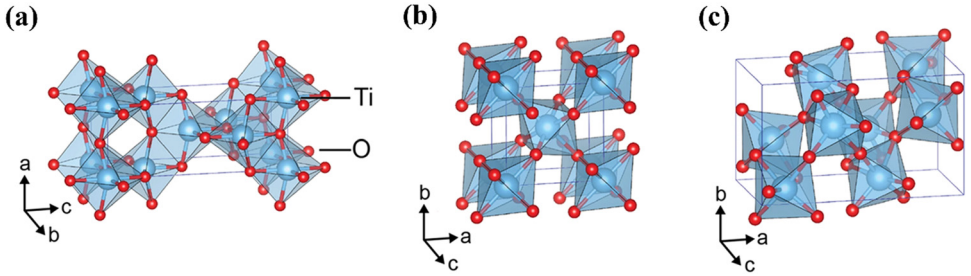

Fig. 7 Crystalline structures of TiO_2 in polymorphs (a) anatase, (b) rutile, (c) brookite. Reproduced with permission from ref. 76 copyright 2017, Nature Portfolio.

The main focus of TiO_2 research has been in two main areas, (1) tuning its large band gap (~3.2 eV, 387 nm), which limits its light absorption to the near-UV/UV regions of incident light, just 3.3–5.0% of all incident radiation,[21,37] (2) slowing down the rate of recombination of photogenerated electrons and holes to improve quantum efficiency.[72] Promising methods to enhance these properties in TiO_2 devices include annealing, nanostructuring, electrocatalyst loading, cation and anion doping, and heterojunction formation.[43,73]

Crystalline TiO_2 can exist in three phases, anatase, rutile, and brookite; crystalline structures for these polymorphs can be seen in Fig. 7. Rutile is the thermodynamically favoured structure and can be achieved directly in deposition or by heating the metastable anatase or brookite states at temperatures exceeding 600 °C.[74] All three phases are semiconducting, have band edges positioned suitably for both OER and HER, and have band gaps of 3.2 eV, 3.0 eV, and 3.2 eV for anatase, rutile and brookite, respectively. It is generally accepted that neither brookite nor amorphous-TiO_2 (a-TiO_2) are promising candidates for photocatalysis, and hence the discussions herein will focus on either anatase or rutile.[44] It is worth noting that anatase is considered the more photochemically active form of TiO_2, despite its greater bandgap than rutile.[75]

Pure TiO_2 is an n-type semiconductor because of intrinsic oxygen vacancies, which effectively serve as electron donor sites to reduce some of the Ti(IV) centres in the lattice to Ti(III) (Fig. 8). Such a reduction has been increased extrinsically by a range of techniques, including high pressure hydrogen treatment,[77] reduction using aluminium reducing agent,[78] and annealing under vacuum environment.[13] Acceptor doping (*e.g.* Cr^{3+}, Fe^{3+})[79,80] into TiO_2 can modify it into a p-type semiconductor for use as a photocathode. Naturally, this also adds additional dopant energy levels above the VB which serves to narrow the band gap (to absorb a wider photon range from the visible light spectrum) and improve the rate of charge transport inside the semiconductor.[81] Indeed, lowering the bandgap by doping, with either acceptor or donor dopants, has proven highly successful for the viability of TiO_2 in commercial photocatalysis, however, the most effective dopants are often noble metal ions which are too expensive and rare for large scale, sustainable production.[44] A promising alternative to noble metal usage is in sulfur-doped TiO_2, or similarly the combination of TiO_2 with metal sulfides, such as MoS_2 and WS_2, both options producing much cheaper, more abundant semiconductor devices with photochemical properties comparable to those using noble metal ions.[82,83]

3.1.2 α-Fe_2O_3. α-Fe_2O_3, or hematite, is a similar semiconductor to TiO_2 with respect to its high stability under a large pH range, non-toxicity, natural abundance, and low cost in both production and raw materials.[84] Unlike TiO_2 however, α-Fe_2O_3 possesses a narrower bandgap of 2.0–2.2 eV, allowing absorption of photons up to 620 nm – most of visible light.[19] Despite these ideal properties, the photochemical applications of α-Fe_2O_3 are restricted to OER, and limited by short hole diffusion lengths, 2–4 nm compared to >1 μm in TiO_2, resulting in rapid recombination of excited electron–hole pairs.[19,61] As such, α-Fe_2O_3 is usually deposited at low thicknesses to ensure that carriers can travel to interfaces on either side, but more intricate approaches to overcome this limitation have also been reported, including controlling deposition morphologies, doping, heterojunction formation, and use in hybrid materials.[85]

A promising hybrid material using both α-Fe_2O_3 and TiO_2 is Fe_2TiO_5 (iron titanate), retaining the advantages of each

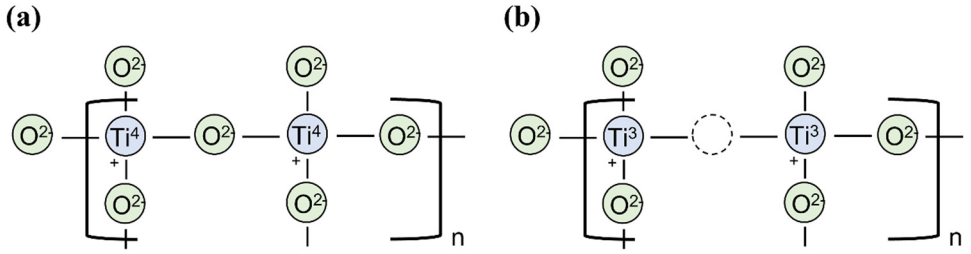

Fig. 8 (a) Defect free rutile TiO_2. (b) Intrinsic oxygen vacancy in rutile TiO_2 causing reduction of Ti^{4+} to Ti^{3+} in the lattice to conserve overall charge neutrality.

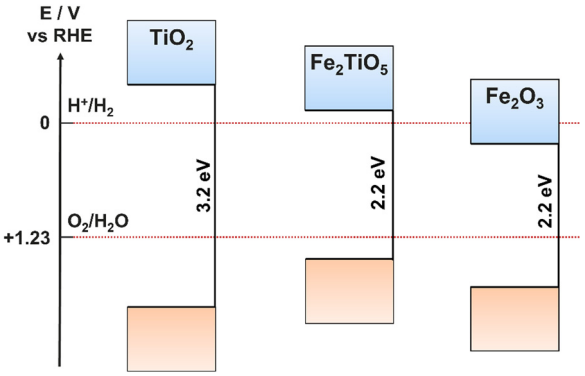

Fig. 9 Band positions for TiO_2, α-Fe_2O_3, and Fe_2TiO_5.

material, while also improving upon the limiting properties of each, such as the large band gap of TiO_2 (Fe_2TiO_5 has a much narrower bandgap of around 2.0–2.2 eV) and the poor charge carrier conductivity and diffusion lengths of α-Fe_2O_3.[86,87] In addition, the CB and VB positions of Fe_2TiO_5 are ideally placed to facilitate both HER and OER (Fig. 9).[88] Iron titanates are formed *via* solid state reactions between TiO_2 and α-Fe_2O_3, however, due to the similar metal ion sizes, films can be created by simultaneous, dual deposition of Ti and Fe oxides followed by thermal annealing, where the properties and structure are controlled by the relative concentrations of Fe and Ti ions.[88,89] The requirement for high temperature annealing can result in Fe_2TiO_5 films containing Fe and Ti oxide impurities.

3.1.3 $BiVO_4$. Ever since its first development in 1998 by Kudo *et al.*,[90] $BiVO_4$ has been another promising n-type photocatalyst candidate due in part to its stability and non-toxicity, particularly important when compared to alternative lead or cadmium based photocatalysts with similar yellow colouration, which are both toxic and susceptible to photo-corrosion.[91] Out of three potential polymorphs, only the monoclinic scheelite-like crystalline structure phase has been shown to be photochemically active, with a bandgap of around 2.4 eV ($\sim$517 nm),[61] as such the band positions of $BiVO_4$ only allow OER.

There are limitations to the viability of $BiVO_4$ photocatalysts, the first is that it cannot be run on its own in photocatalytic systems, or even for OER PEC catalysis at low potentials due to high surface recombination resulting in low IPCE values at lower biases.[91] The VO_4 octahedra that make up the $BiVO_4$ lattice result in poor carrier mobility, forcing hopping between octahedra instead of a constant motion through the lattice. Doping with W or Mo metals is considered essential in $BiVO_4$ to overcome this, substituting into the V sites, and distorting the octahedra to promote easier movement through the lattice.[92] $BiVO_4$ can also have a poor photocurrent stability due to the dissolution of V^{5+} on the surface, and the build-up of oxidation products at the anode surface which act as recombination centres. Decreases in photocurrent densities of up to 75% have been reported after just 30 minutes, highlighting the need to modify such electrodes or coat with protective layers.[93]

3.1.4 WO_3. WO_3 is often seen as an alternative to TiO_2, with a smaller bandgap of 2.5 eV (496 nm), moderate hole-diffusion length, and good stability, albeit only at acidic pH.[94] It also possesses a well-placed VB for water oxidation, but a CB more positive than the hydrogen evolution potential, making it suitable as a photoanode material only.[61] As a result of the smaller bandgap and greater photon absorption, the theoretical maximum STH of WO_3 is 4.8%, compared to just 2.2% for TiO_2.[95] However, WO_3 shows poor surface transfer kinetics, often seeing high overpotentials and losses to recombination. For this reason, WO_3 is mostly used for oxidation/degradation of organic species in the electrolyte, which can act as hole scavengers to limit the loss due to poor interfacial transfer kinetics.[96] A viable method for improving the surface transfer kinetics is by co-catalyst loading, however, since WO_3 is only stable at acidic pH, the chosen electrocatalyst must also be functional in highly acidic environments, limiting the available options significantly.[97] One alternative is using dual-function electrocatalyst coatings, for example, NiO_x/TiO_2 mixed phases where the NiO_x, a particularly effective catalyst in basic conditions, acts as the OER catalyst, while TiO_2 can stabilise WO_3 under basic conditions.[98]

3.2 Photocathodes

Photocathodes are a significant bottleneck in the development of an overall PEC device. The intrinsic electric field originating from the space charge region in p-type semiconductors make them suitable for proton reduction/hydrogen evolution, however, stability and photocorrosion is a ubiquitous issue across the range of potential candidates. It is well understood that PEC cells combining a photoanode with a complementary photocathode will lead to the highest theoretical efficiency, hence it is an issue that must be solved.[99] There is therefore great interest in both emerging photocathode materials that show good stability while still performing effectively, and in electrocatalysts and protective layers that can be coated onto the unstable materials to make them viable.

3.2.1 Cu_2O. Cu_2O, or cuprous oxide, is one of the main photocathode materials being studied due to its abundance, low cost, and non-toxicity. It possesses a favourable bandgap of $\sim$2.0–2.1 eV (590–620 nm) and has a large driving force for the hydrogen evolution reaction due to the CB positioning of -1.1 V *vs.* RHE at pH 0.[32,100] The significant issue with Cu_2O is the extensive photocorrosion that occurs upon light irradiation and electrolyte contact, owing to its self-reduction ($Cu_2O \rightarrow Cu$) and self-oxidation ($Cu_2O \rightarrow CuO$) potentials both being straddled by the CB and VB, Fig. 10).[54] Indeed, all Cu-based oxide photocathodes that have been studied as alternatives display similar issues with stability, including $CuFeO_2$,[101] $CuFe_2O_4$,[102] $CuAlO_2$,[103] $CuBi_2O_4$.[104]

Research on the optimisation of Cu_2O photoelectrodes has revealed multiple methods by which the extent of photocorrosion can be suppressed. The most common method, but also the method with the most breadth in variables to optimise, is to coat the electrode with a protective layer, often a hydrogen evolution catalyst such as MoS_x.[105] This has the added benefit of improving the surface charge transfer and reducing bulk recombination, as well as increasing stability. TiO_2 is another

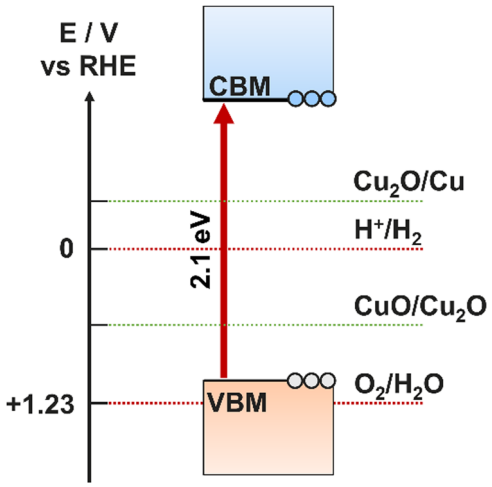

Fig. 10 Positions of CB and VB relative to self-oxidation and self-reduction potentials for a Cu_2O photocathode.

protective choice that has suitable band positions for p–n heterojunction formation, however, it requires complete coverage and good charge transfer, and therefore it is often used with another semiconductor to form a bi-layer coating the Cu_2O.[106,107] This method also requires the deposition of reduction cocatalysts to ensure the effectiveness of proton reduction is not lost in place of increased stability.[100]

3.2.2 Metal chalcogenides. Metal chalcogenides are promising photocathode materials, usually containing suitable bandgaps for PEC application, tuneable electronic structures, and are low cost and environmentally benign, however, they have common limitations of high sensitivity to air and moisture, and instability towards photocorrosion.[108,109] It is therefore common to couple metal chalcogenide electrodes with more stable materials, such as TiO_2, to improve both stability and charge separation.[110] SnS is used as a light harvesting layer in PV devices, with direct and indirect bandgaps of 1.3 and 1.1 eV respectively, making it an effective solar absorber.[111] The low bandgap requires its application in PEC to be restricted to advanced devices, used in conjunction with other semiconductors of higher bandgap to ensure high efficiency of visible-light absorption and energy utilisation. Low photocurrent performance compared to theoretical values can be linked to the formation of secondary Sn phases such as Sn_2S_3 and SnS_2, which act as detrimental deep trap sites.[112] Precursor design is particularly interesting for SnS films as the versatile Sn coordination chemistry, ranging from 2–9, allows for great flexibility in structures.[108] Charge transfer and transport have also been revealed to depend strongly on morphology, crystallinity, and phase for SnS materials, and literature over the past two decades has clearly shown that the most influential aspect of fabrication to control these properties for SnS is in suitable selection and design of starting precursors.[113–115]

CdS is generally considered a good photocatalyst material for PEC water splitting, possessing a bandgap of 2.4 eV with a suitably positioned CB for HER and VB for OER, and high catalytic activity, however, environmental concerns and rapid carrier recombination have limited its use.[116,117] It is often coupled with more stable materials such as ZnS, TiO_2, WO_3, and amorphous carbon to counteract its high photocorrosion, as well as form heterojunctions to minimise its intrinsically high recombination rates.[118,119] ZnS is like TiO_2 in that it is nontoxic, earth abundant, and shows good catalytic properties with suitable band edge positions for both OER and HER. However, its 3.70 eV bandgap is even greater than that of TiO_2, making it unsuitable for use without band structure engineering, for example, by doping, and combining/layering with lower band gap materials.[120]

Many reports have been looking at chalcogenide materials already extensively studied for use in PV systems and repurposing them for PEC photocathodes, including Sb_2Se_3, Cu_2BaSnS_4 (CBTS), Cu_2ZnSnS_4 (CZTS), and CuS_2. Due to the nature of PV requirements, all promising options have small bandgaps with CBM and VBM positioning only suitable for photocathodic use. The existing, well studied, and optimised multi-component PV devices based on these materials gives a good starting point for PEC photocathode development, often only requiring slight modifications with electrocatalyst or stability coatings.[4]

Sb_2Se_3 is an emerging material for use as a photocathode in PEC water splitting, with a small bandgap of ~1.2 eV facilitating absorption into the near-IR region, and good bulk carrier mobility.[121] It was first reported for PEC application in 2017, where it was used with n-type TiO_2 and Pt co-catalysts.[122] It can be seen from the use of anti-photocorrosion layers in most reports that stability is still an issue, however, after TiO_2-based protective layering, along with loading a Pt or RuO_x cocatalyst to ensure efficient HER catalysis can occur, water splitting performances are promising and stability is no longer an issue – unlike the Cu-based photocathodes which still show instability even after a protective coating.[123,124] A 2018 study by Malik *et al.* synthesised Sb_2Se_3 nanorods by both hot injection and aerosol-assisted chemical vapour deposition (AACVD) techniques using a novel single-source precursor (SSP), which showed high stability under simulated sunlight illumination for 10 minutes, longer than most Cu-based and chalcogenide photocathodes are stable for, however, longer durations would be required to assess long-term stability, and for comparison to photocathodes with protective layers.[125]

CBTS, CZTS, and binary sulfides such as CuS_2 are earth-abundant PV materials that have been investigated for photocathode application. Again, after slight modification from their use in PV, for example, Se incorporation into CBTS,[126] and deposition of buffer layers and TiO_2 protective overlayers,[127] current performances seem promising, although to date not competitive. Promisingly, the significant gap between current PEC performance and PV performance indicates that there is still lots of potential for performance enhancement within these materials.[128]

4. Design of important photoelectrode properties

Regardless of the electrode material, there are a range of important properties that need to be considered, improved,

and implemented to create a highly efficient photoelectrode. To effectively design a precursor, it is essential to understand these properties that should be targeted for improvement. Literature case studies outlining how precursors can be designed to control the properties discussed herein can be found throughout Section 5.

4.1 Charge carrier transport within the bulk

The first challenge faced by photogenerated charge carriers is successful transport through the bulk material to the relevant interface, usually either the semiconductor/electrolyte or semiconductor/back-contact interface, before recombination occurs. It is therefore crucial to study and control the bulk charge carrier mobility through a range of photoelectrode design techniques, as outlined herein. Doping and heterojunction formation are both effective and well-used approaches towards improving bulk transport, however, due to their versatile application towards engineering a range of different electrode material properties other than this, they are instead discussed in greater detail in Sections 4.3 and 6.1, respectively.

4.1.1 Morphology. The shape of a materials nanostructure can shorten the carrier transport path without sacrificing overall film thickness, which would result in less semiconductor to absorb photons, and hence reduced charge carrier generation.[129] For examples, morphologies such as quasi 1D nanotubes and nanorods, or spherical arrays instead of flat films, will favour faster carrier transport to the nearest interfacial point because of the shorter distance from generation point to interface, leading to less performance loss due to recombination while maintaining sufficient bulk material for efficient light absorption.[130,131] Interestingly, the total absorption will actually be greater in these nanostructures than in similarly thick flat films, as they are shaped to re-absorb scattered light from a previous incidence (Fig. 11).[132] Such morphologies therefore result in increased charge carrier generation through photon absorption, as well as less recombination of charge carriers due to shorter required transport distances.[133] Controlling morphology through molecular precursor design is discussed in Section 5.6.

4.1.2 Crystallographic planes and directions. The anisotropic property of semiconductors has a significant impact on the charge separation within a photoelectrode, with different predominant bulk crystal orientations facilitating different charge carrier mobilities.[134] Han *et al.* reported a 16-fold increase in measured photocurrent using a $BiVO_4$ photoanode with preferential ordered growth of [010] orientation and exposed (001) facets, compared to random growth.[135] Not only did this reveal the preferential charge mobility within the [010] direction for $BiVO_4$, and the high OER activity of (001) facets, the disproportionately increased [010] photocurrent identified the importance of ordered systems with the same preferential growth orientation of grains for charge movement, compared to more random systems. Li *et al.* observed electrons and holes favouring different facets within the same $BiVO_4$ electrode, facilitating more effective separation as they transport through the bulk to different surface locations.[136] This phenomenon is not restricted to $BiVO_4$, having also been reported for other semiconductors including TiO_2. Considering the previous discussion, it is important that in engineering different surface facets, the bulk material remains all the same orientation, or has distinct separation between orientation regions.

In TiO_2, exposed (101) and (010) facets are usually considered as the most photoactive, due to the increased number of uncoordinated atoms at the surface,[137,138] or the abundance of 100% coordinated Ti_{5c} atoms at the surface which can more efficiently transfer charge carriers, reducing recombination.[139] While certain precursors and deposition procedures can produce films with a high abundance of desired facets directly due to the deposition and growth mechanisms, it is difficult to evaluate this before deposition trials. For a deliberate facet engineering, two techniques can be used: additive addition and templating.

Additives in the precursor solution can interact with either the precursor or the nanocrystals during growth, altering the crystallite shape and the exposed facets.[140] The additives chosen must not remain after deposition, either through removal during the deposition process, or by thermal annealing post-deposition. Murray *et al.* was able to enhance and control the abundance of the (001) facet in TiO_2 nanocrystals using TiF_4 precursor with oleic acid and cosurfactant additives to produce HF *in situ*, which selectively binds to the (001) facet, preventing termination and maintaining exposure during continuing crystal growth.[138] With the use of different cosurfactants and the introduction of a percentage of $TiCl_4$ instead of TiF_4, the amount of facet exposure could be controlled, as well as the resulting overall crystal morphology.

Templating is another common method for controlling the shape of nanostructure during deposition,[141,142] however, it can also be used to selectively grow specific crystal facets. Zhou *et al.* demonstrated the use of a salt template to grow specific planes of transition metal phosphines (TMPs) due to the lattice matching between the salt crystals exposed facets and the grown TMP planes.[143,144] Theoretically, any preferred material orientation can be grown provided a suitable template with lattice matching exposed planes, however, it may limit other morphological requirements such as shape and surface area. Templating and additives also add additional material costs and fabrication steps to photoelectrode synthesis, hence achieving similar effects through bespoke precursor design would be advantageous for scale-up application.

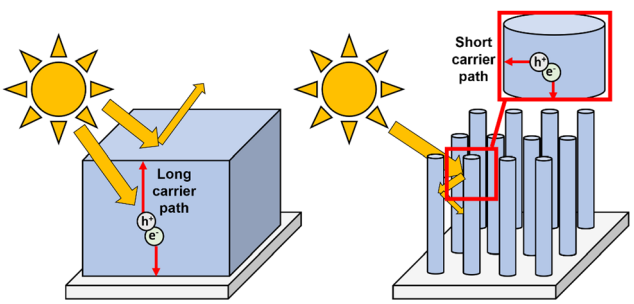

Fig. 11 Schematic comparisons of light trapping and carrier diffusion distances in a flat film *versus* nanorods.

4.1.3 Grain boundaries. The interconnect between crystallites within a material, known as grain boundaries, can dominate the optical and electronic properties of a device, hence it is essential to understand and consider when designing a thin film, even if the exact control and behaviour of the boundaries is still not clear. This is even more important for monolayers or ultra-thin films which are dominated by grain-effects.[145,146] Grain boundaries introduce traps within the film, however, simulations have shown that these energy traps have minimal impact on mobility, and instead charge transfer is hindered by energy barriers created due to misalignment of the meeting crystallites.[145]

Carrier mobility between grains is correlated to how intimately connected neighbouring grains are, hence a sample with a larger range of different grain sizes can often form stronger connections and therefore show greater transport properties; however, this can also increase the density of grains, introducing more energy barriers to move through and also increasing charge mobility degradation rates due to greater diffusion of ambient species into the film, which can then act as energy traps.[147–149] Mixed phase films, like anatase–rutile TiO_2, will likely contain different sized grains due to the differing growth rates and mechanism of each phase, hence often showing increased bulk charge mobility due to the resulting formation of more intimate contacts.[150] Grain sizes can be controlled by the decomposition rate of the precursor molecules, but also by deposition (see Section 5.1.3) and annealing conditions.

4.2 Charge carrier transfer at surfaces

Surface charge utilization is as important as bulk charge behaviour, as poor interfacial transfer will result in significant efficiency losses through carrier recombination.

4.2.1 Surface area. The charge carrier excitation, separation, and interfacial transfer properties of a material are all critical steps to optimise in PEC electrodes, however, enhancing these areas is futile if the number of active sites at the electrode surface is too few to utilise all of the charge carriers that are available for redox.[4] To prevent wasting these active carriers (through recombination, side reactions, or self-oxidation/reduction), and hence increase the device efficiency, a high surface area nanostructure is key. This ensures that the device performance is dependent on the photonic and electronic properties of the material(s) itself, which can be modified and improved, rather than the lack of active surface sites causing a backlog of carriers that can then be lost to recombination.

The porosity is also important to consider. While a more porous material will have a greater surface area and thus higher efficiency, it is important to note that a performance decrease with time for materials with extreme porosity may be seen, as solution ions around active sites are consumed but cannot be replenished due to the difficulty of transport through the pores (*i.e.*, mass transport limitations). Nanostructures such as nanorods/nanotubes are among the most promising due to their high surface area, as well as ordered perpendicular growth relative to the substrate surface allowing for easy transport between the solution bulk and the base of the pores.[151] Ordered growth can also allow for more control over active areas of the crystal, increasing the exposure of specific facets.

4.2.2 Surface passivation and co-catalyst loading. Surface, or interface, passivation involves the deposition of a passivating material onto the photoelectrode, usually by atomic layer deposition (ALD), electrodeposition, or photodeposition. ALD is the most specialised technique, providing a highly controllable conformal coating over the photoelectrode surface while maintaining the underlying morphology, as well as being suitable for scale-up. Usefully, photodeposition deposits passivating material at the most photoelectrochemically active areas, by nature of the technique, hence ensuring passivation of the most important surface sites.

There are four photoanode properties that can be improved using passivating layers: (i) increased stability, preventing photocorrosion by increasing the speed of charge transport and removal from the electrode material to the passivating layer or solution. Chemical dissolution from instability of the electrode material in aqueous solution can also be eliminated by coating with a protective layer of highly chemically stable semiconductor, common examples being TiO_2 and WO_3.[53] (ii) Minimised surface state charge trapping, and therefore recombination, due to non-empty surface states acting as photogenerated hole traps. This phenomenon is caused by defects, dopants, and vacancies at the surface, hence deposition of a passivating layer eliminates charge traps at the electrode–electrolyte interface.[152,153] Use of a passivating layer also prevents the need for high temperature annealing to remove these states, which is known to negatively alter morphologies and material phases/polymorphs.[154] (iii) Decreased charge accumulation at the back contact, usually caused by poor band alignments between the photoanode and the back contact.[155] A thin passivating layer with a very negative VB at this interface also blocks hole backflow, a phenomenon where both holes and electrons are injected into the highly conductive back contact, so recombination can readily occur.[156] (iv) Manipulated interfacial energies; layering semiconductors with suitable bandgaps can lead to improved charge transfer throughout the device due to band bending facilitating more favoured transfers of carriers between materials.[42,157–159]

Alternatively (or in addition) to passivating layers, co-catalyst loading is a common method for enhancing surface charge utilization. OER and HER kinetics are improved by surface-bound electrocatalysts through reduction of the interfacial charge injection overpotential. The highest performing electrocatalysts are noble metals (Pt,[160,161] Pd,[162] Ru,[163,164] Rh,[165] Au,[166] Ag[167]) and noble metal oxides (RuO_2,[168,169] IrO_2[170]), however, due to their high costs and rarity, extensive research is aimed at finding alternatives to facilitate more viable commercialisation and scale-up, including materials such as transition metal phosphides[171–173] and oxyhydroxides.[174,175] Complex, multicomponent catalysts are emerging as highly efficient multi-functional systems, where the range of species present facilitates use in both HER and OER, a particularly useful trait for PC devices.[176]

There is a wide range of techniques used for co-catalyst deposition, including electrodeposition,[173,177] photodeposition,[178]

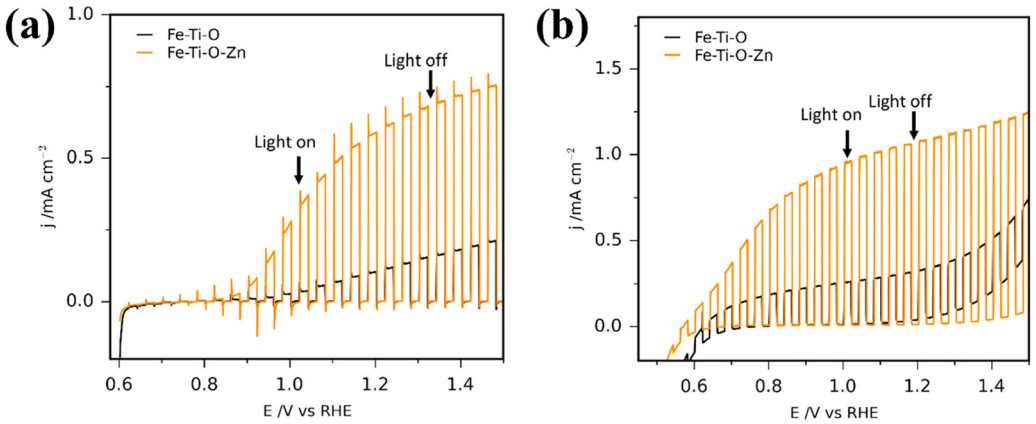

Fig. 12 Photocurrent density plots for Fe_2TiO_5 and Zn-doped Fe_2TiO_5 photoanodes (a) without hole quencher present, (b) with 10% H_2O_2 in the solution. Reproduced with permission from ref. 179 copyright 2020, American Chemical Society.

ALD,[56] hydrothermal,[83] and precipitation.[172] Co-catalysts with complementary band structure to the photoanode can also enhance charge carrier transport and separation throughout the device in the same way as discussed for passivating layers, acting as a heterojunction, and if the electrocatalyst is coated across the entire surface, or by photodeposition to cover the photoactive sites, stability can also be increased.[87] A rudimentary test for the photocurrent difference with and without an electrocatalyst can be achieved by running a linear sweep voltammetry measurement under chopped illumination before and after addition of a hole quencher (*e.g.* H_2O_2) into the electrolyte (Fig. 12). The difference in measured photocurrent can be correlated to the photocurrent loss due to poor surface charge transfer kinetics.[179]

4.3 Point defects – dopants and vacancies

The introduction of dopants into a semiconductor is one of the most powerful tools for improving and controlling the properties of a film. The substitution of an anion or cation dopant into the lattice can have a variety of impacts, particularly towards the band gap and charge carrier lifetimes. It is impossible to make a real semiconductor without some level of doping due to contamination during deposition processes, or the formation of vacancies (which can be seen as a form of dopant) due to fabrication conditions or non-perfect crystal growth. Understanding their impact, and how to choose dopants, is therefore essential for PEC device development. To achieve the desired doping, molecular precursors must be designed with compatible properties for use in co-depositions, or, alternatively, effective single-source precursors must be designed and synthesised (see Section 5.3). Post-treatment, such as annealing in hydrogen or vacuum environments, can also be used to create vacancies (see Section 6.2).

Dopants will narrow the bandgap through the introduction of dopant energy levels between the CB and VB of the bulk material, reducing the photon energy required for electron promotion, increasing the charge carrier density, and bringing the Fermi level closer to the valence (p-type doping) or conduction (n-type doping) band.[180] These dopant energy levels can form trapping sites, but whether these are good or bad depends

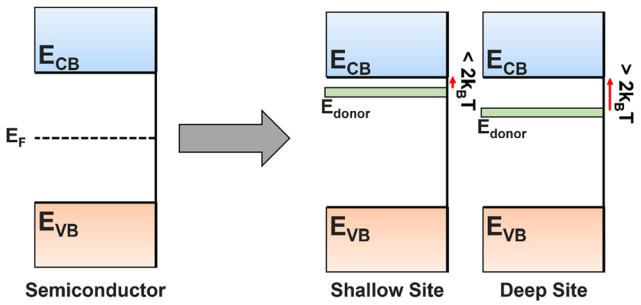

Fig. 13 Energy level diagram for a perfect, non-doped semiconductor, and n-type semiconductors with shallow trapping sites or deep trapping sites.

on the depth of the energy level (Fig. 13). A shallow trapping site (within $\sim 2k_BT$ of bulk energy level) allows fast excitation into and out of the sites, still maintaining overall carrier flow but dynamically separating carriers to prevent recombination, therefore increasing the diffusion distance, but not speed. Alternatively, deep trap sites ($>2k_BT$ from the transport level) can be detrimental, permanently trapping carriers and removing potential catalytic species, while also forming a potential barrier that slows other charges due to Coulomb repulsion.[145,181] It is often difficult to determine the depth of a trapping site before addition of a dopant into a previously unstudied system, so it is common to see reported a range of dopant species tested for a single film, some of which improve the performance and some of which worsen. As discussed in Section 2.3.1, deep traps are visible in *j–V* curves as cathodic and/or anodic transients.

Dopants can also increase the bulk charge transport and conductivity of a deposit by distorting the lattice structure or generating intrinsic electric fields. Monoclinic $BiVO_4$, for example, is well known to have poor bulk transport properties owing to its VO_4 octahedra-based lattice, requiring charge carriers to make distinct, slow hops when travelling through bulk material. By doping with W, V sites in affected octahedra are replaced by W atoms, which distort the lattice geometry and allow more continuous, faster carrier diffusion.[92,182,183]

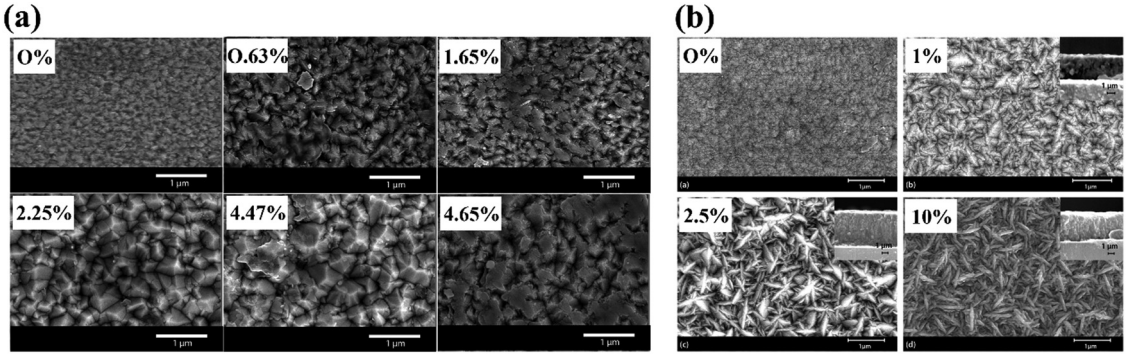

Fig. 14 Morphological changes reported for TiO_2 films after doping with varying concentrations of (a) W, reproduced with permission from ref. 184 copyright 2015, Nature Portfolio, (b) Sb, reproduced with permission from ref. 185 copyright 2017, Royal Society of Chemistry.

If the dopant species resides near to the photoelectrode–electrolyte interface, it can increase the interfacial catalytic activity. This is a good method for increasing catalytic efficiency without needing an additional catalyst loading step in the device fabrication process. Selectivity towards which species is oxidised/reduced can also change dependent on the dopant. For example, in TiO_2, oxygen vacancies can be formed by reductive annealing, acting as 2-electron donors which reduce Ti^{4+} in the lattice to Ti^{3+}. The Ti^{3+} at the surface is both more catalytically active than Ti^{4+}, and has a selectivity towards chloride oxidation over hydroxide, as shown in work by Marken *et al.* where TiO_2 in a solution of KCl was inactive to chloride oxidation before vacuum annealing, but active after.[13,151]

Finally, the film morphology can be altered due to the impact of dopant precursor presence on the film growth mechanisms (Fig. 14). Sathasivam *et al.* reported a morphological switch from an array of compact domes to a pyramidal featured thin film after doping TiO_2 with W in an AACVD process, achieved by the inclusion of a $W(OEt)_6$ precursor into the initial precursor solution.[184] Parkin *et al.* reported a similar change upon antimony doping, again by AACVD, where the pyramidal TiO_2 became a mixed pyramidal-needle morphology, increasing in the amount and prominence of the needle-like features with increasing percentage of Sb doping.[185]

4.4 Polymorph composition

The polymorph of a semiconductor will have considerable influence over the PEC properties it exhibits, including different band gaps, band edge positions, catalytic activities, charge mobilities, and stability. The easiest method to ensure only a single phase is present is by annealing at a temperature high enough such that all the material will be converted to the most thermodynamically favoured phase, for TiO_2 for example, a temperature above 600 °C will ensure complete conversion to rutile, except in rare cases.[186] To obtain a non-thermodynamically stable phase, precursor design and deposition parameters must be used to control the deposition, covered in greater detail in Section 5.5.

It is possible to create a mixture of two or more polymorphs in an as-deposited material, for example, anatase and rutile phases in TiO_2 films, which can modify the properties of the electrode significantly depending on the relative ratios of phases, the properties of each phase, and how compatible the phases are with each other. The possible benefits of mixed phases include: (i) the combination of best properties of each material (if one phase is better at light absorption and the other better at charge carrier transport, for example); (ii) different band gaps enhancing light absorption efficiency; (iii) aligned band positions forming an intrinsic electric field for enhanced charge separation.[74,92,187] It is known that an anatase–rutile mixed phase TiO_2 electrode consistently shows greater PEC performance than equivalent single-phase electrodes.[150,188] Alternatively, multi-phase materials can be detrimental, particularly if one of the phases is inactive or has poor light absorption or carrier transport properties. A greater transport resistance in highly dispersed phases can also occur because of increased hopping between. Unsuitable band alignments that drive electrons and holes to the same material will also increase carrier losses through recombination.

4.5 Photostability and photocorrosion

A common occurrence on PEC electrodes is self-oxidation and self-reduction, also known as photocorrosion, a side effect of generating free charge carriers that are available to oxidise/reduce the electrode material itself in addition to targeted ions in solution.[16] For self-oxidation to occur, the electrode must have an oxidation potential less positive than its VBM, and equivalently for self-reduction the reduction potential must be more positive than the CBM.[189] It is therefore possible for only oxidation or reduction to occur, both, or neither on a single semiconductor. Examples for TiO_2, Cu_2O, and Fe_2O_3 are illustrated in Fig. 15, showing that all three are theoretically susceptible to oxidative photocorrosion, while Cu_2O can also experience reductive photocorrosion.

Photocorrosion can be avoided if the reaction time for oxidation/reduction of the semiconductor is greater than the duration for complete charge carrier removal, therefore using co-catalysts is an effective approach for indirectly increasing material stability. Improved redox kinetics for the transfer of photogenerated charge carriers across the semiconductor–electrolyte interface results in faster removal of the oxidising/reducing species, therefore suppressing photocorrosion and increasing the life and activity of the device.[190] Additionally, co-catalysts inhibit the back

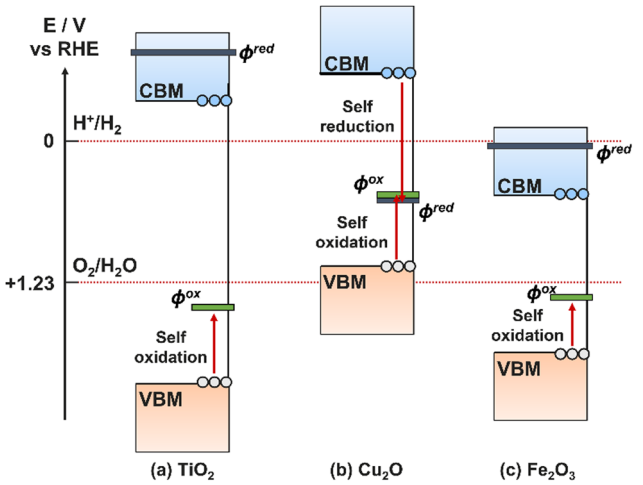

Fig. 15 Band energy levels for three common semiconductors compared to their reduction potentials (φ^{ox}, grey) and oxidation potentials (φ^{red}, green).

reactions of H_2/O_2 recombination and O_2 photoreduction due to their optimised selectivity and activity. However, the most promising options are noble metals and noble metal oxides (see Section 4.2), which are not suitable for large-scale application due to their high costs, rarity, and unsustainability.[191] Doping and heterojunction formation (Section 6.1) also improve charge separation efficiency, lowering the number of unconsumed charge carriers which can act towards self-oxidation or self-reduction.[16]

4.6 Material practicality

Even if a PEC electrode fulfils all electronic and structural requirements such that it performs perfectly, it must also be practical for application in large-scale, green, sustainable energy production and storage. The material must therefore be: (i) earth abundant; (ii) cheap to source and produce at large-scale; (iii) environmentally safe in production, operation, and disposal. Ideally, high percentage return recycling and/or regeneration of the material should be possible to minimise waste at end of life.[22,24,59] Consequently, considerations must be made towards both the deposition method and precursor design beyond simply maximised performance.

5. Precursor design and growth criteria for semiconductor materials

Molecular precursor design takes a systematic approach to thin film deposition, specifically engineering structures to modify the precursor thermal decomposition profile and mechanisms, increase stability and ease of handling, and open the door to a wider range of more complex precursors that can be used to deposit multinuclear, mixed phase, or uniquely structured semiconductors. This section will cover the range of options for tailoring precursor molecular structures towards both suitability for deposition, and properties of the resulting semiconducting films. Modifying the structure of a precursor to enhance a certain property will result in a change to all other properties, hence it is often necessary to work through many iterations of a precursors design, each new structure building on the benefits and limitations of the previous. A large range of case studies from previous reports of precursor design will be discussed, however, there is a distinct lack of literature on precursor design towards water splitting materials. Most discussions will therefore focus on the methods of precursor structural development and improvements towards properties for effective deposition, and resulting film properties that are required for water splitting; instead of specific examples that would report from precursor development to deposition to PEC characterisation.

All molecular design features discussed in Section 5 are summarised in Table 2, along with their influence on precursor and resulting material properties. This is not an exhaustive list, but acts as a guide towards tailoring molecular precursor design for specific deposition and thin film requirements and applications. It should be noted that when designing a precursor, it is essential to consider the simplicity and cost-effectiveness of the precursor synthesis method, whether it would be suitable for scale-up and real-world applications, and how environmentally sustainable its production and use would be.[192] A summary of molecular properties discussed in this section, and the measurement techniques used to study them, is also given in Table 3. It should also be noted that precursors should normally be isolated and purified at the end of synthesis to prevent contamination of the thin film, or disruption during growth, no matter what deposition technique or product is used.

In general, there are two categories of control for deposited semiconductor properties to consider: (i) the molecular precursor design; (ii) the deposition technique and conditions. When using ready-made, common precursors untailored for application such as metal nitrates, chlorides, or simple isopropoxides, ethoxides, and butoxides, not only will the precursor be unoptimized and untailored for the deposition technique and conditions, but the substantial element of semiconductor property control associated with the starting precursor will be lost, significantly limiting the potential of performance optimisation and enhancement.

5.1 Deposition requirements

The first aspect to consider when designing a precursor is the deposition technique that will be used, and the properties required for effective use in that method. Precursor deposition techniques can be split into two categories, solution-based and vapour-based. Solution-based depositions involve dissolving the precursor into a solvent solution, whereas vapour-based techniques rely on volatilisation of the precursor. It is therefore essential to consider the solubility and volatility properties of the precursor for the former and latter family of techniques, respectively.

5.1.1 Deposition techniques. In this review, there is a specific emphasis towards chemical vapour deposition (CVD) techniques, as these are suitable with a wide range of viable chemical precursors with flexibility in structure, allowing for tailoring and bespoke design. Indeed, CVD techniques are

Table 2 A guide for molecular precursor design features, how to achieve specific precursor properties, and the resulting thin film properties

Molecular design	Precursor property	Impact on material deposition
Multidentate ligand	Multi-step thermal decomposition Coordinative saturation for increased air/moisture stability	Nanostructured material Easier to handle, purer material, better solubility and volatility
Organic substituents sterically surrounding metal centre	Increased solubility Increased stability More complex decomposition	Faster deposition by AACVD increased solvent options Nanostructure changes Increased carbon contamination
Large organic chains on ligand	Increased solubility Greater carbon contamination Lower volatility More complex decomposition	Faster deposition by AACVD Nanostructure changes Increased carbon contamination
Fluorinated ligand	Increased volatility Increased solubility Increased thermal stability	Increased decomposition temperature Decreased carbon/by-product contamination Fluorine contamination
Multinuclear	Require larger/more ligands Decrease volatility	Doped and/or hybrid deposit from SSP
Dimer, trimer, oligomer, cluster (homo-polymetallic)	Increased thermal stability More complex decomposition Decreased volatility	Increased decomposition temperature Unique nanostructure and/or phase materials
Donor functionalised ligands	Increased air/moisture stability Reduced oligomerisation Increased solubility	Increased purity Access to difficult-to-make materials
Ligand adaptability to metal systems	Compatible metal precursors – similar solubility, volatility, thermal decomposition rates and mechanisms	High stoichiometric control in multi-source doped/hybrid materials Homogeneous films Single-step doped/hybrid material depositions
Anionic dopant species	Contain atoms that can act as dopants: Cl, F, N, C, S, Se	Single-source doped or chalcogenide materials
Isolated and purified precursor	High molecular purity	Increased purity Consistent depositions
Building block structures	Precursor shaped for growth of desired nanostructure	Controlled growth of specific nanostructure

Table 3 Molecular properties targeted in precursor design, and measurement techniques that can be used to study them

Molecular property	Measurement technique
Volatility	TGA – variation of wt% with temperature ramp Isothermal TGA – volatilisation rates and sublimation enthalpies
Thermal stability and decomposition kinetics and products	TGA – mechanism, decomposition rate, decomposition species and by-products (match wt% to fragment) Couple with NMR, GC-MS, MI-IR
Solubility	Qualitative – check transparency of solution with desired concentration of precursor in
Air/moisture stability	NMR before and after exposure
Solvent adduct formation	Single-crystal XRD
Molecular structure and composition	Single-crystal XRD
M–L bond strength	Single-crystal XRD

becoming increasingly commonplace in the fields of optics and electronics, possessing a great number of advantages for large scale commercial and industrial production, including: (i) uniform film production at high deposition rates; (ii) high control of deposit physical properties through operation conditions (temperature, duration, substrate); (iii) produces conformal

Table 4 Summary of some common CVD techniques, whether they require precursor volatility or solubility, and the main unique advantages and limitations associated with each technique

CVD technique	Volatility	Solubility	Advantages	Limitations
Low-pressure CVD	✓	✗	Simple reactor setup, good film uniformity	Higher process costs, not suitable for multi-source
Photo-assisted CVD	✓	✗	Lower process temperature, unique deposit structures	Higher process costs, not suitable for multi-source
Plasma-enhanced CVD	✓	✗	Lower process temperature, unique deposit structures	Higher process costs, not suitable for multi-source
Aerosol-assisted CVD	✗	✓	Precursor solubility required, multi-source suitability	Solvent decomposition contamination
Metal–organic CVD	✓	✗	Simple reactor setup, high throughput	Poor uniformity, low film purity compared to others
Atomic layer deposition	✓	✗	Highly controlled monolayer deposition	More restricted precursor requirements

films across complex shapes and surfaces; (iv) low processing costs. Due to this application in high throughput commercial depositions, as well as the intrinsic link to precursor chemistry, the focus of this review is on precursor design for CVD techniques, as no other deposition methods available fulfil both criteria so well.

Many variations of CVD exist for different reaction activation mechanisms and precursor types, summarised in Table 4. In the simplest case, CVD involves the volatilisation of a precursor which is subsequently thermally decomposed over a heated substrate to form the target material as a thin film. The structure and behaviour of the precursor itself is therefore the most influencing factor on the fabricated thin film properties. CVD also enables great flexibility in the design of suitable precursors, including the availability for simultaneous co-depositions of multiple precursors to create more complex materials. The reader is referred to ref. 193–196 for more detailed reviews on CVD techniques.

Among the techniques in the CVD family (Table 4), AACVD has a key advantage over other variations: the precursor only needs to be soluble in a solvent that can be aerosolised, without any chemical volatility requirements. AACVD is the only solution-based deposition technique in the CVD family, hence greatly increasing the range of potential precursor structures that can be used to deposit thin films, and opening the door to non-volatile, larger, and more complex precursor structures that can be used as SSPs for complex film deposition (Section 5.3), or for uniquely nanostructured films (Sections 5.4 and 5.6 respectively).[197,198] The number of operational conditions that can be varied to optimise film properties is also increased with AACVD, now including choice of solvent, precursor concentration, and carrier gas flow.

5.1.2 Volatility. Precursor volatility is an essential property for any vapour-phase deposition process, commonly CVD and ALD.[199] It is intrinsically linked to the strength of intermolecular forces, which are determined by a combination of molecular weight and geometry, and lattice structure for solids.[200] Some of the simplest ways to improve volatility are by controlling aggregation or oligomerization of the precursor by increasing the steric bulk of the ligand, and by using donor functionalisation to coordinatively and electronically saturate the metal centre to keep nuclearity at, or close to, one.[201]

Volatility of precursors is usually managed by the choice of organic groups. Ideally, the organic group of the ligand should have a large steric profile to reduce nuclearity, however, bulkier groups tend to indirectly reduce volatility by increasing the molecular weight, and increase thermal stability requiring higher process temperatures. In the development of $MgAl_2O_4$ precursors for CVD, a range of alkoxy groups have been tested and modified to achieve the best performing precursor. The molecular structure $[MgAl_2(O^iPr)_8]$ is a commonly used precursor, however, it was found to oligomerize during vapour transport due to the unsaturated metal centre within the framework, forming the less volatile structures $[MgAl_2(O^iPr)_8]_2$ and $[Mg_2Al_3(O^iPr)_{13}]$.[202] To prevent this, *tert*-butoxide (O^tBu) alkoxide groups were used instead of $\{O^iPr\}$ to make a $[MgAl_2(O^tBu)_8]$ structure, with the larger ligand hopefully increasing the steric profile and hindering oligomerization. However, the bulkier $\{O^tBu\}$ groups also reduce volatility and increase thermal stability to decomposition, now requiring higher process temperatures than with $\{O^iPr\}$ groups. Expanding on this, Kim *et al.* replaced only the terminal alkoxide groups present on the Al atoms with methyl groups to form $[MgAl_2(O^iPr)_4Me_4]$ and $[MgAl_2(O^tBu)_4Me_4]$, which show greater volatility than both the $[MgAl_2(OR)_8]$ compounds.[203] The lower molecular weight gave better vapour-phase transport properties, however, at 600 °C, the temperature required for crystalline deposits using $[MgAl_2(O^iPr)_8]$, the resulting deposit for both methyl substituted precursors was amorphous, requiring annealing in air at 900 °C for crystallinity.

Veith *et al.* used hydride groups instead of methyl to produce the low weight precursor $[MgAl_2(O^tBu)_4H_4]$, with higher volatility ($[MgAl_2(O^tBu)_8]$ vaporisation temperature = 100 °C; $[MgAl_2Me_4(O^tBu)_4]$ 60 °C; $[MgAl_2H_4(O^tBu)_4]$ 45 °C) and forming crystalline films at 450 °C, but now contained small percentages of residual organics.[204] The choice of methyl and hydride groups in these examples was also for tailoring of decomposition products, predicting β-hydrogen elimination to form gaseous, non-contaminating methane or dihydrogen products upon decomposition (Fig. 16), as previously shown in similar ZnO and MgO precursors.[205] Precursors with increasing volatility were also reported to possess increased film growth rates and surface roughness. This combination of work on $MgAl_2O_4$ precursors is

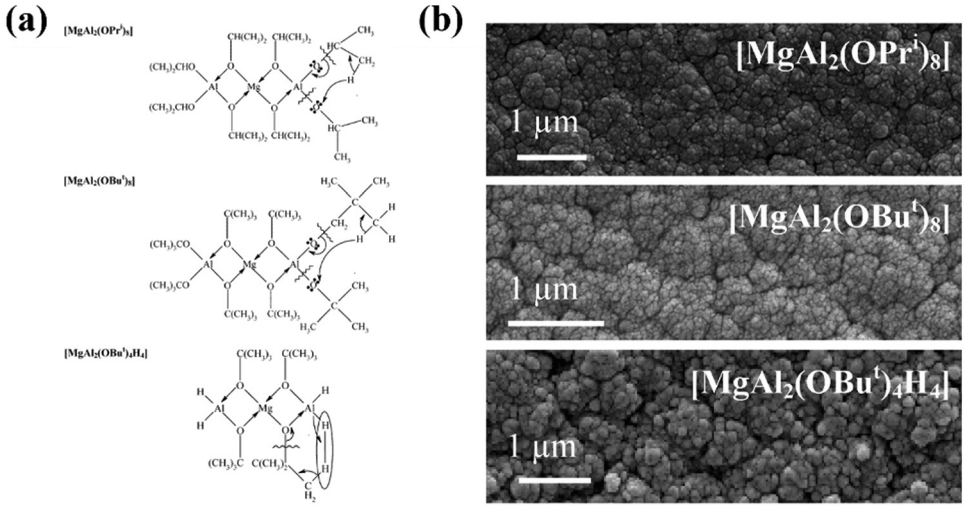

Fig. 16 (a) Proposed decomposition methods and (b) scanning electron microscopy surface images for precursors (top to bottom) $[MgAl_2(O^iPr)_8]$, $[MgAl_2(O^iPr)_8]$, $[MgAl_2(O^iPr)_8]$. Reproduced with permission from ref. 204 copyright 2004, American Chemical Society.

a fitting example of the importance of precursor chemistry towards the fabrication process and the properties of the final material, and how minor changes to a structure can have significant influence. The focus of this small study was solely on volatility and decomposition, hence there is far more work that could be done on designing the precursor molecular structures to encompass other properties, especially targeting a film application.[206]

Fluorination of alkoxide ligands is an alternative strategy reported to increase molecular volatility due to the subsequent strong repulsion between complexes from the introduction of non-bonding p electrons on fluorine, reducing intermolecular interactions.[207–210] Fluoroalkoxides are also hydrophobic, providing additional stability against hydrolysis from atmospheric moisture.[207] While fluorinated ligands are sometimes reported in SSPs for fluorine-doped materials,[211] most commonly fluorine-doped tin oxide (FTO),[212,213] it is feasible to fabricate thin films without fluorine incorporation despite using fluorinated precursors. The strong C–F bond means complexes will thermally decompose into more stable fluorine-containing fragments, removing the fluorine atoms as process-inert by-products and preventing incorporation into the film.[214] Of course, the greater the temperature of the deposition process, and more reactive the precursors and thermal by-products, the greater the likelihood of fluorine contamination. For a more in-depth discussion of fluorinated ligands used in inorganic material precursors, the reader is directed towards the review by Mishra and Daniele.[215]

5.1.3 Solubility. For solution-based deposition methods, it is important to have control over the solubility of the precursor. Not only is high solubility needed, but understanding the range of solvents that can be used is essential for optimising a process, different solvents each impacting the deposit growth differently.[216,217] The ability to tune a molecular precursor towards desired solvents can therefore be invaluable in semiconductor development. In the simplest case, low-nuclear (monomeric and dimeric) complexes, and smaller ligand moieties, favour good solubility.

The solubility of the precursor can be indirectly improved using perfluorinated alkyl chains and CF_3 groups, which are less π-donating than the conventional organic equivalents, therefore favouring low-nuclear (monomeric and dimeric) structures and suppressing aggregation, leading to greater solubility.[215] Additionally, the strong secondary M–F bonds that are formed with oxophilic metals increases the metal coordination number to prevent the formation of multinuclear complexes and maintain high solubility. These secondary bonds also increase the thermal stability of the complex,[209] which would normally be considered a negative result of fluorination, however, it does provide a means to control and tune decomposition temperature without significantly changing the overall molecular structure that has been designed. This is particularly useful when designing a precursor to be compatible with an already existing process, or for co-depositions of two or more different precursors, all requiring similar decomposition temperatures and kinetics to ensure a homogeneous film deposition across the substrate.

Organic solvents are often required due to the air and water instability of many molecular precursors; hence precursors should be designed with organic chains or groups to increase solubility in these solvents. There is a balance between larger organic moieties which maximise solubility, and smaller groups which facilitate lower energy and cleaner thermal decomposition.[218] The polarity of the molecule will also determine which solvents the precursor is soluble in ref. 216 and 219. Solvents containing potential contaminants such as fluorine and chlorine should be avoided.

Carbon contamination in processes near or above the thermal decomposition temperature of the solvent is inevitable. Interestingly, the carbon particles from this decomposition can act as nucleation sites during film growth, influencing film properties including crystal orientation, nanostructure, grain size, and phase.[220,221] The carbon contaminants can be easily removed by annealing post-deposition, but the impact on the film morphology and growth will remain. The selection of

solvent must therefore include considerations towards thermal decomposition temperatures compared to the process temperature being used, and if the result of carbon contamination on the final film nanostructure and grain size is beneficial or detrimental.

Many complexes will form adducts with the solvent molecules they are dissolved in, altering the structural and thermal properties. For particularly reactive precursors, this can bring the advantage of increased air/moisture stability due to steric saturation of the metal centre.[222] Some solvent adducts will impact the thermal properties more significantly than others, partially dependent on how easy the solvent is to remove upon heating, and hence how much the decomposition/volatilisation of the precursor is altered. Buchanan *et al.* compared diglyme, tetrahydrofuran (THF), and dimethoxyethane (DME) solvent adducts to solvent-free species for metal–organic chemical vapour deposition (MOCVD) precursors (targeting volatility) and found that the introduction of solvent adducts, particularly DME, not only increased the stability of the precursors due to steric saturation of the metal centre, but also the volatility.[214] The bidentate nature and low boiling point of DME contributed to it performing best in both aspects, increasing steric saturation while still being easily removed upon heating.

In AACVD, the volatility and viscosity of the solvent also has significant impact on the deposition. Degradation of more volatile solvents usually occurs sooner and faster upon entering the heated furnace, leading to the formation of more particulates compared to less volatile solvents. These act as nucleation sites, inhibiting crystallite growth when in excess and therefore yielding smaller crystallite sizes.[221] Eslava *et al.* demonstrated this with a titanium oxo/alkoxy cluster TiO_2 precursor, deposited using either toluene or THF solvents, identified as the only suitable solvents with good precursor solubility.[139] As expected, THF, the far more volatile solvent, resulted in smaller grain sizes and smaller overall plate-like sheets in the nanostructure, yielding photoanodes with lower PEC performance, suggested to be a result of a decrease in the exposure of the most active TiO_2 (010) facets. Interestingly, the lower viscosity of THF compared to toluene (0.55 *vs.* 0.59 cP at 298 K)[223] should lead to superior grain growth due to the more consistent aerosol generation and increased spray volume rate providing an uninterrupted, stable supply of precursor.[224,225] Larger, well-connected grains promote greater electronic conductivity by reducing grain boundary areas, and the number of grain interfaces charge carriers must travel across.[226,227] As shown by Eslava *et al.*, this does come with the side-effect of significantly higher precursor usage rates for lower viscosity solvents (0.3 and 0.7 ml min^{-1} for toluene and THF respectively), which could be useful if the increased usage correlates to increased film growth rate/thickness, however, in this instance the films had similar thicknesses after the same duration, and thus the increased usage corresponds to wasted precursor and solvent.

The choice of solvent can determine both the structure and phase of the deposited films. Parkin *et al.* reported the AACVD of TiO_2 onto steel substrates using methanol, ethanol, hexane, dichloromethane (DCM), and isopropanol solvents.[217] Methanol yielded exclusively rutile phase films, while all other solvents exclusively anatase. Interestingly, when mixing methanol and ethanol solvents, the phase became majority rutile at just 10% methanol, and was exclusively rutile at $\geq$50% methanol, implying methanol solvent had a stronger impact on the deposition mechanism. The morphology of the films also varied with varying mixtures of ethanol and methanol, ranging from plate-like crystallites in 100% ethanol, needles in 100% methanol, and block-like crystallites in mixtures (Fig. 17). Methanol solvent has been previously reported to act as a reducing or oxidizing agent due to its thermal breakdown mechanism forming carbon dioxide and hydrogen, an explanation for this variation from ethanol deposits despite the similar solvent properties.[228] Carmalt *et al.* used hexane or DCM in an *in situ* AACVD reaction for NbS_2 and TaS_2 films, which showed significantly different sized cluster morphologies depending on the solvent, however, the larger, and less uniform, clusters were grown using hexane for TaS_2 but DCM for NbS_2.[229]

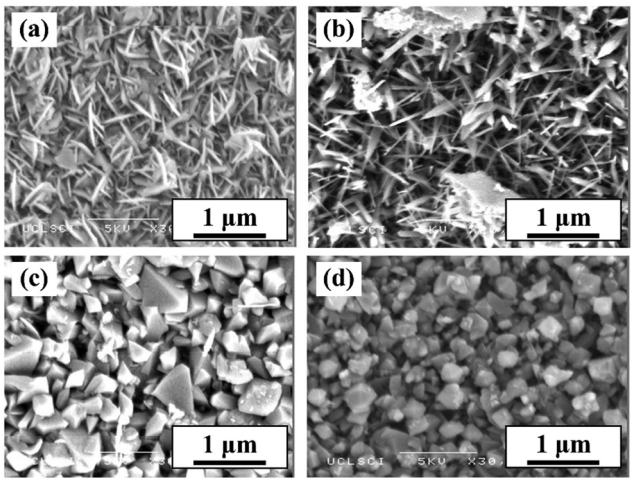

Fig. 17 Scanning electron micrographs of TiO_2 grown on steel substrate by AACVD use carrier solvent of (a) ethanol, (b) methanol, (c) 10% methanol and 90% ethanol, (d) 25% methanol and 75% ethanol. Reproduced with permission from ref. 217 copyright 2012, Wiley-VCH.

The use of solvents for precursor synthesis *in situ* can produce films with higher purity and reduced oxygen deficiency,[230,231] while also eliminating the need for precursor purification and isolation, increasing the efficiency of both production time and cost. Additionally, it provides an alternative means of deposition for precursors that are difficult to isolate, and different morphologies can be constructed dependent on the solvent reactant used.[232] Carmalt *et al.* studied *in situ* precursor synthesis in CVD applications in detail, first fabricating In_2O_3 films from the AACVD reaction of Me_3In and ROH,[233] then reporting the first use of AACVD for Ga_2O_3 fabrication using $[Ga(NMe_2)_3]_2$ and ROH,[231] and comparing the use of 2 pre-made diorganoalkoxygallanes in low pressure CVD (LPCVD) with *in situ* equivalents made from Et_3Ga and excess ROH in AACVD (Fig. 18).[230] LPCVD resulted in oxygen deficient Ga_2O_3 thin films, whereas the *in situ* synthesis of precursor in AACVD gave stoichiometric Ga_2O_3. This was suggested to be a result of low oxygen content in the precursor

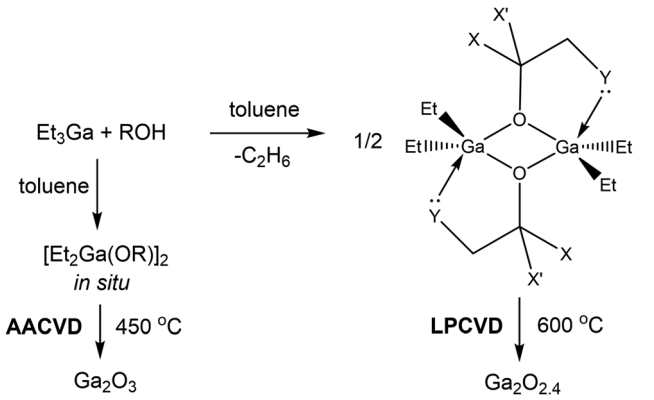

Fig. 18 *In situ* precursor formation, using AACVD and lower process temperature, *versus* pre-deposition synthesis, isolation, and purification; R = $CH_2CH_2NMe_2$, $CH(CH_3)CH_2NMe_2$, $C(CH_3)_2CH_2OMe$, or $CH(CH_2NMe_2)_2$, X and/or X′ = H, CH_3, or CH_2NMe_2; Y = NMe_2 or OMe.[230]

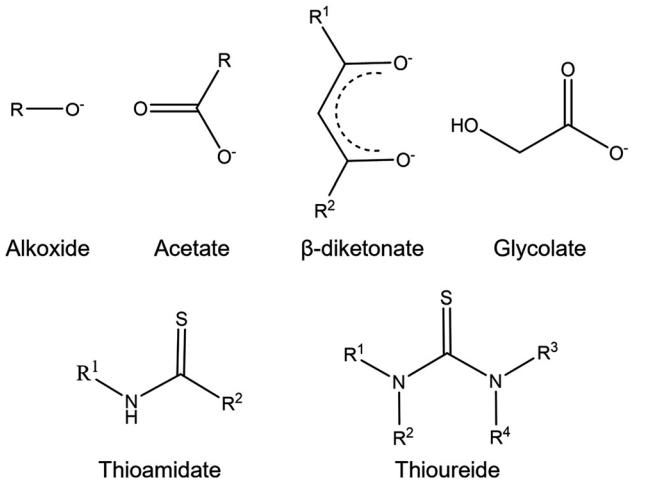

Fig. 19 Common ligands used for metal oxide and metal sulfide precursors.

molecule, but excess alcohol in the *in situ* reaction increased oxygen availability in the deposition chamber and prevented deficiency. The precursor synthesis reaction must be studied and optimised before use in deposition to ensure a full understanding of the chemicals present in the reaction chamber. More reactive input species are preferred to guarantee a complete reaction before entering the chamber.

5.2 Ligand structure

While solubility and volatility only need to be considered for solution or vapour-based deposition techniques respectively, all precursor properties discussed herein can be applied for all deposition methods and target photoelectrode materials. Section 5.2 will cover the fundamental aspects of ligand design for any new precursor ranging from small, simple structures to large, complex structures.

5.2.1 Metal oxides and chalcogenides. The structural design of the ligand in a metal complex is one of the key parameters for effective control of molecular properties.[234] For metal oxide precursors, it is common to use alkoxide ligands for many reasons. Alkoxide groups provide terminal oxo ligands as an oxygen source during film deposition, and can therefore be used to deposit metal oxides without oxygen deficiency and in non-oxygen or vacuum environments.[235] They also contain highly reactive, electronegative OR groups that can speed up the required *in situ* chemical reactions during deposition, and facilitate lower process temperatures.[200] Residual alkoxy groups decompose rapidly and at significantly lower temperatures compared to alternative metallo-organic precursors such as acetates, glycolates, and β-diketonates (Fig. 19), reducing the amount of organic contamination in the deposited films and again requiring lower temperatures.[236,237] Solution-based deposition techniques particularly favour alkoxide ligands due to their high solubility in a variety of solvents, low decomposition temperatures, and broad range of ligand structures available.[238] The flexibility of design in alkoxide ligand structures is vital towards their use in bespoke molecular precursors. The size and symmetry of the organic moiety contributes towards the solubility and solvent range, while the steric bulk of the ligand around the metal centre will determine if the complex is monomeric, dimeric, or oligomeric, or can form a cluster or cage. Chelating alkoxide ligands can also be used to ensure monomer formation if the deposition process requires it.[210,239]

The high reactivity of alkoxides makes them sensitive to moisture exposure, forming clusters or metal oxide particles due to partial hydrolysis which cannot deposit in the same way as the precursors, or at all. This decreases the ease of handling and use, requiring inert conditions during synthesis and deposition.[219] Fortunately, the molecular design can be altered to increase stability without losing the beneficial alkoxide properties. Larger, multinuclear complexes with oxo-bridges and alkoxide ligands (metal oxoalkoxides) can be synthesised by the non-hydrolytic condensation of alkoxides, usually showing higher solubility, lower volatility, and greater thermal and chemical stability.[200] Alternatively, multidentate alkoxide ligands can be used to reduce the number of terminal, hydrolysable alkoxide groups and provide greater steric protection around the metal centre, increasing the chemical stability without significantly increasing the molecular size or number of metal atoms.[207,240]

While most precursor design case studies in this review focus on metal oxide precursors, it is important to note that the same understanding can be applied to the growing field of metal chalcogenide precursors. It is most common to use dual-source precursors to deposit a metal chalcogenide, usually a precisely designed metal alkyl coupled with H_2S, however, it is becoming more apparent the advantages of SSPs for the development of these materials. Thiolate ligands ($[R–S]^-$) such as thioamidates[241] and thioureides[242,243] (Fig. 19) are good choices for sulfur-based chalcogenide precursors due to the flexibility in the organic group structure for tailoring steric size, shape, polarity, composition, and molecular weight.[244] Metal chalcogenide SSPs are discussed in detail in Section 5.3.6.

5.2.2 By-products and impurities. By-products formed during thermal decomposition are largely determined by the ligand

structure used, and should be studied and optimised to ensure minimal contamination into the target material; for example, using techniques such as gas chromatography coupled with mass spectroscopy (GC-MS) and NMR spectroscopy on cold-trapped products.[218] For solution-based techniques, by-products should be unreactive to the process conditions, while for vapour-based techniques they should be volatile gases such that they are completely removed from the system using carrier gas or vacuum. Controlling the by-products produced is difficult, however, certain products can be made more likely by using ligand groups containing much of the desired product's organic structure. For example, isobutylene and *tert*-butanol are common decomposition products of complexes containing *tert*-butyl groups.[245,246] Organic by-products can be made more volatile using fluorinated ligands (Section 5.1.2) such that fluorinated organic fragments will be formed form decomposition. Mazhar *et al.* has synthesised a range of multinuclear precursors that use a trifluoroacetato group instead of common, less volatile butoxy or acetate groups. This is particularly useful for heterometallic semiconductors like $MgTi_2O_5$ which have strong property dependence on purity and metallic ratios.[247]

Film impurities are ubiquitous across all deposition techniques for all target materials. Carbon impurities are the most common, arising from M–C bonds that are not broken and replaced, or from thermal decomposition of carbon containing by-products. This contamination can be minimised through precursor design, using ligands that form M–O bonds (*e.g.* alkoxides) for metal oxide depositions, or M–N (*e.g.* amides) for metal nitrides. Alternatives such as M–Cl species have been reported, however, this usually then leads to chlorine contamination instead.[248] In metal oxide-free materials, oxygen impurities are also a significant issue, even present if the precursor does not contain oxygen atoms due to background oxygen levels and the higher M–O thermodynamic driving forces compared to M–N or M–Cl. The simplest way to minimise this is by purging the system with extreme vacuum to make background oxygen negligible, however, this is expensive, energy intensive, and not a complete fix. Instead, the precursor can be designed to contain reducing surface conditions to prevent oxygen incorporation. Buttera *et al.* used a tris(dimethylamido)aluminium(III) ($[Al(NMe_2)_3]_2$) precursor to eliminate carbon impurities in the PE-ALD deposition of AlN,[249] yielding carbon contamination of approx. 1%; compared to trimethyl aluminium, the standard Al-based ALD precursor, which usually yields 3–6% carbon,[250,251] and aluminium chloride ($AlCl_3$) which gets similar 1% carbon impurity, but with 1–3% chlorine contamination as well.[248] Despite the ultra-high vacuum used in ALD, significant oxygen contamination was present in XPS spectra, hence the precursor design was later amended to replace two dimethylamine groups with strongly reducing hydride groups ($[AlH_2(NMe_2)]_3$) that can protect the metal centre from oxygen incorporation, lowering the final oxygen impurity to $<2\%$.[252]

5.2.3 Donor functionalisation. Ligands can be functionalised to contain Lewis base donor groups that can increase the coordination number of the central metal atom to enhance air/moisture stability, limit dimerization/oligomerization, and prevent solvent adduct formation.[207] As exemplified for a series of diorganoalkoxogallanes by Carmalt *et al.*, the use of a donor functionalized ligand eliminates the need for a separate organic ligand and donor group to stabilize the electron deficient gallium alkoxide complex, where water sensitivity is a common shortfall for these species in solution-based processes.[230] The reduction in nuclearity of complexes by donor functionalisation has been reported to be more impactful with functionalised ligands containing α-branching, compared to unbranched or β-branched ligands (Fig. 20), due to the increased cone angle and chelating behaviour increasing the steric bulk.[200,253,254] Decreasing nuclearity while ensuring complete surrounding of the metal centre by organic moieties will also improve solubility. Multidentate Lewis bases (donor functionalised multidentate ligands) are particularly recommended to ensure complete coordination and electronic saturation towards the metal centre from a single ligand, without requiring additional groups to form monomeric or low-nuclearity complexes.[201]

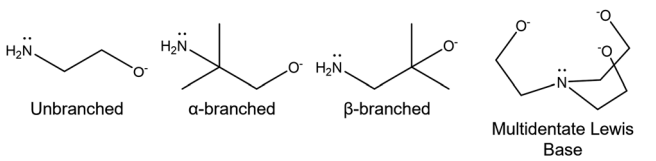

Fig. 20 Donor functionalised ligands with no branching, α-branching, β-branching, and multidenticity.

5.2.4 Adaptability. Adaptability of a ligand to many metal centres is important for multi-component depositions, either for depositing hybrid materials like $BiVO_4$ and Fe_2TiO_5 using dual-source precursors, or for the fabrication of a cation-doped material. Stoichiometric control is only possible if the precursors have similar solubilities/volatilities (depending on the deposition technique used), and thermally decompose at similar temperatures and rates. In CVD of $BiVO_4$, for example, separate Bi and V precursors are commonly used, however, if the Bi precursor decomposes faster or at lower temperature, the deposit will not be homogenous, and instead contain higher Bi concentration on the 'front end' (nearest the precursor input) and higher V on the 'rear end'.[220] The easiest way to ensure these precursors properties remain compatible is using the same, or similar, ligands on both, rather than finding a completely new ligand structure that will provide the same properties. Another alternative method for ensuring homogeneous deposition is through SSPs, where all metal centres required for doping or hybrid material formation reside within a single precursor, bypassing the need for multiple compatible precursors.

5.3 Single-source precursors

5.3.1 Single *vs.* dual-source precursors. Metal hybrids and doped metals are mostly deposited using multiple different precursors simultaneously, each containing one of the elements required for the final film. This allows for great flexibility and variety in the precursor design with few limitations other than those imposed by the deposition technique.[193] Using different precursors simultaneously does, however, lead to complications

associated with differing thermal decomposition rates and temperatures, solubilities and volatilities, and different film deposition mechanisms leading to varied growth rates; all of which will contribute towards non-homogeneous and non-stoichiometric deposition.[218,255,256] While stoichiometries can be improved by trial-and-error depositions to find the right precursor ratio, non-homogeneous deposition can only be fixed by using more compatible precursors with similar pertinent properties.

Alternatively, mixed-metal multinuclear precursors can be used to deposit complex hybrid, doped, and mixed materials as a single molecular source (Fig. 21),[257] allowing deposition conditions to be tailored specifically for that single precursor, as well as introducing benefits such as higher purity of the deposited material and defining stoichiometries at a molecular level.[245,258] There is, however, higher complexity in molecular composition and design, and metals within the precursor molecule must be accessible for deposition upon thermal decomposition and with the correct stoichiometries for the desired film, particularly challenging for doping where as little as a 1–5% dopant concentration is standard. SSPs will inevitably have larger and heavier structures than smaller, simpler precursors used in dual-source deposition, hence volatility will always be poor even with tailored structure modification, therefore ruling out the use of vapour-based deposition techniques. The importance of AACVD (Section 5.1), the only solution-based CVD technique, is now clear. Solubility is a far easier property to engineer in large, complex SSP structures, hence the flexibility in structure and design for SSPs is not limited by what can retain some level of volatility, and deposition can still occur *via* a highly promising CVD method.

There are two approaches towards SSP design for a multinuclear system: (i) binding many small, simple ligands individually to multinuclear centres; (ii) specifically designing a single, large ligand system that acts as a complex scaffold for multiple metal centres. Both can be effective, but the latter approach provides greater freedom in structural design and tailoring. Scaffolds can also be multi-use, with a range of metal atoms capable of integrating into the centre, hence a variety of doped or hybrid mixed metal semiconductors can be fabricated using a single ligand design, and without significantly altering the properties of the precursor which would require re-optimisation of the deposition conditions – a slow and expensive process.[259,260]

SSPs can be designed for three possible scenarios: (i) SSP-I, the stoichiometric ratio of elements in the SSP is equal to that in the deposit, but the number and structure of side products is not controlled (eqn (9)); (ii) SSP-II, same as SSP-I but with ligands that have been designed to decompose into fewer, inert and/or volatile side products (eqn (10)); (iii) SSP-III, the precursor decomposes to form two or more solid phases that make up the resulting composite deposit (eqn (11)).[262]

$$AB_nXY \rightarrow AB_n + X + Y \quad (9)$$

$$AB_nXY \rightarrow AB_n + X\text{–}Y \quad (10)$$

$$AB_nXY \rightarrow AB_{n\ -\ m} + mB + X\text{–}Y \quad (11)$$

All reports of single-source mixed/doped metal oxide precursors specifically for PEC water splitting are listed in Table 5. It is evident that this is an underexplored area with a high research potential and impact factor. For additional comprehensive reviews on the synthesis of SSPs, the reader is directed towards ref. 261 and 263.

5.3.2 SSPs for mixed-metal hybrid systems. SSPs have been reported for a variety of metal oxide thin films, often using alkoxide-based ligands to ensure low decomposition temperature and high compositional purity.[205,270–275] $BaTiO_3$, $BaZrO_3$, and $BaTi_{0.5}Zr_{0.5}O_3$ were developed by Veith *et al. via* a sol–gel technique using $[BaM(OH)(O^iPr)_5(HO^iPr)_3]_2$ (M = Ti, Zr) and $[BaTi_{0.5}Zr_{0.5}(O^iPr)_6]_2$ SSPs.[245] $BaTiO_3$ thin films were reported to be pure state at 600 °C using these precursors, whereas the equivalent films using dual-source precursors still contained many impurities at 1200 °C including $BaCO_3$ and Ba_2TiO_4. The crystallite size distribution for the SSPs was also significantly reduced.

As noted in Section 3.1.2, pseudo-brookite structured Fe_2TiO_5 is a promising material for PEC water splitting, where

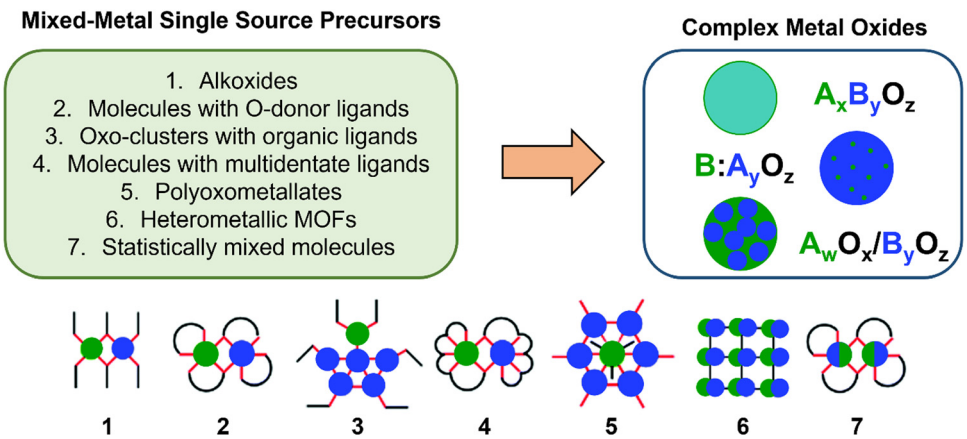

Fig. 21 Structures for mixed-metal SSPs and the deposited complex metal oxides. Reproduced with permission from ref. 261 copyright 2020, Royal Society of Chemistry.

Table 5 Reported novel structures synthesised for use as mixed/doped metal oxide SSPs for PEC water splitting application

Precursor[a]	Material	Deposition technique	Nanostructure	Substrate/temp/solvent	j^b/mA cm^{-2}	Ref.
$[Ti_2(OEt)_9(NiCl)]_2$	NiO_x/TiO_2	Spin coating	Smooth unfeatured	WO_3/—/toluene	0.45	98
$[Ti_4Mo_2O_8(OEt)_{10}]_2$	Mo–TiO_2	Spray pyrolysis	Aggregated islands	FTO/150 (anneal 700)/ toluene	0.2	264
$[Bi_2(DMSO)_6V_{12}O_{33}Cl]_2[Zn(DMSO)_6]$	Zn–$BiVO_4$	Drop casting	Mixed rods/particles	FTO/550/DMSO	1.07	259
$[Mg_2Ti_4(O)_2(OH)_4(TFA)_8(THF)_6]\cdot THF$ TFA = trifluoroacetato and THF = tetrahydrofuran	$MgTi_2O_5$	AACVD	Compact spheroid objects	FTO/600/EtOH	0.25	247
$[Mn_2Ti_4(TFA)_8(THF)_6(OH)_4(O)_2]\cdot 0.4THF$ TFA = trifluoroacetato	Mn_2O_3–$4TiO_2$	AACVD	Uniform cube/rod distribution	FTO/450/THF	0.343	265
$\{[CaMn(OAc)(TFA)_3(THF)(H_2O)_2]\cdot 3THF\}_n$ (OAc = acetate, TFA = trifluoroacetate, THF = tetrahydrofuran)	$Ca_2Mn_3O_8$–CaO	AACVD	Spheres	FTO/500/THF	1.3	266
$[SrNb_2(O^iPr)_{12}(HO^iPr)]$	$SrNb_2O_6$	Electro-spinning	Nanofibers	—/1000 calcination/ isopropanol	0.16	267
$Zn_6(OAc)_8(\mu\text{-}O)_2(dmae)_4$	ZnO	AACVD	Dense rectangular	FTO/400/THF	0.09	268
$\{Zn_5(TFA)_7(OH)_2(H_2O)_4(OAc)\}_n\cdot 2(C_4H_6O_2)$ [TFA = trifluoroacetate, OAc = acetate] $Ag(CH_3COO)$	ZnO, Ag–ZnO	AACVD	ZnO: dense pyramidal particles Ag–ZnO: porous rounded particle	FTO/500/THF	ZnO: 0 at 0.8 V Ag–ZnO: 0.55 at 0.8 V	269

[a] Only the highest performing photoelectrode and precursor is listed from each literature report. [b] Photocurrent density measured at 0 V *vs.* RHE under 1 sun (100 mW cm^{-2}, AM 1.5G) solar simulation, unless stated otherwise. All potentials are *vs.* RHE.

purity can have a significant impact on the performance of the film, and therefore it makes sense to deposit using a SSP.[276–279] Single-source deposited Fe_2TiO_5 appears difficult to produce as a phase pure material however, due to its high temperature of formation but low thermodynamic stability relative to its secondary phases, hematite and rutile.[280,281] Soares *et al.* developed the $[FeCl\{Ti_2(OPr^i)_9\}]$ precursor (Fig. 22) used in sol–gel deposition, which obtained films containing: (i) anatase TiO_2 and amorphous Fe_2O_3 at 500 °C; (ii) rutile TiO_2, α-Fe_2O_3, and pseudobrookite Fe_2TiO_5 at 700 °C; (iii) rutile TiO_2 and pseudobrookite Fe_2TiO_5 at 1000 °C.[282] Klabunde *et al.* reported similar issues with a range of metal titanates; using a $[M\{O\text{–}Ti(OPr^n)_3\}_2]$ (M = Mg, Mn, Fe, Co, Zn, Sn) precursor (Fig. 22b), composites of $MTiO_3/TiO_2$ were formed, except for M = Mg where pure pseudobrookite $MgTi_2O_5$ was obtained.[283]

Obtaining mixed phases from SSPs is often more common than single pure phases, previously defined as SSP-III. The precursor $[NdAl_3(O^iPr)_{12}(Pr^iOH)]$ formed equimolar crystalline $NdAlO_3$ and amorphous Al_2O_3 when applied in sol–gel and CVD techniques by Mathur *et al.*[284,285] Mixed phase metal/metal oxides are also possible, for example, in work by Veith and Kneip, a $BaSn_2(O^tBu)_8$ precursor used in MOCVD formed Sn and $BaSnO_3$ mixed phases due to the disproportionation of the two valent Sn species to Sn(0) and Sn(IV).[286] While single-source mixed-metal precursors have a greater occurrence of forming mixed phases due to the presence of multiple metal centres simultaneously depositing, it is important to note that it is not a unique characteristic and it is possible to fabricate similar mixed metal/metal oxide films from homo-nuclear precursors such as $[Ge(O^tBu)_2]_2$, $[Sn(O^tBu)_2]_2$, $[Pb(O^tBu)_2]_3$ forming (α-Ge/GeO_2), (β-Sn/SnO_2), and (Pb/PbO_2) respectively,[287] and mixed phase metal oxide films such as rutile/anatase–TiO_2 from $[(EtO)Ti\{OCMe_2CH_2\}_3N]$.[288]

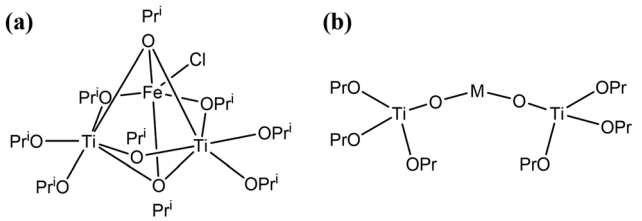

Fig. 22 Molecular structures of (a) $[FeCl\{Ti_2(OPr^i)_9\}]$, (b) $[M\{O\text{–}Ti(OPr^n)_3\}_2]$ (M = Mg, Mn, Fe, Co, Zn, Sn).

5.3.3 SSPs for co-depositions. Mixed-metal precursors can also be used as SSPs for more creative applications other than simply hybrid material depositions. For example, Reisner *et al.* designed a $[Ti_2(OEt)_9(NiCl)]_2$ precursor as a simultaneous deposition source for NiO_x and TiO_2, fabricating both an electrocatalyst and stabilisation/protective layer respectively in a single deposition step, while also functioning as a p–n heterojunction for enhanced charge transport.[98]

5.3.4 SSPs for doping. Doped films can be fabricated from SSPs, however, there is less control over the relative amount of doping compared to dual/multi-source – instead of directly varying the precursor ratio, it relies on the precursor atomic ratio and relative incorporation rates of each element present.[273,289,290] Eslava *et al.* fabricated a Mo-doped TiO_2 film by spray pyrolysis using a $[Ti_4Mo_2O_8(OEt)_{10}]_2$ heterometallic oxo cage (Fig. 23), obtaining a mixed anatase–rutile phase.[264] Due to there being fewer process variables to optimise in SSPs compared to dual-source, the remaining conditions, particularly annealing parameters, become even more significant for the overall film properties and performance, as seen in this work. Interestingly, the Mo atoms in these films were found to sublime at annealing temperatures greater than 600 °C, leaving behind only substitutional and interstitial Mo, creating pores from now vacant Mo sites to create a high surface area, porous structure.

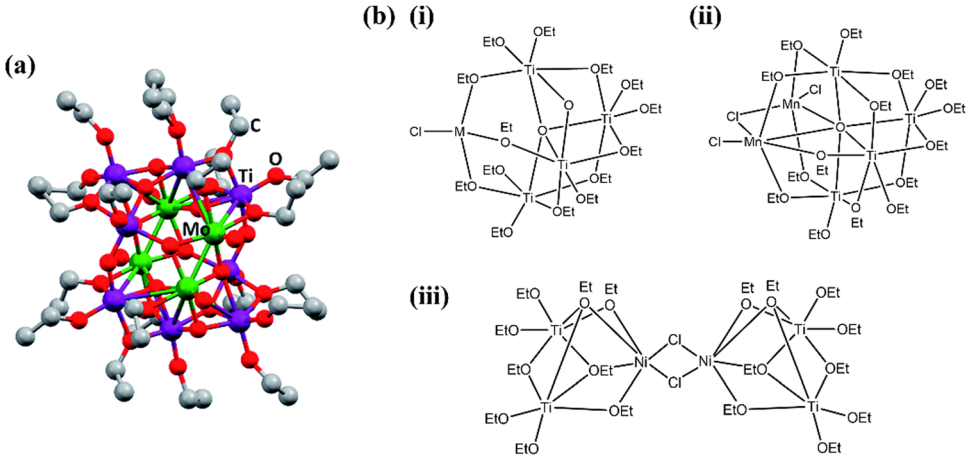

Fig. 23 Molecular structures of (a) $[Ti_4Mo_2O_8(OEt)_{10}]_2$, reproduced with permission from ref. 264 copyright 2018, Royal Society of Chemistry, (b) (i) $[Ti_4O(OEt)_{15}(MCl)]$ (M = Co, Zn, Fe, Cu), (ii) $[Ti_4O(OEt)_{15}(Mn_2Cl_3)]$, (iii) $[Ti_2(OEt)_9(NiCl)]_2$.

Similar work developed a family of heterometallic titanium oxo cage SSPs for different metal-doped TiO_2 films using a simple solvothermal reaction of $Ti(OEt)_4$ with a transition metal dichloride ($M^{II}Cl_2$).[260] The nature of the cage was dependent on the metal ion in each case due to differing ionic radii and strength of interactions, resulting in $[Ti_4O(OEt)_{15}(MCl)]$ (M = Co, Zn, Fe, Cu), $[Ti_4O(OEt)_{15}(Mn_2Cl_3)]$, and $[Ti_2(OEt)_9(NiCl)]_2$ stoichiometries (Fig. 23), hence the doping stoichiometry for each will also be different within similar deposition parameters. Deposition studied using these precursors were not carried out.

Polyoxometallate (POM) cages of the form $[M_xO_y(OR)_z]$ are a promising solution-based precursor for thin film deposition due to the readily hydrolysable alkoxide groups, high solubility in organic solvents, and vast flexibility in molecular design.[291] Modifications can be made to the structure to include functional ligands that will vary the thermal decomposition mechanism, and thus phase and morphology of the deposit,[292,293] yield highly nanoporous or mesoporous films,[294] or contain atoms for anionic doping (halides for example). Such structures are known as functional ligand-modified POMs (L-POM) with the formula $[M_xO_y(OR)_z(L)_m]$ (OR = alkoxide, L = functional ligand). The yielded thin films are usually amorphous due to substantial amounts of organic residue because of poor decomposition from the L group, hence films require further calcination to remove carbon contamination and obtain crystalline films.[295]

Additional metal cations can be added into the structure of polyoxotitanates (POT) to form a metal-doped POT (M-POT, $[Ti_xO_y(OR)_zM_nX_m]$, M = metal ion, X = anion such as halide), which can act as a SSP to metal-doped materials. Importantly, M-POTs give a high degree of atomic control over the level of doping, for example, Wright *et al.* synthesised three Ce-POTs with structures $[Ti_{28}O_{38}(OEt)_{38}(EtOH)_{1.4}CeCl]$, $[Ti_8O_7(HOEt)(OEt)_{21}Ce]$, and $[\{Ti_2O(OEt)_8\}(EtOH{\cdot}CeCl)]_2$ (Fig. 24) for use as Ce-doped TiO_2 SSPs.[296] $[Ti_{28}O_{38}(OEt)_{38}(EtOH)_{1.4}CeCl]$ and $[Ti_8O_7(HOEt)(OEt)_{21}Ce]$ both contained high Ti : Ce ratios, 28 : 1 and 8 : 1 respectively, and yielded anatase TiO_2 films with Ce doping at the exact concentrations matching the precursor stoichiometries. Interestingly, $[\{Ti_2O(OEt)_8\}(EtOH{\cdot}CeCl)]_2$, with a low Ti : Ce ratio (2 : 1), instead formed a phase separated TiO_2-coated $Ce_2Ti_2O_7$ film, implying that the inclusion of Ce(III) into the TiO_2 lattice is concentration dependent. This behaviour has been reported for POTs multiple times, for example, in similar systems forming Ba-TiO_2 and $BaTiO_2$ from Ba-POT cages.[297,298] The flexibility in choice of metal dopant makes these M-POT systems very

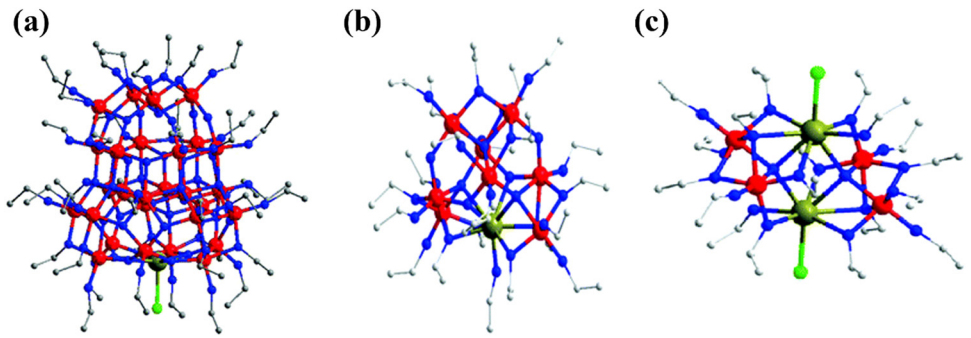

Fig. 24 M-POT structures with varying Ti : Ce ratios, (a) $[Ti_{28}O_{38}(OEt)_{38}(EtOH)_{1.4}CeCl]$, (b) $[Ti_8O_7(HOEt)(OEt)_{21}Ce]$, (c) $[\{Ti_2O(OEt)_8\}(EtOH{\cdot}CeCl)]_2$. Reproduced with permission from ref. 296 copyright 2013, Royal Society of Chemistry.

promising SSP options for TiO_2-based films, even facilitating lanthanide dopants such as Eu and Er.[299,300]

5.3.5 SSPs for co-catalysts. Multicomponent photoelectrodes containing co-catalysts can be fabricated from SSPs as an efficient, scalable method to produce multicomponent devices in a more viable, fewer-stepped approach. By using a dopant cation that is highly active as a water oxidation catalyst, and a compatible dopant with the bulk semiconductor, both doping and electrocatalyst loading benefits can be seen from a single precursor deposition.[301]

Dopant ions can also be mobile in a material, allowing them to migrate to the surface of the electrode during operation and remain there for future use. This is particularly important when the dopant is an excellent electrocatalyst, as their surface enrichment provides a means of depositing a photoanode-electrocatalyst multi-component device with a single precursor in a single deposition step. Expanding on complexes designed by Streb *et al.*,[302] Pike *et al.* synthesised a single-source trimetallic $BiVO_4$ precursor that could use any one of a range of metal dopants; $[Bi_2(DMSO)_6V_{12}O_{33}X]_2[M(DMSO)_6]$ (X = Cl, Br; M = Ca, Co, Ni, Cu, Zn).[259] Aside from the impressive success of using an SSP to deposit doped $BiVO_4$, the resulting Co-doped $BiVO_4$ photoelectrode showed a surface (6–9 nm) enrichment of Co after initial operation, providing a concentrated Co surface layer in the photoelectrode, known to enhance PEC water oxidation and photoanode stability. Interestingly the Zn-doped $BiVO_4$ film showed the greatest photocurrent response at 1.23 V *vs.* RHE (1.07 mA cm^{-2}, Zn > Co > Cu > Ni > Undoped), but Co-doped showed the earliest onset potential (0.4 V *vs.* RHE) and the highest photocurrent at potentials lower than 1.15 V *vs.* RHE, due to the enhanced catalysis at the enriched Co surface. Zn is considered a structural modifier for $BiVO_4$, hence a combination of Co and Zn dopants could combine the best properties of each of these M-doped films, since neither property is mutually exclusive. The Co-doped $BiVO_4$ multi-component photoelectrode was then used in a scaled up 300 cm^2 device, proving the method's viability for large scale production; a common flaw of many electrocatalyst loading techniques.

The efficiency of a catalyst is improved when used with a complementary material, for example, improved conductivity of NiOOH when combined with small fractions of FeOOH,[303] Ca^{2+} stabilising water oxidation intermediates of $CaMn_4$ clusters,[304] or Fe forming a highly oxidised state to act as a favourable surface for oxidised ligands to form on during Co- or Ni-based catalysis.[305] Zr is an emerging, unexplored partner to OER catalysts such as Co, providing protection from moisture as well as stabilisation of OER intermediates to reduce loss during catalysis. Novel SSPs with structures $[\{Zr_4(\mu_4\text{-}O)(OEt)_{15}\}Co(II)Cl]$, $[\{Zr_4(\mu_4\text{-}O)_2(EtO)_{16}\}(Fe(III)Cl)_2]$, $[\{Zr_4(\mu_4\text{-}O)_2(EtO)_{16}\}\{(Cu(II)Cl)_2(OEt)\}_2]$ were developed by Wright *et al.* for the solution deposition of catalyst-doped ZrO_2 films.[301] The Co-doped ZrO_2 film had the lowest Tafel slopes and onset potentials (at pH 14, 1 M KOH electrolyte), as expected given Co is considered one of the most efficient non-precious metal oxidation catalysts available. All three doped films showed a stable, homogeneous distribution of catalyst dopant particles throughout ZrO_2, an essential feature for electrocatalyst function as unstable dopant ions near the surface will be dissolved or reacted and the photoelectrode will lose the surface catalysis benefits.

5.3.6 SSPs for metal chalcogenides. Metal chalcogenides are p-type semiconductors that can be used as photocathodes, or layered with n-type semiconductors to form n–p or p–n heterojunctions.[306] Fabrication can be achieved through dual-source depositions, using one metal-containing precursor and one sulfur/selenium/tellurium containing precursor.[108,306,307] While this has proven effective, it carries the same dual-source issues discussed at the start of the section, higher amounts of impurity, and greater material costs and precursor synthesis times, as well as issues related to highly reactive precursor species such as metal alkyls and H_2S. The development of SSPs for direct deposition of metal chalcogenides is therefore of key interest for increasing the viability of such materials in PEC water splitting photoelectrodes. All reports of metal chalcogenide precursors specifically for PEC water splitting are listed in Table 6, although it is obvious that this is also a mostly unexplored area with lots of research potential. Thiolate ligands ($[R\text{–}S]^-$) such as thioamidates[241] and thioureides[242,243] are good choices for sulfur-based chalcogenide precursors due to the flexibility in the organic group structure for tailoring steric size, shape, polarity, composition, and molecular weight.[244]

Johnson *et al.* developed a family of 12 zinc thioureide systems, with general structures $[\{L\}ZnMe]$, $[\{L\}Zn\{N(SiMe_3)_2\}]$, and $[\{L\}_2Zn]$, where $H\{L\}$ = $^{i}PrN(H)CS(NMe_2)$, $CyN(H)CS(NMe_2)$, $^{t}BuN(H)CS(NMe_2)$, or $MesN(H)CS(NMe_2)$, as SSPs to ZnS films, choosing AACVD to overcome the limitations seen with developing chalcogenide precursors with high volatilities for CVD.[243] Viabilities for deposition were assessed by TGA. Many compounds showed multistep decompositions, with residual masses

Table 6 Reported novel structures synthesised for use as chalcogenide SSPs for PEC water splitting

Precursor[a]	Material	Deposition technique	Nanostructure	Substrate/temp/solvent	j^b/mA cm^{-2}	Ref.
$[Sn(\mu\text{-}NMe_2)\{SC(NMe_2)NC_6H_5\}]_2$	SnS	AACVD	500 nm triangular grains	FTO/375 °C/toluene	−0.92 (470 nm illumination)	242
$[\{PhC(O)Se\}_2SnBu_2]$	SnSe	Hot injection + dropcasting	Nanosheets	FTO/200/isopropanol	−0.011	308
$[Sb\{SeC(O)C_6H_5\}_3]$	Sb_2Se_3	Hot injection + dropcasting	Nanorod	FTO/200/isopropanol	−0.029, −0.662 at −0.6 V_{RHE}	125
$[Bi(SeOCPh)_3]$	Bi_2Se_3	AACVD	Nanosheets	FTO/200/$CHCl_3$	−0.082, −0.213 at −0.6 V_{RHE}	309

[a] Only the highest performing photoelectrode and precursor is listed from each literature report. [b] Photocurrent density measured at 0 V *vs.* RHE under 1 sun (100 mW cm^{-2}, AM 1.5G) solar simulation, unless stated otherwise.

lower than ZnS, suggesting some volatility, or lower than ZnS and Zn, suggesting high volatility. Volatility is not an issue for AACVD, however, it hides the useful decomposition data from TGA traces. $[\{^{t}BuN(H)CS(NMe_2)\}Zn\{N(SiMe_3)_2\}]_2$, showed the best TGA values (residual mass only 0.1% lower than extended, lowest onset temperature), but it contained a slow multi-step mass loss event after an initial rapid decrease. $[\{^{i}PrN(H)CS(NMe_2)\}_2Zn_2]$ was therefore identified as the most promising for application due to its single mass loss event at low onset temperature, as well as practical benefits including ease of synthesis, stability, and solubility in THF – all factors that need to be considered outside of what is theoretically the best.

Johnson *et al.* have also synthesised and compared three SSPs for CdS deposition, pyridine, bis-3-methylpyridine and bis-4-methylpyridine complexes of cadmium(II) ethylxanthate ($[Cd(S_2COEt)_2(Py)_2]$, $[Cd(S_2COEt)_2(3\text{-}MePy)_2]$, $[Cd(S_2COEt)_2(4\text{-}MePy)_2]$ respectively).[116] TGA profiles revealed single mass loss events for all three, however, the pyridine complex possessed the highest onset temperature and a residual mass significantly higher (11.5%) than that expected for CdS. The pyridine methyl compounds displayed similar thermograms, indicating that the position of the methyl group on the pyridine had negligible impact on thermal decomposition. Despite these similar TGA profiles however, the deposition of the methylpyridine derivatives were significantly different. The 3-MePy isomer grew dense aggregates of ~200 nm particulates at both 220 and 350 °C process temperatures, while 4-MePy had plate-like morphologies at both temperatures with larger crystallite sizes of 25–36 nm compared to 16–17 nm. Further, the 3-MePy deposit had a hexagonal phase at both temperatures, with preferential growth in [002] direction, whereas that for 4-MePy was amorphous at 220 °C and hexagonal phase at 350 °C, again favouring the [002] direction. This clearly identifies the dramatic influence that minor precursor structure can make on the deposited film, in this case it is suggested that differences in the basicity and steric demands of the two isomeric derivatives are the cause of these differences.

Sb_2Se_3 is a very newly emerging photocathode material for PEC water splitting, despite its application in microelectronics predating this by several years. Sb_2Te_3 has also been recently applied towards PEC water splitting, but as a HER co-catalyst instead of photoelectrode.[310] Reid *et al.* developed a series of alkylchalcogenostibines, $[Me_2SbSe^{n}Bu]$, $[MeSb(Se^{n}Bu)_2]$, $[Sb(Se^{n}Bu)_3]$ as SSPs for Sb_2Se_3.[311] LPCVD studies on all three precursors revealed $[MeSb(Se^{n}Bu)_2]$ as the most promising based on Sb : Se ratios close to the desired 1 : 1.5 value, and superior uniformity and coverage of deposit, likely due to its higher volatility. Substrate-dependent morphologies were observed, producing a high surface area film consisting of separated clusters on SiO_2, and a denser continuous thin film on TiN with lower surface area but higher surface coverage. Due to the success of this precursor, the tellurostibine analogue was synthesised as an SSP for Sb_2Te_3, requiring lower temperature for deposition (450 instead of 500 °C) but again seeing similar substrate-dependent morphologies, but on fused SiO_2 compared to PVD silica.

5.4 Clusters

While they can lead to issues due to formation of many thermal decomposition fragments, higher required process temperatures, and worse air/moisture sensitivities, metal clusters can prove effective precursors, not only for their promise as multinuclear complexes for SSPs, but also producing interesting and more complex thin film morphologies and crystal phases, features which can enhance performance in many ways, as discussed in Section 4.1. There is also more flexibility in design for larger complexes, such as varying metal composition, nuclearity, spatial arrangements, and functionalities.[312,313]

Eslava *et al.* used a $Ti_7O_4(OEt)_{20}$ titanium-oxo cluster that produced a unique desert rose anatase TiO_2 morphology when deposited using AACVD.[139] This morphology was found to favour the (010) facet, the most photocatalytically active orientation for anatase, without the need for any templating, and produced an anatase phase that was impressively stable up to an annealing temperature of 1000 °C. To investigate the effect of the cluster precursor, its thermal decomposition was compared to that of a common titanium precursor, titanium ethoxide ($Ti(OEt)_4$), in the same AACVD conditions. The simpler $Ti(OEt)_4$ structure has in a single-step volatilisation, whereas $[Ti_7O_4(OEt)_{20}]$, as expected for a cluster, showed a more complex 3-step decomposition pathway that settled on the target TiO_2 weight percentage (Fig. 25a and b). For $[Ti(OEt)_4]$, only the alkoxy groups must break off to reveal the Ti core for TiO_2 growth, whereas in $[Ti_7O_4(OEt)_{20}]$ the alkoxy groups need to be removed, and the Ti–O–Ti bonds need to be broken. The resulting TiO_2 morphologies can also be linked back to the difference in precursor structures, with $[Ti(OEt)_4]$ growing randomly distributed particles of irregular shape due to rapid decomposition, while $[Ti_7O_4(OEt)_{20}]$ grew the ordered and more complex structured desert rose, likely due to the influence of its large, sterically hindering ethoxide groups acting as barriers to growth around a single Ti growth site (Fig. 25c and d). As previously described in Section 4.1, the desert rose morphology also increases the light absorption efficiency due to reabsorption of scattered photons, particularly important for lighter/white coloured films such as TiO_2.[133]

Another report by Eslava *et al.* used $[Ti_{16}O_{16}(OEt)_{32}]$ clusters with graphene oxide sacrificial templates to create nanoflakes that could act as spontaneous photocatalysts for hydrogen evolution when suspended in a methanol hole scavenging solution.[314] This shows the versatility that polyoxometalate clusters possess for use within the PEC and PC field.

5.5 Polymorph control

The polymorph, or phase, of a deposited film is heavily influenced by the thermal decomposition pathway of the precursor, and the temperature along that pathway that the deposition process uses. Precursors with minor differences in molecular structure can therefore yield different polymorphs due to the differing decomposition pathways. Boyle *et al.* produced a series of calcium aryloxide precursors for the fabrication of calcium ceramics, and used thermogravimetric analysis (TGA) to explain the different polymorphs seen for different molecular structures

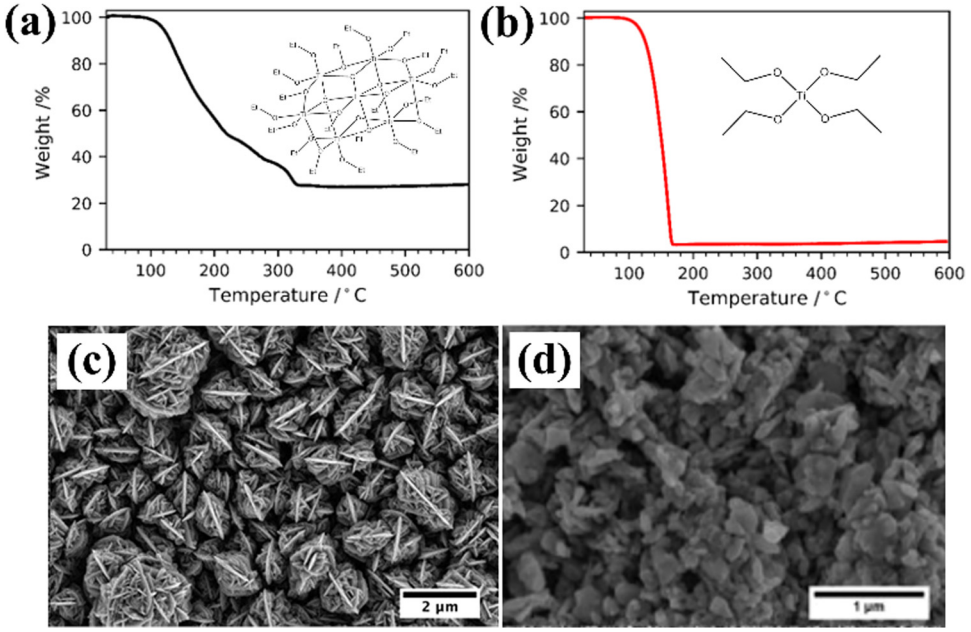

Fig. 25 Thermogravimetric analysis data for (a) $[Ti_7O_4(OEt)_{20}]$, (b) $[Ti(OEt)_4]$, inserts show the respective molecular structures; and SEM micrographs of films deposited using 0.35 M concentration of precursors (c) $[Ti_7O_4(OEt)_{20}]$, (d) $[Ti(OEt)_4]$. Reproduced with permission from ref. 139 copyright 2019, Royal Society of Chemistry.

(Fig. 26).[315] Compound 3 (Fig. 26a) is seen to cleanly decompose (a single, fast mass loss event) in two distinct steps either side of the process temperature (200 °C), hence the precursor will decompose cleanly with no ongoing decomposition during the deposition. The flatter, stable section between the major mass-loss events at the process temperature favours a thermodynamically stable phase, which matches the portlandite phase seen experimentally, independent of the processing route.

Conversely, the TGA for compound **4a** (Fig. 26b) contains many small weight steps with no stable, flat segments, indicating a more complex decomposition with many different steps and pathways. There are therefore ongoing decomposition events occurring at the process temperature, causing the kinetically favoured phases to be trapped instead of providing enough time for thermodynamic stability. Again, this was confirmed experimentally by the deposition of the vaterite phase when using compound **4a**. To further confirm this phase-decomposition correlating theory, both precursors were deposited at elevated temperatures for prolonged times, now yielding the thermodynamically stable portlandite phase for both. This is as expected for compound 3 as it is already in the most stable state, and compound **4a** now is being processed at a temperature above the more complex mass-loss events and instead in a smooth region on the TGA trace.

Exploring the exact thermal decomposition mechanism helps to understand how different polymorphs and purity can be selectively formed through chosen deposition temperature. Johnson *et al.* studied the thermal breakdown of a novel tin thioureide SnS precursor, $[Sn(\mu\text{-}NMe_2)\{SC(NMe_2)NC_6H_5\}]_2$.[242] Interestingly, deposits of α-SnS were formed at deposition temperatures of 375 °C, compared to ZB-SnS at 300 °C, which one may expect given that ZB-SnS is the thermodynamically unstable phase, but more kinetically stable phase, compared to α-SnS. TGA revealed a two-step thermal decomposition event (Fig. 27a), an initial minor drop at ~270 °C followed by a rapid, complete drop to the expected residue that onsets during the first event but only reaches peak rate of mass loss at ~315 °C.

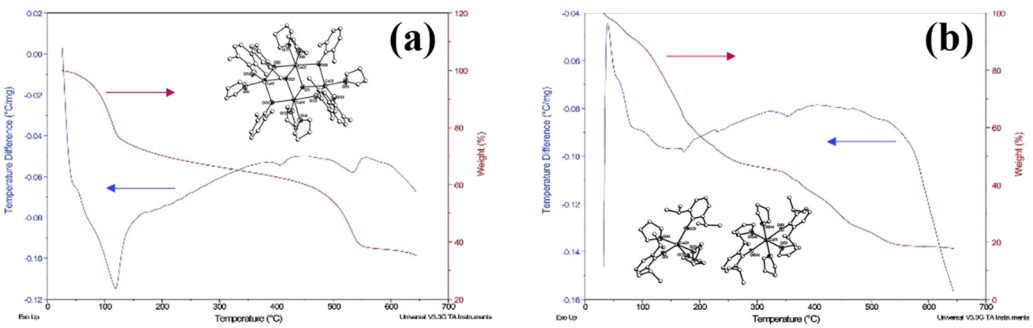

Fig. 26 Differential thermal analysis (blue) and thermogravimetric analysis (red) traces for (a) compound **3**, (b) compound **4a**. Inserts show the molecular structures. Reproduced with permission from ref. 315 copyright 2007, American Chemical Society.

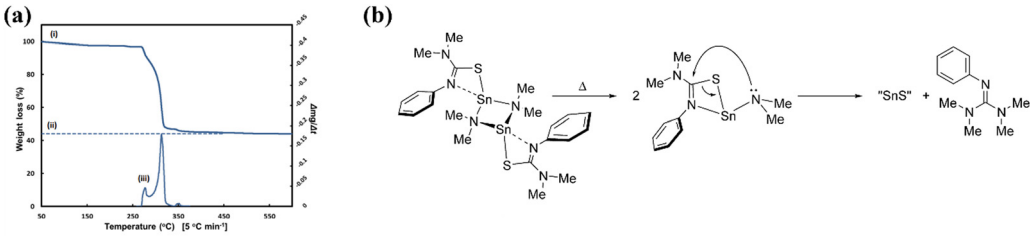

Fig. 27 (a) TGA of $[Sn(\mu\text{-}NMe_2)\{SC(NMe_2)NC_6H_5\}]_2$, and the derivative of mass loss with respect to temperature to identify significant mass loss events, (b) suggested SnS formation mechanism from initial precursor. Reproduced with permission from ref. 242 copyright 2015, American Chemical Society.

Using similar theory to that discussed by Boyle *et al.*, using a process temperature that facilitates multiple ongoing decomposition events will trap the kinetically favoured phase, as is the case for 300 °C here. The precursor was found to form a dimer complex in solid state, however, evidence from high temperature (323 K) ^{119}Sn NMR studies suggested that the dimer complex breaks down into its monomeric species at elevated temperatures. The nucleophilic $\{NMe_2\}$ group on the Sn centre is then free to attack the $\{NMe_2\}$ group at the central carbon. This was reinforced by the identification of a matching phenyl guanidine species by ^{13}C NMR spectroscopy of the cold-trapped CVD by-products from a 375 °C deposition process, implying that at this temperature decomposition occurs in a single reaction step (Fig. 27b) likely matching the larger mass loss event seen in TGA, whereas at 300 °C there is contributions from another decomposition, however, the decomposition by-products at this temperature were not examined in the study.

5.6 Nanostructure control

Structural design of precursors is a key technique for controlling the morphology of thin films, particularly within multi-nuclear precursors where preferential film growth directions can be more easily controlled. The benefits of morphological control were outlined in Section 4.1.1. The precursor structure argument (PSA) treats precursors as building blocks to direct the final morphology formed, with many literature reports highlighting its effectiveness.[316–319] Boyle *et al.* developed a Ca framework of 2 face-shared cubes, each with opposite corners missing (Fig. 28), depositing a nanorod morphology in both solution and solvothermal depositions.[315] The organic moieties are removed during Ca deposition, leaving the double cubic structure which will grow significantly easier/faster in the direction where corners are not missing, fabricating particles with greater length in one direction than the other; rods. Similar ZnO work expands on this structural argument for the influence of the central multi-nuclear core of the precursors, using Zn cores with increasing nuclearity and steric size to deposit nanorod morphologies with increasing rod thickness to match the core structure.[319]

Cd chalcogen precursors have also been used to a similar extent,[318] showing how morphological changes are possible based on the influence of decomposition by-products which poison and promote different growth planes, however, the ability to control this outside of trial and error is limited. The chalcogen used (S, Se, Te) also impacted the final morphology (sphere, rod, sphere respectively), hence the control of the morphology relies on all different parameters within the precursor molecular structure: metal core structure, ligand choice and its decomposition fragments, and the chalcogen (or oxygen) choice for M–L bonding.

An option for controlling film morphology through precursor molecular structure without requiring multi-nuclear complexes is with multidentate ligands with strong M–L bonds, for example, M-alkoxide bonds as described previously. The slower thermal decomposition process means that at any instance during film growth, when the metal centre has bound to the substrate or growing film surface, each M–L bond will break in distinct, time separated events, leaving the ligand, or remaining fragment of ligand, bound but in a different position around the metal and occupying space within the growing film, therefore creating a porous structure.[288] This method has less control over the exact shape of the nanostructure morphology; however, it is complementary with previously described benefits to chelating ligands, and can be achieved with low-nuclear complexes.

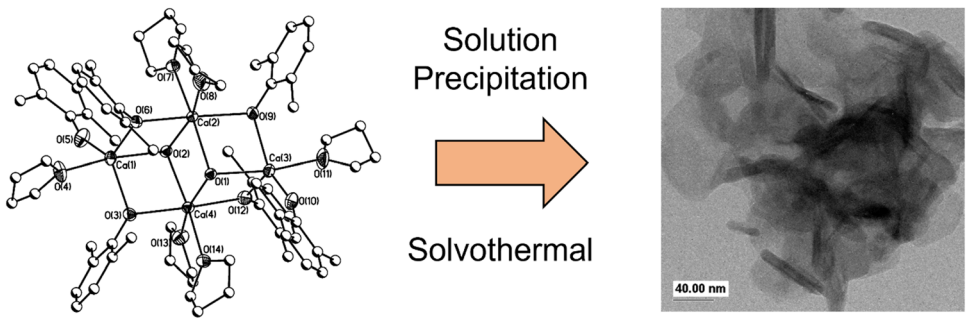

Fig. 28 Structure plot of a Ca framework designed to fabricate nanorod morphology, with TEM image of a nanorod cluster produced *via* solution precipitation route. Reproduced with permission from ref. 315 copyright 2007, American Chemical Society.

To effectively control elongated morphology (essential for high surface area, thicker films), the rate of nucleation site generation during precursors decomposition must be limited, while maintaining sufficient feedstock to continue growth, and without the process taking too long or requiring too much precursor.[320] Highly reactive precursors lead to rapid deposition, but an overload of nucleation sites results in uncontrolled film growth.[317] The use of the stronger M–O bonds compared to M–N tends to favour this reduction in reactivity just enough for controlled growth, however, it may vary depending on the ligand, the metal, and the amount of steric hindrance.

6. Further photoelectrode performance enhancement

So far, the review has detailed ways to design and tailor molecular precursors to deposit a high-performance film with controlled and desired properties. To make a competitive photoelectrode, additional, post-deposition modifications can and must be made to further increase performance and maximise efficiencies. There are numerous approaches that can be applied to increase the complexity of the device, and usually a combination of many will be used. Here, the three most common methods will be outlined, however, there are countless other modifications that can be made, including sensitizer incorporation, deposition of a blocking layer, protective layer, passivating layer and charge transport layer, and tandem cell configurations.

6.1 Heterojunction formation

Charge carrier recombination is a dominant source of efficiency loss in most photochemical devices, but one common and highly effective method for enhancing the properties of a device against this is by layering one semiconductor on top of another, known as a heterojunction, or composite semiconductor. There are many variations of heterojunctions, distinguished in two ways: (i) whether the majority charge carriers present in each semiconductor are the same (p–p or n–n heterojunction) or opposite (p–n or n–p heterojunction), known as isotype and anisotype heterojunctions respectively;[321] (ii) by the relative band positions of each semiconductor (Fig. 29), if both bands of one semiconductor are straddled by those of the other, it is Type-I, if only one of the VB or CB of one semiconductor is straddled by both bands of the other, it is Type-II, and if one has both bands above the CB of the other, it is Type-III.[322] Type-I heterojunctions show no improvement to charge carrier separation since all carriers are accumulated onto semiconductor B, whereas Type-II and Type-III junctions result in spatially separated holes and electrons, reducing recombination and increasing lifetimes.[323]

Further, heterojunctions can be created for multiple functions, such as employing a protective layer that has compatible band positioning, or using a second semiconductor with a significantly different band gap that will absorb photons of energy too low for the original semiconductor, or too large resulting in energy losses to nonradiative relaxation, hence utilising the available photon energy range more efficiently. It is important to note that the second semiconductor layer used to create the heterojunction can also be designed using bespoke precursors as outlined in Section 5, resulting in two or more semiconductors developed and optimised in this way. The additional layer should therefore be fabricated on its own first to ensure the best precursor structure and deposition conditions/technique are found prior to layering.

ALD is an outstanding technique for depositing heterojunction layers due in part to its high aspect ratio deposition, meaning the carefully designed, high surface area morphology of the initial semiconductor layer is not filled by the second material, but rather uniformly coated to maintain shape and surface area. The highly controllable thickness of deposition is also essential for optimisation of the two layers, as often the second layer in a heterojunction is only there for charge separation and surface passivation. It is also a chemisorption-based process, ensuring intimate contact between the layers and hence more rapid carrier injection across the interface.[56,324–326]

In recent work by Johnson *et al.*, a TiO_2 nanorod system was coated with NiO using ALD to form a TiO_2/NiO heterojunction, yielding significantly increased photocurrents at all potentials and a conformal NiO coating was observed that maintained the morphology and high porosity of the TiO_2 nanorods (Fig. 30).[327] Barecca *et al.* used ALD to coat TiO_2 onto a chemical vapour deposited Fe_2O_3 film, forming an intimately contacted TiO_2-stabilised heterojunction with a 10-fold photocurrent increase due to the enhanced charge separation and transfer.[328,329] ALD can also be used to deposit hybrid materials using either single-source or dual-source precursors. Fe_2TiO_5, for example, was

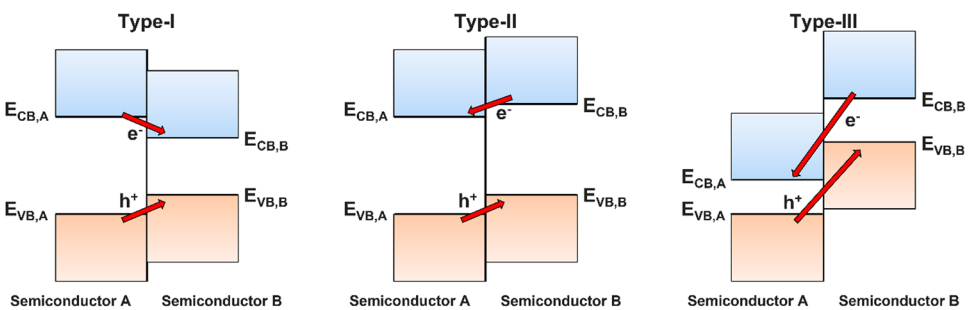

Fig. 29 Variations of heterojunction based on energy band alignments.

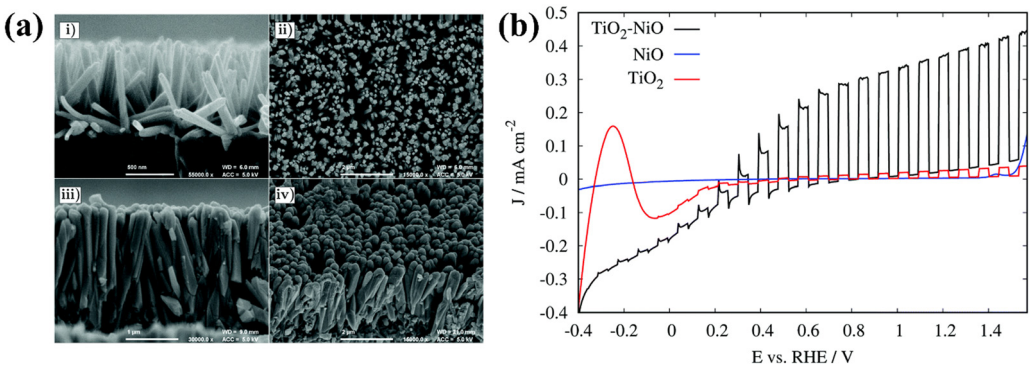

Fig. 30 (a) Scanning electron microscopy images of TiO_2 nanorods before (above) and after (below) NiO ALD coating, (b) photocurrent densities measured under chopped 1 sun rear-side illumination for TiO_2, NiO, and NiO-coated TiO_2 systems. Reproduced with permission from ref. 327 copyright 2021, Royal Society of Chemistry.

deposited onto an Fe_2O_3 film to increase photocurrent performance by up to 3.5-fold.[330]

6.2 Annealing

Post deposition annealing is a useful tool to remove carbon contamination from the deposition, increase the crystallinity of the film to increase conductance, alter film or nanoparticle shape and size, and convert the material phase to a more thermodynamically favoured phase.[95] Annealing can also be undergone in a range of environments to modify the oxygen content within the film in whichever direction is required for that material. An air environment is oxidative, hence oxygen deficient as-deposited films can be air-annealed to ensure correct stoichiometry.[231] Annealing in a vacuum or hydrogen environment is reductive, hence it is possible to increase the oxygen deficit/number of oxygen vacancies which can enhance PEC properties of some metal oxides, such as charge carrier generation and separation, by effective vacancy doping.[331] TiO_2, which forms Ti^{3+} centres with oxygen vacancies, has been reported to have significantly greater PEC performance after hydrogen or vacuum annealing, and vacuum annealing has also been shown by Marken *et al.* to change the material selectivity from oxygen evolution to chorine evolution in the presence of chloride ions.[13,151]

6.3 Co-catalyst loading

The principles of co-catalyst loading have already been covered in Section 4.2, and it should be stated that for almost any real-world device it is essential to have co-catalysts, however, what form this takes can vary between thin films, nanoparticles, and surface-level doping. Thin films are often the chosen option when the co-catalyst has greater stability than the pristine film, good charge transport properties, and preferential energy band alignment with the material below, for example, with WO_3-coated $BiVO_4$, such that the loading not only improves surface charge transfer, but also acts as a protective layer and a component in a heterojunction for enhanced bulk charge transfer.[92,332]

Catalyst doping, particularly at the surface, can be used to combine the enhancement associated with doped materials (*i.e.* narrower bandgap, better charge transport, reduced recombination) with the improved surface transfer and catalysis kinetics associated with co-catalysts, however, it is only viable for catalyst species that are compatible for doping with the bulk material, and when the bulk material is already chemically stable enough during operation since additional protective layers will render the catalyst dopant pointless.[333,334] Case studies for SSP catalyst doping were covered in Section 5.3.5. It also facilitates the fabrication of the overall device in fewer steps without the need for a separate process to load catalyst on the surface, which is always preferential when moving towards commercialisation. Finally, nanoparticles are typically the only option when precious metal catalysts are required, since the high cost and rarity limits the quantity of metal that can be used for a realistic device, while still providing as many active sites through exposed catalyst surface area as possible.[335,336]

Deposition of cocatalysts often uses common precursors and simple methods, however, the same principles for precursor design may be taken into consideration to design an efficient co-catalyst loading process, either as a distinct additional deposition process or in the same process as photoelectrode deposition. Table 7 shows examples of literature reporting novel precursor design of electrocatalysts for water splitting.

Devi *et al.* used three Ir precursors (Fig. 31) that had been tailored for high volatility and thermal stability to suit deposition *via* MOCVD, and to create a highly catalytically efficient Ir coating method for oxygen evolution enhancement.[339] Thermal evaluation of each precursor by TGA led to conclusion of [Ir(COD)(DPAMD)] being the most promising, owing to its decomposition to the residual weight of crystalline metallic Ir (confirmed by PXRD) at suitably low temperatures. By varying the deposition time from 3.25 min to 30 min, the microstructure of the deposits was controllable, ranging from nanoparticulate deposition to a continuous thin film respectively, allowing for tailoring of the electrocatalyst form to suit the underlying material, as discussed earlier in the section.

Coupling co-catalysts with complementary materials can enhance their effectiveness. Zr-based mixed metal oxides are an emerging system for use in stable, low-cost, and earth abundant electrocatalyst coatings. Zr^{4+} has a high charge density, making it strongly Lewis acidic, a trait known to stabilise water oxidation intermediates during catalysis.[340,341] It is therefore promising to couple Zr with an effective OER catalyst, such as Co, into a single

Table 7 Reported novel structures synthesised for use as electrocatalyst precursors

Precursor	Material	Deposition technique	Catalytic activity	Overpotential[a]	Tafel slope[b]	Ref.
$FeMn(CO)_8(\mu\text{-}PH(\mu\text{-}PH_2)$	FeMnP	MOCVD	OER	280	57	337
$[Ni_4(HL)_4(OAc)_4]$ H_2L = 2,6-pyridinedimethanol	NiO_x	Electrodeposition	OER	380–400	42	338
$[Ti_2(OEt)_9(NiCl)]_2$	NiO_x/TiO_2	Spin coating	OER	Increased WO_3 photocurrent at low bias	—	98
[Ir(COD)(DPAMD)] COD = 1,5-cyclooctadiene DPAMD = *N*,*N*′-diisopropyl-amidinate	Ir	MOCVD	OER and HER	HER: 50	HER: 41	339
$[Bi(SeOCPh)_3]$	Bi_2Se_3	AACVD	OER and HER	OER: 385 HER: 220	OER: 122 HER: 178	309
$[\{Zr_4(\mu_4\text{-}O)(OEt)_{15}\}Co^{II}Cl]$	Co–ZrO_2	Solution deposition	OER	430	54	301

[a] Overpotential measured at 10 (−10) mA cm^{-2} for the OER (HER)/mV. [b] Tafel slope measured at 10 (−10) mA cm^{-2} for the OER (HER)/mV dec^{-1}.

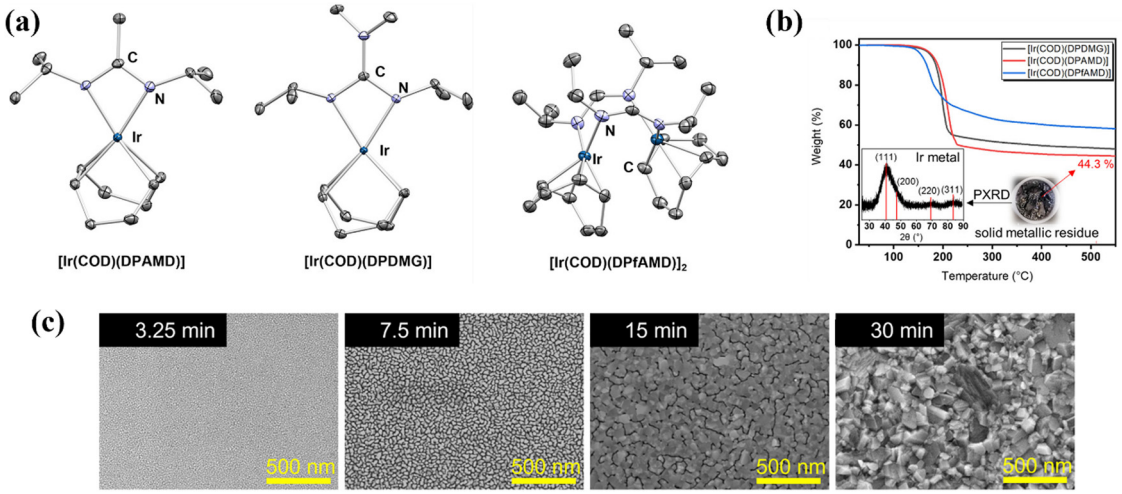

Fig. 31 (a) Structures of three bespoke Ir precursors, (b) TGA curves for the three complexes with PXRD of the residue for [Ir(COD)(DPAMD)], (c) SEM images of the Ir film deposited from [Ir(COD)(DPAMD)] with varying deposition times. Reproduced with permission from ref. 339 copyright 2022, American Chemical Society.

mixed-metal oxide system for improving surface water oxidation at the photoanode. Wright *et al.* developed three SSPs, $[Zr_4O(EtO)_{15}Co(II)Cl]$, $[Zr_4(O)_2(EtO)_{16}Fe_2(III)Cl_2]$, $[Zr_4(O)_2(EtO)_{18}Cu_4(II)Cl_4]$, for the deposition of first-row transition metal-doped ZrO_2 thin films Co–ZrO_2, Fe–ZrO_2, Cu–ZrO_2 respectively, as discussed in Section 5.5.5.[301]

7. Overall device design and characterisation

The most significant device properties, design methods to control them, and techniques to measure each are outlined in Table 8. It should be noted that molecular precursor design can influence all these properties, as discussed throughout Section 5, however, for a commercial device it is beneficial to combine precursor design with other techniques to obtain vastly greater performances than any device design method could on its own.

8. Conclusions and outlook

8.1 Summary

The most crucial factor affecting the composition and structure of a semiconductor is the precursor itself.[244] Bespoke precursor development for semiconducting thin films is a well explored field, with the overwhelming benefits already proven in areas such as microelectronics, however, it has yet to be significantly introduced to PEC water splitting, despite similarities in many design requirements. Similarly, extensive PEC studies on complex multi-component devices are reported regularly, but using untailored, commercially available precursors for material fabrication. The quality of research and expertise within these two fields individually is exceptional, hence if collaborations can be made to link the two areas together, the potential research output could have remarkable impact, producing higher performance devices as well as using a more systematic, informed approach to gain valuable knowledge for the benefit of future development and progression.

Table 8 Techniques to enhance major PEC device properties other than bespoke molecular precursor design

Device property to enhance	Design method	Measurement technique
Light absorption	Heterojunction Doping Nanostructure	PEC efficiency (STH, IPCE) UV/Vis spectroscopy (Tauc plot – bandgap measurement)
Bulk charge separation	Heterojunction Doping Morphology (surface area, nanostructure, orientation)	Impedance Mott Schottky plot (charge carrier density)
Surface charge transfer	Co-catalyst loading Doping Interface passivation	Hole/electron quencher PEC measurements
Grain size	Nucleation rate, annealing	XRD (Scherrer equation)
Bulk carrier mobility	Annealing Doping	Impedance
Morphology (surface area, nanostructure, orientation)	Templating, additives, deposition method and conditions (temp., prec. conc., solvent)	SEM, TEM, EBSD
Chemical and photo-stability	Protective layer Electrolyte choice	Chronoamperometry
Material phase/polymorph	Temperature of deposition and annealing	XRD Raman spectroscopy

The ligand structure on a precursor not only influences its own properties for tailoring towards specific deposition techniques and conditions, but also the resulting deposit structure, composition, and performance. The thermal decomposition and removal of the ligand is therefore key to precursor development. The molecular structure should provide the precursor with favourable properties for handling and deposition, while being thermally decomposed and removed rapidly at low temperatures, ideally as a gas phase by-product or an inert species that will not act as a contaminant source, react with starting precursor, or negatively impact the crystal growth. The more complex the precursor, the greater the complexity of thermal decomposition and fragmentation, which can be detrimental to film growth, but can also result in unique physical properties that are unseen in standard common precursor uses.

The general requirements of any precursor, novel or not, are purity, stability, low-toxicity, ease and scale of synthesis, and cost. From there, specialised precursors can be designed to target more tailored properties, such as thermal decomposition kinetics and pathways, volatility/solubility, deposit morphology, deposit crystal phase and orientation, and homogeneity in single and mixed materials. The physical features of the photoelectrode, such as morphology and polymorph composition, are becoming increasingly important as research advances. The use of templating, additives, etching, and post-deposition treatment can achieve good control over these properties; however, all these options also increase production time and costs, limiting scalability. Tailored precursors offer excellent control over the physical features of the deposit without the need for additional fabrication steps or chemicals, vastly increasing the potential for scaling to commercial and industrial application.

Precursor development is not necessarily reliant on planning the perfect structure from the start, but instead designing a base structure that should provide the desired properties, followed by ongoing refinement of this structure to progressively achieve more effective performance in optimal deposition conditions, and composition and structure of the photoelectrode deposited. Such refinement processes are not possible with commercial, pre-made precursors. Several case studies that exemplify this iterative structure refinement have been discussed throughout the review.

Transition from lab scale to commercial must be considered when designing new precursors and materials if the technology is to become viable. High STH efficiencies are not industrially meaningful unless the device can be effectively scaled to yield high H_2 production rates. Both the precursor synthesis and the deposition techniques must therefore be chosen carefully to ensure suitability for batch production across large surface areas. CVD techniques have been proven for large scale production already, and are well suited to the use of new and multiple precursors, hence it is likely that CVD will dominate material production in the future, and why it has been the focus of this review compared to alternative deposition methods.

Herein, it has been described how bespoke precursor development is an invaluable tool for the tailored optimisation of each property within a semiconductor. Compatibility between precursors is required for doping, hybridisation, and any other simultaneous use, which is more effective and more easily controlled using molecular structures that have been specifically designed for simultaneous use. Alternatively, single-source precursors can overcome many issues associated with combining multiple individual precursors, such as a simpler deposition process, fewer film defects, and greater homogeneity of deposition, however, the

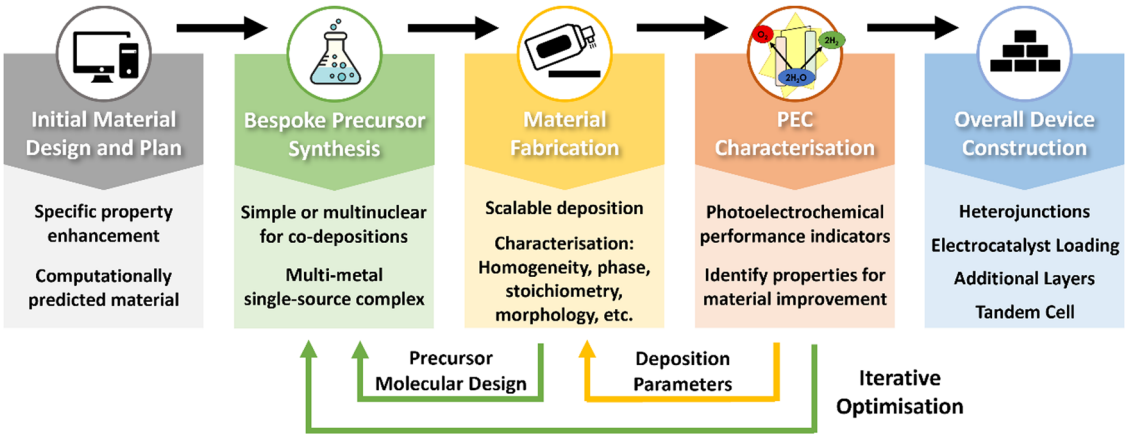

Fig. 32 An idealised complete interdisciplinary workplan and work packages for photoelectrode development.

multinuclear, larger complexes used requires an even greater focus and control on molecular structure and behaviour; hence such precursors are usually only effective when they have been well-designed for purpose, which demands a strong understanding of, and consideration towards, design requirements. This field can therefore be expanded by the inclusion of synthetic chemists and collaboration between an interdisciplinary team, splitting photoelectrode development and characterisation into: (i) planning and design of the desired material(s)/electrode; (ii) bespoke precursor synthesis; (iii) precursor deposition; film characterisation, and iterative optimisation; (iv) photoelectrochemical characterisation; and (v) additional complexity towards an overall multicomponent photoelectrode device (Fig. 32).

The current absence of work on tailoring for water splitting photoelectrodes provides clear and strong evidence for the importance and timeliness of this review, highlighting the benefits of tailored precursors towards: (i) suitability for deposition and optimising required deposition conditions; (ii) resulting thin film properties that can enhance overall water splitting performance; (iii) providing unique properties to thin films that are unseen in commercial precursors; (iv) progressive, iterative improvements to precursors; (v) gaining more valuable long-term knowledge and understanding from systematic precursor designs for future development. All this together shows that the only way to achieve the target of a cost-effective, stable, highly efficient PEC device is by combining the expertise available across a range of disciplines.

8.2 Future outlook

The overall aim for this field is to create a highly efficient PEC device that is cost-effective and stable long-term.[59] It has been concluded that individual semiconductors are not capable of this – TiO_2 is cheap and stable but has poor carrier generation, $BiVO_4$ is effective at carrier generation but has slow bulk and surface transport, Cu_2O has high PEC efficiencies but is unstable. It is therefore clear that not only does each material need to be maximised in its own performance, combinations of materials through doping, hybridisation, layering, and co-catalyst loading will be essential to achieving this target. At present, there is a significant disparity between theoretical maximum efficiency and practical performance, particularly in photoanodes which are limited by the sluggish OER kinetics. The only way to achieve the development of new, better, and more complex materials, using existing deposition techniques, is through new, systematic precursor design. This would switch to a more 'bottom-up', fundamental approach towards systematic photoelectrode material development, focusing on the development and optimisation of individual materials, using suitable precursors such that they can be combined to then fabricate more complex devices with already highly optimised individual components. The use of techniques such as AACVD allows for greater precursor design flexibility, particularly for large, complex, multinuclear precursors that can be used as SSPs for advanced materials.

Consequently, new materials are emerging as promising next generation photoelectrodes to either replace or supplement the more ubiquitous materials such as TiO_2. In fact, there is excellent compatibility between bespoke precursor design and the fabrication requirements for many of these next generation materials. Hybrid and complex materials such as Fe_2TiO_5,[342] perovskites,[343] and organic polymers[344] are among the alternatives. Additionally, computational studies can be used to predict new materials with a myriad of multi-metal elemental compositions as promising next generation photoelectrodes.[345–347] It is therefore clear that having a library of already compatible precursors for a wide range of different metal species which can be dropped in and instantly used effectively would be invaluable, not only for reducing the time required to develop an optimised process for each new material, but also improve the quality of deposition using precursors already tailored for this function. In this way, computationally predicted new materials can be quickly and effectively experimentally screened as potential candidates, and those that show promise can then be examined further, with additional tailored precursors, including SSPs, being synthesised specifically for property optimisation of that individual material.

High entropy and entropy-stabilised inorganic materials are a recent development, but show great promise in a range of energy and catalysis applications, including photoelectrochemical water

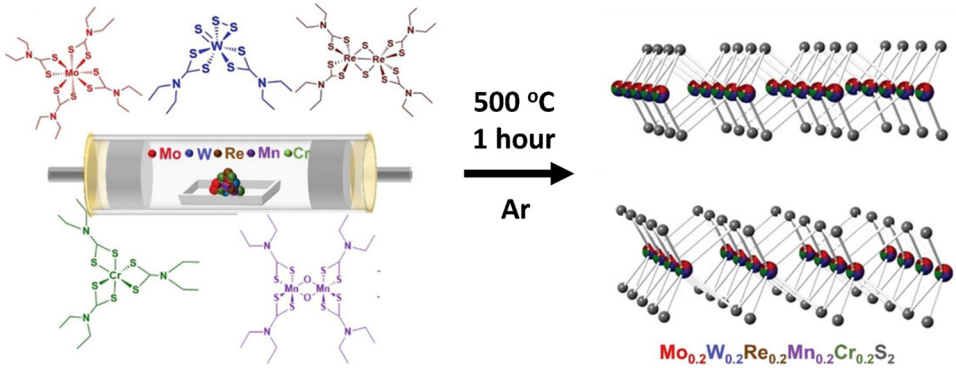

Fig. 33 Schematic of the preparation of a high entropy transition metal disulfide by the thermal decomposition of five precursor powders in tandem. Reproduced with permission from ref. 350 copyright 2023, Wiley-VCH.

splitting.[348] Often containing greater than five principal metal elements incorporated into a single disordered phase, this class of materials show unique and promising structures and properties conducive towards use in highly efficient photoelectrodes.[349] Current synthesis procedures use high temperature and multi-stepped methods, often using solid state synthetic strategies from the constituent elements, however, simpler and more scalable routes using metal precursors have also been explored, for example in the work by Lewis *et al.*,[350] where precursors were decomposed in tandem to form a high entropy transition metal disulfide material (Fig. 33).[351,352] The simultaneous application of a collection of bespoke and compatible metal precursors, or the development of a multinuclear SSP containing five or more different metals, could be an effective, scalable fabrication route for these materials, particularly with a lower temperature deposition technique such as AACVD followed by high temperature post-treatment to ensure single-phase formation.

All-in-all, the PEC water splitting field is currently dominated by materials scientists and electrochemists, however, there is a large absence of precursor design for material development, which requires inorganic chemists to fill, if the technology is to progress further and become viable and successful. This inter-disciplinary approach is an untapped research field, ripe for further development and discovery; and it will only grow in both size and importance as green hydrogen is increasingly introduced and integrated into society. Now is the time to get involved and realise its potential. This review links the two sides of PEC water splitting to encourage a more inter-disciplinary approach that can push PEC water splitting into new frontiers of understanding and performance.

List of abbreviations

0D, 1D, 2D, 3D	Zero/one/two/three-dimensional
AACVD	Aerosol-assisted chemical vapour deposition
ALD	Atomic layer deposition
a-TiO_2	Amorphous TiO_2
CB	Conduction band
CBM	Conduction band minima
CBTS	Cu_2BaSnS_4
COD	1,5-Cyclooctadiene
CVD	Chemical vapour deposition
CZTS	Cu_2ZnSnS_4
DCM	Dichloromethane
DME	Dimethoxyethane
DMSO	Dimethylsulfoxide
DPAMD	*N*,*N*′-Diisopropyl-amidinate
EBSD	Electron backscatter diffraction
EIS	Electrochemical impedance spectroscopy
Et	Ethyl group
FE	Faradaic efficiency
FTO	Fluorine-doped tin oxide
GC-MS	Gas chromatography–mass spectroscopy
HER	Hydrogen evolution reaction
HOMO	Highest occupied molecular orbital
IPCE	Incident photon to current conversion efficiency
^{i}Pr	Isopropyl group
LPCVD	Low-pressure CVD
LUMO	Lowest unoccupied molecular orbital
Me	Methyl group
MI-IR	Matrix-isolation infrared (spectroscopy)
MOCVD	Metal–organic chemical vapour deposition
M-POT	Metal-doped polyoxotitanate
NMR	Nuclear magnetic resonance (spectroscopy)
OAc	Acetate
OER	Oxygen evolution reaction
PC	Photocatalysis
PEC	Photoelectrochemical
Ph	Phenyl group
POM	Polyoxometalate
POT	Polyoxotitanate
PSA	Precursor structure argument
PV	Photovoltaics
PV–E	Coupled photovoltaics–electrolysis
PXRD	Powder X-ray diffraction
Py	Pyridine
RHE	Reversible hydrogen potential
SEM	Scanning electron microscopy

SHE	Standard hydrogen potential
SSP	Single-source precursor
STH	Solar to hydrogen conversion efficiency
^{t}Bu	*tert*-Butyl group
TEM	Transmission electron microscopy
TFA	Trifluoroacetate
TGA	Thermogravimetric analysis
THF	Tetrahydrofuran
TMP	Transition metal phosphine
VB	Valence band
VBM	Valence band maxima
XRD	X-ray diffraction

List of symbols

E	Potential
e^-	Electron
E_F	Fermi level
E_{redox}	Electrolyte redox potential
h^+	Hole
j_{photo}	Photocurrent density
V_{on}	Onset potential
V_{plat}	Plateau potential
φ^{ox}	Oxidation potential
φ^{red}	Reduction potential

Conflicts of interest

There are no conflicts to declare.

Acknowledgements

We gratefully acknowledge the financial support of the University of Bath and University of Monash, and the provision of a Bath/Monash PhD studentship to T. R. H. L.; C. L. B. is the recipient of an Australian Research Council (ARC) Discovery Early Career Researcher Award (DECRA, project number DE200101076), funded by the Australian Government.

References

1 Energy Institute, 72nd Statistical Review of World Energy, 2023.
2 J. Tsao, N. Lewis and G. Crabtree, *Solar FAQs*, US Department Energy, 2006, 1–24.
3 S. Wang, A. Lu and C.-J. Zhong, *Nano Convergence*, 2021, **8**, 4.
4 W. Yang, R. R. Prabhakar, J. Tan, S. D. Tilley and J. Moon, *Chem. Soc. Rev.*, 2019, **48**, 4979–5015.
5 N. Nitta, F. Wu, J. T. Lee and G. Yushin, *Mater. Today*, 2015, **18**, 252–264.
6 G. Girishkumar, B. McCloskey, A. C. Luntz, S. Swanson and W. Wilcke, *J. Phys. Chem. Lett.*, 2010, **1**, 2193–2203.
7 I. Staffell, D. Scamman, A. V. Abad, P. Balcombe, P. E. Dodds, P. Ekins, N. Shah and K. R. Ward, *Energy Environ. Sci.*, 2019, **12**, 463–491.
8 J. Chi and H. Yu, *Chin. J. Catal.*, 2018, **39**, 390–394.
9 M. K. Singla, P. Nijhawan and A. S. Oberoi, *Environ. Sci. Pollut. Res.*, 2021, **28**, 15607–15626.
10 D. J. Durbin and C. Malardier-Jugroot, *Int. J. Hydrogen Energy*, 2013, **38**, 14595–14617.
11 Internal Atomic Energy Agency, Hydrogen Production Using Nuclear Energy, 2013.
12 Z. Li, S. Fang, H. Sun, R. J. Chung, X. Fang and J. H. He, *Adv. Energy Mater.*, 2023, **13**, 1–26.
13 T. R. Harris-Lee, Y. Zhang, C. R. Bowen, P. J. Fletcher, Y. Zhao, Z. Guo, J. W. F. Innocent, S. A. L. Johnson and F. Marken, *Electrocatalysis*, 2021, **12**, 65–77.
14 C. Palmer, F. Saadi and E. W. McFarland, *ACS Sustainable Chem. Eng.*, 2018, **6**, 7003–7009.
15 B. Mei, G. Mul and B. Seger, *Adv. Sustainable Syst.*, 2017, **1**, 1600035.
16 S. Chen, D. Huang, P. Xu, W. Xue, L. Lei, M. Cheng, R. Wang, X. Liu and R. Deng, *J. Mater. Chem. A*, 2020, **8**, 2286–2322.
17 A. Raveendran, M. Chandran and R. Dhanusuraman, *RSC Adv.*, 2023, **13**, 3843–3876.
18 L. Tian, X. Guan, S. Zong, A. Dai and J. Qu, *Catalysts*, 2023, **13**, 355.
19 Q. Chen, G. Fan, H. Fu, Z. Li and Z. Zou, *Adv. Phys. X*, 2018, **3**, 1487267.
20 T. Hisatomi and K. Domen, *Nat. Catal.*, 2019, **2**, 387–399.
21 K. Takanabe, *ACS Catal.*, 2017, **7**, 8006–8022.
22 C. Ros, T. Andreu and J. R. Morante, *J. Mater. Chem. A*, 2020, **8**, 10625–10669.
23 B. D. Alexander, P. J. Kulesza, I. Rutkowska, R. Solarska and J. Augustynski, *J. Mater. Chem.*, 2008, **18**, 2298–2303.
24 S. Ardo, D. Fernandez Rivas, M. A. Modestino, V. Schulze Greiving, F. F. Abdi, E. Alarcon Llado, V. Artero, K. Ayers, C. Battaglia, J. P. Becker, D. Bederak, A. Berger, F. Buda, E. Chinello, B. Dam, V. Di Palma, T. Edvinsson, K. Fujii, H. Gardeniers, H. Geerlings, S. M. Hashemi, S. Haussener, F. Houle, J. Huskens, B. D. James, K. Konrad, A. Kudo, P. P. Kunturu, D. Lohse, B. Mei, E. L. Miller, G. F. Moore, J. Muller, K. L. Orchard, T. E. Rosser, F. H. Saadi, J. W. Schüttauf, B. Seger, S. W. Sheehan, W. A. Smith, J. Spurgeon, M. H. Tang, R. Van De Krol, P. C. K. Vesborg and P. Westerik, *Energy Environ. Sci.*, 2018, **11**, 2768–2783.
25 C. Jiang, S. J. A. Moniz, A. Wang, T. Zhang and J. Tang, *Chem. Soc. Rev.*, 2017, **46**, 4645–4660.
26 M. G. Walter, E. L. Warren, J. R. McKone, S. W. Boettcher, Q. Mi, E. A. Santori and N. S. Lewis, *Chem. Rev.*, 2010, **110**, 6446–6473.
27 B. D. Alexander, P. J. Kulesza, I. Rutkowska, R. Solarska and J. Augustynski, *J. Mater. Chem.*, 2008, **18**, 2298–2303.
28 T. Hisatomi and K. Domen, *Nat. Catal.*, 2019, **2**, 387–399.
29 S. K. Ghosh and H. Rahaman, *Noble Metal-Metal Oxide Hybrid Nanoparticles*, Elsevier, 2019, pp. 313–340.
30 R. Tang, S. Zhou, Z. Zhang, R. Zheng and J. Huang, *Adv. Mater.*, 2021, **33**, 2005389.

31 M. S. Prévot and K. Sivula, *J. Phys. Chem. C*, 2013, **117**, 17879–17893.
32 C. Jiang, S. J. A. Moniz, A. Wang, T. Zhang and J. Tang, *Chem. Soc. Rev.*, 2017, **46**, 4645–4660.
33 P. Hofmann, *Solid State Physics: an introduction*, 2nd edn, 2015.
34 R. J. Singh, *Solid State Physics*, Pearson, India, 1st edn, 2011.
35 H. Ibach and H. Lüth, *Solid-state physics: An introduction to principles of materials science*, Springer Berlin Heidelberg, 2010.
36 A. B. Bocarsly and H. Tachikawa, in *Laboratory Techniques in Electroanalytical Chemistry, Revised and Expanded*, ed. P. Kissinger and W. R. Heineman, Taylor and Francis Ltd., 2nd edn, 1996, pp. 855–899.
37 M. Shakeel, B. Li, M. Arif, G. Yasin, W. Rehman, A. U. Khan, S. Khan, A. Khan and J. Ali, *Appl. Catal., B*, 2018, **227**, 433–445.
38 J. W. Harder, J. M. Fontenla, P. Pilewskie, E. C. Richard and T. N. Woods, *Geophys. Res. Lett.*, 2009, **36**, L07801.
39 X. Tao, Y. Zhao, S. Wang, C. Li and R. Li, *Chem. Soc. Rev.*, 2022, **51**, 3561–3608.
40 Y. Ma, X. Wang, Y. Jia, X. Chen, H. Han and C. Li, *Chem. Rev.*, 2014, **114**, 9987–10043.
41 J. Li and N. Wu, *Catal. Sci. Technol.*, 2015, **5**, 1360–1384.
42 M. R. Nellist, F. A. L. Laskowski, F. Lin, T. J. Mills and S. W. Boettcher, *Acc. Chem. Res.*, 2016, **49**, 733–740.
43 S. M. Thalluri, L. Bai, C. Lv, Z. Huang, X. Hu and L. Liu, *Adv. Sci.*, 2020, **7**, 1902102.
44 H. Eidsvåg, S. Bentouba, P. Vajeeston, S. Yohi and D. Velauthapillai, *Molecules*, 2021, **26**, 1–30.
45 J. Low, J. Yu, M. Jaroniec, S. Wageh and A. A. Al-Ghamdi, *Adv. Mater.*, 2017, **29**, 1601694.
46 J. R. Hook and H. E. Hall, *Solid state physics*, 2nd edn, 1928.
47 Z. Chen, H. N. Dinh and E. Miller, *Photoelectrochemical Water Splitting Standards, Experimental Methods, and Protocols*, 2013.
48 B. Klahr, S. Gimenez, F. Fabregat-Santiago, J. Bisquert and T. W. Hamann, *Energy Environ. Sci.*, 2012, **5**, 7626–7636.
49 F. Spadavecchia, S. Ardizzone, G. Cappelletti, L. Falciola, M. Ceotto and D. Lotti, *J. Appl. Electrochem.*, 2013, **43**, 217–225.
50 L. M. Peter, A. B. Walker, T. Bein, A. G. Hufnagel and I. Kondofersky, *J. Electroanal. Chem.*, 2020, **872**, 114234.
51 K. Schwarzburg and F. Willig, *Appl. Phys. Lett.*, 1991, **58**, 2520–2522.
52 Z. Chen, T. F. Jaramillo, T. G. Deutsch, A. Kleiman-Shwarsctein, A. J. Forman, N. Gaillard, R. Garland, K. Takanabe, C. Heske, M. Sunkara, E. W. McFarland, K. Domen, E. L. Milled and H. N. Dinh, *J. Mater. Res.*, 2010, **25**, 3–16.
53 S. Zhang, I. Ahmet, S. H. Kim, O. Kasian, A. M. Mingers, P. Schnell, M. Kölbach, J. Lim, A. Fischer, K. J. J. Mayrhofer, S. Cherevko, B. Gault, R. Van De Krol and C. Scheu, *ACS Appl. Energy Mater.*, 2020, **3**, 9523–9527.
54 C. Y. Toe, Z. Zheng, H. Wu, J. Scott, R. Amal and Y. H. Ng, *Angew. Chem.*, 2018, **130**, 13801–13805.
55 C. Y. Toe, J. Scott, R. Amal and Y. H. Ng, *J. Photochem. Photobiol., C*, 2019, **40**, 191–211.
56 N. Pastukhova, A. Mavrič and Y. Li, *Adv. Mater. Interfaces*, 2021, **8**, 2002100.
57 F. E. Osterloh, *Chem. Mater.*, 2008, **20**, 35–54.
58 Y. J. Jang and J. S. Lee, *ChemSusChem*, 2019, **12**, 1835–1845.
59 C. Jiang, S. J. A. Moniz, A. Wang, T. Zhang and J. Tang, *Chem. Soc. Rev.*, 2017, **46**, 4645–4660.
60 K. Qi, S. Liu and A. Zada, *J. Taiwan Inst. Chem. Eng.*, 2020, **109**, 111–123.
61 P. Lianos, *Appl. Catal., B*, 2017, **210**, 235–254.
62 A. Fujishima and K. Honda, *Nature*, 1972, **238**, 37–38.
63 Z. Zhang, L. Zhang, M. N. Hedhili, H. Zhang and P. Wang, *Nano Lett.*, 2012, **13**, 14–20.
64 I. S. Cho, C. H. Lee, Y. Feng, M. Logar, P. M. Rao, L. Cai, D. R. Kim, R. Sinclair and X. Zheng, *Nat. Commun.*, 2013, **4**, 1–10.
65 M. Xu, P. Da, H. Wu, D. Zhao and G. Zheng, *Nano Lett.*, 2012, **12**, 1503–1508.
66 K. Rajeshwar, N. R. de Tacconi and C. R. Chenthamarakshan, *Chem. Mater.*, 2001, **13**, 2765–2782.
67 K. Basu, H. Zhang, H. Zhao, S. Bhattacharya, F. Navarro-Pardo, P. K. Datta, L. Jin, S. Sun, F. Vetrone and F. Rosei, *Nanoscale*, 2018, **10**, 15273–15284.
68 J. N. Tiwari, R. N. Tiwari and K. S. Kim, *Prog. Mater. Sci.*, 2012, **57**, 724–803.
69 J. Joy, J. Mathew and S. C. George, *Int. J. Hydrogen Energy*, 2018, **43**, 4804–4817.
70 O. K. Varghese and C. A. Grimes, *Sol. Energy Mater. Sol. Cells*, 2008, **92**, 374–384.
71 S. Cho, J.-W. Jang, K.-H. Lee and J. S. Lee, *APL Mater.*, 2014, **2**, 010703.
72 V. Etacheri, C. Di Valentin, J. Schneider, D. Bahnemann and S. C. Pillai, *J. Photochem. Photobiol., C*, 2015, **25**, 1–29.
73 F. Niu, D. Wang, F. Li, Y. Liu, S. Shen and T. J. Meyer, *Adv. Energy Mater.*, 2020, **10**, 1900399.
74 M. Pelaez, N. T. Nolan, S. C. Pillai, M. K. Seery, P. Falaras, A. G. Kontos, P. S. M. Dunlop, J. W. J. Hamilton, J. A. Byrne, K. O'Shea, M. H. Entezari and D. D. Dionysiou, *Appl. Catal., B*, 2012, **125**, 331–349.
75 T. Luttrell, S. Halpegamage, J. Tao, A. Kramer, E. Sutter and M. Batzill, *Sci. Rep.*, 2014, **4**, 1–8.
76 J. E. S. Haggerty, L. T. Schelhas, D. A. Kitchaev, J. S. Mangum, L. M. Garten, W. Sun, K. H. Stone, J. D. Perkins, M. F. Toney, G. Ceder, D. S. Ginley, B. P. Gorman and J. Tate, *Sci. Rep.*, 2017, **7**, 1–11.
77 X. Chen, L. Liu, P. Y. Yu and S. S. Mao, *Science*, 2011, **331**, 746–750.
78 Z. Wang, C. Yang, T. Lin, H. Yin, P. Chen, D. Wan, F. Xu, F. Huang, J. Lin, X. Xie and M. Jiang, *Energy Environ. Sci.*, 2013, **6**, 3007–3014.
79 S. Das, S. H. Kim, Y. K. Park, C. M. Choi, D. Y. Kim and Y. B. Hahn, *Mater. Chem. Phys.*, 2010, **124**, 704–708.
80 A. R. Bally, E. N. Korobeinikova, P. E. Schmid, F. Lévy and F. Bussy, *J. Phys. D: Appl. Phys.*, 1998, **31**, 1149–1154.
81 V. C. Anitha, A. N. Banerjee and S. W. Joo, *J. Mater. Sci.*, 2015, **50**, 7495–7536.

82 E. Parzinger, B. Miller, B. Blaschke, J. A. Garrido, J. W. Ager, A. Holleitner and U. Wurstbauer, *ACS Nano*, 2015, **9**, 11302–11309.
83 Z. Li, X. Meng and Z. Zhang, *J. Photochem. Photobiol., C*, 2018, **35**, 39–55.
84 A. Bak, W. Choi and H. Park, *Appl. Catal., B*, 2011, **110**, 207–215.
85 E. Kalamaras, V. Dracopoulos, L. Sygellou and P. Lianos, *Chem. Eng. J.*, 2016, **295**, 288–294.
86 P. S. Bassi, S. Y. Chiam, Gurudayal, J. Barber and L. H. Wong, *ACS Appl. Mater. Interfaces*, 2014, **6**, 22490–22495.
87 M. A. Melo, H. A. Centurion, T. T. A. Lucas, D. N. F. Muche, F. L. Souza and R. V. Gonçalves, *ACS Appl. Nano Mater.*, 2020, **3**, 9303–9317.
88 S. Kment, F. Riboni, S. Pausova, L. Wang, L. Wang, H. Han, Z. Hubicka, J. Krysa, P. Schmuki and R. Zboril, *Chem. Soc. Rev.*, 2017, **46**, 3716–3769.
89 L. Wang, N. T. Nguyen, X. Huang, P. Schmuki and Y. Bi, *Adv. Funct. Mater.*, 2017, **27**, 1703527.
90 A. Kudo, K. Ueda, H. Kato and I. Mikami, *Catal. Lett.*, 1998, **53**, 229–230.
91 Z. Li, W. Luo, M. Zhang, J. Feng and Z. Zou, *Energy Environ. Sci.*, 2013, **6**, 347–370.
92 B. S. Kalanoor, H. Seo and S. S. Kalanur, *Mater. Sci. Energy Technol.*, 2021, **4**, 317–328.
93 K. Sayama, A. Nomura, Z. Zou, R. Abe, Y. Abe and H. Arakawa, *Chem. Commun.*, 2003, 2908–2909.
94 J. Gan, X. Lu and Y. Tong, *Nanoscale*, 2014, **6**, 7142–7164.
95 X. Liu, F. Wang and Q. Wang, *Phys. Chem. Chem. Phys.*, 2012, **14**, 7894–7911.
96 S. Sfaelou, L. C. Pop, O. Monfort, V. Dracopoulos and P. Lianos, *Int. J. Hydrogen Energy*, 2016, **41**, 5902–5907.
97 M. Sarnowska, K. Bienkowski, P. J. Barczuk, R. Solarska and J. Augustynski, *Adv. Energy Mater.*, 2016, **6**, 1600526.
98 Y. H. Lai, T. C. King, D. S. Wright and E. Reisner, *Chem. – Eur. J.*, 2013, **19**, 12943–12947.
99 B. D. Alexander, P. J. Kulesza, I. Rutkowska, R. Solarska and J. Augustynski, *J. Mater. Chem.*, 2008, **18**, 2298–2303.
100 Q. Huang, Z. Ye and X. Xiao, *J. Mater. Chem. A*, 2015, **3**, 15824–15837.
101 C. G. Read, Y. Park and K. S. Choi, *J. Phys. Chem. Lett.*, 2012, **3**, 1872–1876.
102 Y. Liu, F. Le Formal, F. Boudoire, L. Yao, K. Sivula and N. Guijarro, *J. Mater. Chem. A*, 2019, **7**, 1669–1677.
103 M. S. Prévot, Y. Li, N. Guijarro and K. Sivula, *J. Mater. Chem. A*, 2016, **4**, 3018–3026.
104 S. P. Berglund, F. F. Abdi, P. Bogdanoff, A. Chemseddine, D. Friedrich and R. Van De Krol, *Chem. Mater.*, 2016, **28**, 4231–4242.
105 C. G. Morales-Guio, S. D. Tilley, H. Vrubel, M. Gratzel and X. Hu, *Nat. Commun.*, 2014, **5**, 1–7.
106 A. Paracchino, V. Laporte, K. Sivula, M. Grätzel and E. Thimsen, *Nat. Mater.*, 2011, **10**, 456–461.
107 T. Shi, Y. Feng, Y. Zhong, H. Ding, K. Chen and D. Chen, *Inorganics*, 2023, **11**, 155.
108 J. Yin, J. Jin, H. Lin, Z. Yin, J. Li, M. Lu, L. Guo, P. Xi, Y. Tang and C. Yan, *Adv. Sci.*, 2020, **7**, 1903070.
109 Y. Chen, X. Feng, M. Liu, J. Su and S. Shen, *Nanophotonics*, 2016, **5**, 524–547.
110 L. Zheng, F. Teng, X. Ye, H. Zheng and X. Fang, *Adv. Energy Mater.*, 2020, **10**, 1–32.
111 I. Y. Ahmet, J. R. Thompson and A. L. Johnson, *Eur. J. Inorg. Chem.*, 2018, 1670–1678.
112 H. Lee, W. Yang, J. Tan, J. Park, S. G. Shim, Y. S. Park, J. W. Yun, K. M. Kim and J. Moon, *ACS Appl. Mater. Interfaces*, 2020, **12**, 15155–15166.
113 I. Y. Ahmet, M. S. Hill, P. R. Raithby and A. L. Johnson, *Dalton Trans.*, 2018, **47**, 5031–5048.
114 M. Yarema, R. Caputo and M. V. Kovalenko, *Nanoscale*, 2013, **5**, 8398–8410.
115 D. V. Talapin, J. S. Lee, M. V. Kovalenko and E. V. Shevchenko, *Chem. Rev.*, 2010, **110**, 389–458.
116 M. A. Buckingham, A. L. Catherall, M. S. Hill, A. L. Johnson and J. D. Parish, *Cryst. Growth Des.*, 2017, **17**, 907–912.
117 J. A. Nasir, Z. U. Rehman, S. N. A. Shah, A. Khan, I. S. Butler and C. R. A. Catlow, *J. Mater. Chem. A*, 2020, **8**, 20752–20780.
118 A. Kolivand and S. Sharifnia, *Int. J. Energy Res.*, 2021, **45**, 2739–2752.
119 S. Han, Y. C. Pu, L. Zheng, L. Hu, J. Z. Zhang and X. Fang, *J. Mater. Chem. A*, 2016, **4**, 1078–1086.
120 L. Xu, J. Meng, J. Wang, L. Wang and Q. Li, *New J. Chem.*, 2022, **46**, 8079–8087.
121 P. Adams, F. Creazzo, T. Moehl, R. Crockett, P. Zeng, Z. Novotny, S. Luber, W. Yang and S. D. Tilley, *J. Mater. Chem. A*, 2023, **11**, 8277–8284.
122 J. Kim, W. Yang, Y. Oh, H. Lee, S. Lee, H. Shin, J. Kim and J. Moon, *J. Mater. Chem. A*, 2017, **5**, 2180–2187.
123 L. Zhang, Y. Li, C. Li, Q. Chen, Z. Zhen, X. Jiang, M. Zhong, F. Zhang and H. Zhu, *ACS Nano*, 2017, **11**, 12753–12763.
124 W. Yang, S. Lee, H. C. Kwon, J. Tan, H. Lee, J. Park, Y. Oh, H. Choi and J. Moon, *ACS Nano*, 2018, **12**, 11088–11097.
125 M. D. Khan, M. Aamir, M. Sohail, M. Sher, J. Akhtar, M. A. Malik and N. Revaprasadu, *Sol. Energy*, 2018, **169**, 526–534.
126 J. Ge, Y. Yu and Y. Yan, *ACS Energy Lett.*, 2016, **1**, 583–588.
127 J. Ge, P. J. Roland, P. Koirala, W. Meng, J. L. Young, R. Petersen, T. G. Deutsch, G. Teeter, R. J. Ellingson, R. W. Collins and Y. Yan, *Chem. Mater.*, 2017, **29**, 916–920.
128 R. B. Hall, R. W. Birkmire, J. E. Phillips and J. D. Meakin, *Appl. Phys. Lett.*, 1981, **38**, 925–926.
129 M. V. Makarova, F. Amano, S. Nomura, C. Tateishi, T. Fukuma, Y. Takahashi and Y. E. Korchev, *ACS Catal.*, 2022, **12**, 1201–1208.
130 A. Prathan, C. Bhoomanee, P. Ruankham, S. Choopun, A. Gardchareon, S. Phadungdhitidhada and D. Wongratanaphisan, *Mater. Today Proc.*, 2019, **17**, 1514–1520.
131 S. Reghunath, D. Pinheiro and K. R. Sunaja Devi, *Appl. Surf. Sci. Adv.*, 2021, **3**, 100063.
132 Y. Zhou, L. Zhang, L. Lin, B. R. Wygant, Y. Liu, Y. Zhu, Y. Zheng, C. B. Mullins, Y. Zhao, X. Zhang and G. Yu, *Nano Lett.*, 2017, **17**, 8012–8017.
133 M. Ge, C. Cao, J. Huang, S. Li, Z. Chen, K.-Q. Zhang, S. S. Al-Deyab and Y. Lai, *J. Mater. Chem. A*, 2016, **4**, 6772–6801.

134 D. Li, Y. Liu, W. Shi, C. Shao, S. Wang, C. Ding, T. Liu, F. Fan, J. Shi and C. Li, *ACS Energy Lett.*, 2019, **4**, 825–831.
135 H. S. Han, S. Shin, D. H. Kim, I. J. Park, J. S. Kim, P. S. Huang, J. K. Lee, I. S. Cho and X. Zheng, *Energy Environ. Sci.*, 2018, **11**, 1299–1306.
136 R. Li, F. Zhang, D. Wang, J. Yang, M. Li, J. Zhu, X. Zhou, H. Han and C. Li, *Nat. Commun.*, 2013, **4**, 1–7.
137 J. Pan, G. Liu, G. Q. (Max) Lu and H.-M. Cheng, *Angew. Chem., Int. Ed.*, 2011, **50**, 2133–2137.
138 T. R. Gordon, M. Cargnello, T. Paik, F. Mangolini, R. T. Weber, P. Fornasiero and C. B. Murray, *J. Am. Chem. Soc.*, 2012, **134**, 6751–6761.
139 M. Regue, S. Sibby, I. Y. Ahmet, D. Friedrich, F. F. Abdi, A. L. Johnson and S. Eslava, *J. Mater. Chem. A*, 2019, **7**, 19161–19172.
140 J. Du, M. Zhang and J. Tian, *Int. J. Miner., Metall. Mater.*, 2022, **29**, 49–58.
141 H. Kmentova, S. Kment, L. Wang, S. Pausova, T. Vaclavu, R. Kuzel, H. Han, Z. Hubicka, M. Zlamal, J. Olejnicek, M. Cada, J. Krysa and R. Zboril, *Catal. Today*, 2017, **287**, 130–136.
142 A. K. Singh and D. Sarkar, *Nanoscale*, 2018, **10**, 13130–13139.
143 T. Li, H. Jin, Z. Liang, L. Huang, Y. Lu, H. Yu, Z. Hu, J. Wu, B. Y. Xia, G. Feng and J. Zhou, *Nanoscale*, 2018, **10**, 6844–6849.
144 X. Xiao, H. Song, S. Lin, Y. Zhou, X. Zhan, Z. Hu, Q. Zhang, J. Sun, B. Yang, T. Li, L. Jiao, J. Zhou, J. Tang and Y. Gogotsi, *Nat. Commun.*, 2016, **7**, 1–8.
145 I. Vladimirov, M. Kühn, T. Geßner, F. May and R. T. Weitz, *Sci. Rep.*, 2018, **8**, 1–10.
146 J. Wang and C. Jiang, *Org. Electron.*, 2014, **16**, 164–170.
147 R. T. Weitz, K. Amsharov, U. Zschieschang, M. Burghard, M. Jansen, M. Kelsch, B. Rhamati, P. A. Van Aken, K. Kern and H. Klauk, *Chem. Mater.*, 2009, **21**, 4949–4954.
148 R. T. Weitz, K. Amsharov, U. Zschieschang, E. B. Villas, D. K. Goswami, M. Burghard, H. Dosch, M. Jansen, K. Kern and H. Klauk, *J. Am. Chem. Soc.*, 2008, **130**, 4637–4645.
149 W. Kalb, P. Lang, M. Mottaghi, H. Aubin, G. Horowitz and M. Wuttig, *Synth. Met.*, 2004, **146**, 279–282.
150 D. C. Hurum, A. G. Agrios, K. A. Gray, T. Rajh and M. C. Thurnauer, *J. Phys. Chem. B*, 2003, **107**, 4545–4549.
151 T. R. Harris-Lee, S. A. L. Johnson, L. Wang, P. J. Fletcher, J. Zhang, C. Bentley, C. R. Bowen and F. Marken, *New J. Chem.*, 2022, **46**, 8385–8392.
152 K. Sivula, *J. Phys. Chem. Lett.*, 2013, **4**, 1624–1633.
153 M. Zhong, T. Hisatomi, Y. Kuang, J. Zhao, M. Liu, A. Iwase, Q. Jia, H. Nishiyama, T. Minegishi, M. Nakabayashi, N. Shibata, R. Niishiro, C. Katayama, H. Shibano, M. Katayama, A. Kudo, T. Yamada and K. Domen, *J. Am. Chem. Soc.*, 2015, **137**, 5053–5060.
154 O. Zandi and T. W. Hamann, *J. Phys. Chem. Lett.*, 2014, **5**, 1522–1526.
155 F. Le Formal, S. R. Pendlebury, M. Cornuz, S. D. Tilley, M. Grätzel and J. R. Durrant, *J. Am. Chem. Soc.*, 2014, **136**, 2564–2574.
156 H. Lee, W. Yang, J. Tan, Y. Oh, J. Park and J. Moon, *ACS Energy Lett.*, 2019, **4**, 995–1003.
157 Y. Mi and Y. Weng, *Sci. Rep.*, 2015, **5**, 1–10.
158 Z. Zhang and J. T. Yates, *Chem. Rev.*, 2012, **112**, 5520–5551.
159 S. Chen, T. Takata and K. Domen, *Nat. Rev. Mater.*, 2017, **2**, 17050.
160 N. Bao, L. Shen, T. Takata and K. Domen, *Chem. Mater.*, 2007, **20**, 110–117.
161 H. Yan, J. Yang, G. Ma, G. Wu, X. Zong, Z. Lei, J. Shi and C. Li, *J. Catal.*, 2009, **266**, 165–168.
162 M. Liu, X. Wang, J. Liu, K. Wang, S. Jin and B. Tan, *ACS Appl. Mater. Interfaces*, 2020, **12**, 12774–12782.
163 M. Hara, J. Nunoshige, T. Takata, J. N. Kondo and K. Domen, *Chem. Commun.*, 2003, 3000–3001.
164 I. Tsuji, H. Kato and A. Kudo, *Angew. Chem., Int. Ed.*, 2005, **44**, 3565–3568.
165 K. Maeda, K. Teramura, D. Lu, N. Saito, Y. Inoue and K. Domen, *Angew. Chem., Int. Ed.*, 2006, **45**, 7806–7809.
166 H. Y. Lin, H. C. Yang and W. L. Wang, *Catal. Today*, 2011, **174**, 106–113.
167 S. Onsuratoom, T. Puangpetch and S. Chavadej, *Chem. Eng. J.*, 2011, **173**, 667–675.
168 K. Kalyanasundaram, E. Borgarello, D. Duonghong and M. Grätzel, *Angew. Chem., Int. Ed. Engl.*, 1981, **20**, 987–988.
169 K. Maeda, T. Takata, M. Hara, N. Saito, Y. Inoue, H. Kobayashi and K. Domen, *J. Am. Chem. Soc.*, 2005, **127**, 8286–8287.
170 W. J. Youngblood, S.-H. A. Lee, Y. Kobayashi, E. A. Hernandez-Pagan, P. G. Hoertz, T. A. Moore, A. L. Moore, D. Gust and T. E. Mallouk, *J. Am. Chem. Soc.*, 2009, **131**, 926–927.
171 D. K. Zhong, J. Sun, H. Inumaru and D. R. Gamelin, *J. Am. Chem. Soc.*, 2009, **131**, 6086–6087.
172 Z. Dai, Z. Guo, J. Wang, X. Zhang and J. Tu, *Metal Oxides and Related Solids for Electrocatalytic Water Splitting*, Elsevier, 2022, pp. 293–324.
173 D. K. Zhong, S. Choi and D. R. Gamelin, *J. Am. Chem. Soc.*, 2011, **133**, 18370–18377.
174 L. Francàs, S. Corby, S. Selim, D. Lee, C. A. Mesa, R. Godin, E. Pastor, I. E. L. Stephens, K. S. Choi and J. R. Durrant, *Nat. Commun.*, 2019, **10**, 1–10.
175 T. W. Kim and K. S. Choi, *Science*, 2014, **343**, 990–994.
176 Q. Shi, Q. Liu, Y. Ma, Z. Fang, Z. Liang, G. Shao, B. Tang, W. Yang, L. Qin and X. Fang, *Adv. Energy Mater.*, 2020, **10**, 1–11.
177 Y. P. Liu, S. X. Guo, L. Ding, C. A. Ohlin, A. M. Bond and J. Zhang, *ACS Appl. Mater. Interfaces*, 2015, **7**, 16632–16644.
178 B. D. B. Aaronson, J. Garoz-Ruiz, J. C. Byers, A. Colina and P. R. Unwin, *Langmuir*, 2015, **31**, 12814–12822.
179 M. Regue, I. Y. Ahmet, P. S. Bassi, A. L. Johnson, S. Fiechter, R. van de Krol, F. F. Abdi and S. Eslava, *ACS Appl. Energy Mater.*, 2020, **3**, 12066–12077.
180 M. Gao, L. Zhu, C. K. Peh and G. W. Ho, *Energy Environ. Sci.*, 2019, **12**, 841–864.
181 Z. Cai, B. Liu, X. Zou and H.-M. Cheng, *Chem. Rev.*, 2018, **118**, 6091–6133.
182 G. Talasila, S. Sachdev, U. Srivastva, D. Saxena and S. S. V. Ramakumar, *Energy Rep.*, 2020, **6**, 1963–1972.
183 V. Pasumarthi, T. Liu, M. Dupuis and C. Li, *J. Mater. Chem. A*, 2019, **7**, 3054–3065.

184 S. Sathasivam, D. S. Bhachu, Y. Lu, N. Chadwick, S. A. Althabaiti, A. O. Alyoubi, S. N. Basahel, C. J. Carmalt and I. P. Parkin, *Sci. Rep.*, 2015, **5**, 1–10.
185 D. S. Bhachu, R. G. Egdell, G. Sankar, C. J. Carmalt and I. P. Parkin, *J. Mater. Chem. C*, 2017, **5**, 9694–9701.
186 D. A. H. Hanaor and C. C. Sorrell, *J. Mater. Sci.*, 2010, **46**, 855–874.
187 X. Wang and G. Yushin, *Energy Environ. Sci.*, 2015, **8**, 1889–1904.
188 A. J. Gardecka, C. Bishop, D. Lee, S. Corby, I. P. Parkin, A. Kafizas and S. Krumdieck, *Appl. Catal., B*, 2018, **224**, 904–911.
189 S. Chen and L.-W. Wang, *Chem. Mater.*, 2012, **24**, 3659–3666.
190 J. Ran, J. Zhang, J. Yu, M. Jaroniec and S. Z. Qiao, *Chem. Soc. Rev.*, 2014, **43**, 7787–7812.
191 J. Ran, J. Yu and M. Jaroniec, *Green Chem.*, 2011, **13**, 2708–2713.
192 H. Pedersen, S. T. Barry and J. Sundqvist, *J. Vac. Sci. Technol., A*, 2021, **39**, 051001.
193 P. Marchand, I. A. Hassan, I. P. Parkin and C. J. Carmalt, *Dalton Trans.*, 2013, **42**, 9406–9422.
194 A. C. Jones and M. L. Hitchman, *Chemical Vapour Deposition: Precursors, Processes and Applications*, Royal Society of Chemistry, 2009.
195 K. L. Choy, *Prog. Mater. Sci.*, 2003, **48**, 57–170.
196 X. Hou and K. L. Choy, *Chem. Vap. Deposition*, 2006, **12**, 583–596.
197 P. Marchand, I. A. Hassan, I. P. Parkin and C. J. Carmalt, *Dalton Trans.*, 2013, **42**, 9406–9422.
198 X. Hou and K.-L. Choy, *Chem. Vap. Deposition*, 2006, **12**, 583–596.
199 S. E. Koponen, P. G. Gordon and S. T. Barry, *Polyhedron*, 2016, **108**, 59–66.
200 L. G. Hubert-Pfalzgraf, *Inorg. Chem. Commun.*, 2003, **6**, 102–120.
201 D. J. Otway and W. S. Rees, *Coord. Chem. Rev.*, 2000, **210**, 279–328.
202 J. A. Meese-Marktscheffel, R. Fukuchi, M. Kido, G. Tachibana, C. M. Jensen and J. W. Gilje, *Chem. Mater.*, 1993, **5**, 755–757.
203 J. H. Boo, S. B. Lee, S. J. Ku, W. Koh, C. Kim, K. S. Yu and Y. Kim, *Appl. Surf. Sci.*, 2001, **169–170**, 581–586.
204 S. Mathur, M. Veith, T. Ruegamer, E. Hemmer and H. Shen, *Chem. Mater.*, 2004, **16**, 1304–1312.
205 J. Auld, D. J. Houlton, A. C. Jones, S. A. Rushworth, M. A. Malik, P. O'Brien and G. W. Critchlow, *J. Mater. Chem.*, 1994, **4**, 1249–1253.
206 M. Azad Malik and P. O'Brien, *Chemical Vapour Deposition*, 2008, pp. 207–271.
207 D. C. Bock, N. C. Ou, R. O. Bonsu, C. T. Anghel, X. Su and L. McElwee-White, *Solid State Ionics*, 2018, **315**, 77–84.
208 A. P. Purdy and C. F. George, *Recent Developments in the Chemistry of Fluorinated Isopropoxides and Tertiary Butoxides*, 1994, pp. 405–420.
209 W. D. Buchanan and K. Ruhlandt-Senge, *Chem. – Eur. J.*, 2013, **19**, 10708–10715.
210 N. C. Ou, D. C. Bock, X. Su, D. Craciun, V. Craciun and L. McElwee-White, *ACS Appl. Mater. Interfaces*, 2019, **11**, 28180–28188.
211 L. Bigiani, C. Maccato, A. Gasparotto, C. Sada, E. Bontempi and D. Barreca, *Nanomaterials*, 2020, **10**, 1–13.
212 L. A. Miinea and D. M. Hoffman, *J. Mater. Chem.*, 2000, **10**, 2392–2395.
213 M. F. Mahon, K. C. Molloy, J. E. Stanley, D. W. H. Rankin, H. E. Robertson and B. F. Johnston, *Appl. Organomet. Chem.*, 2005, **19**, 658–671.
214 W. D. Buchanan, M. A. Guino-O and K. Ruhlandt-Senge, *Inorg. Chem.*, 2010, **49**, 7144–7155.
215 S. Mishra and S. Daniele, *Chem. Rev.*, 2015, **115**, 8379–8448.
216 D. B. Potter, I. P. Parkin and C. J. Carmalt, *RSC Adv.*, 2018, **8**, 33164–33173.
217 C. Edusi, G. Sankar and I. P. Parkin, *Chem. Vap. Deposition*, 2012, **18**, 126–132.
218 M. J. Powell and C. J. Carmalt, *Chem. – Eur. J.*, 2017, **23**, 15543–15552.
219 C. E. Knapp and C. J. Carmalt, *Chem. Soc. Rev.*, 2016, **45**, 1036–1064.
220 P. Brack, J. S. Sagu, T. A. N. Peiris, A. McInnes, M. Senili, K. G. U. Wijayantha, F. Marken and E. Selli, *Chem. Vap. Deposition*, 2015, **21**, 41–45.
221 N. Noor and I. P. Parkin, *J. Mater. Chem. C*, 2013, **1**, 984–996.
222 W. Maudez and K. M. Fromm, *Z. Anorg. Allg. Chem.*, 2012, **638**, 1810–1819.
223 I. M. Smallwood, *Handbook of Organic Solvent Properties*, Elsevier, 1996.
224 D. B. Potter, I. P. Parkin and C. J. Carmalt, *RSC Adv.*, 2018, **8**, 33164–33173.
225 W. N. Wang, A. Purwanto, I. W. Lenggoro, K. Okuyama, H. Chang and H. D. Jang, *Ind. Eng. Chem. Res.*, 2008, **47**, 1650–1659.
226 D. B. Potter, M. J. Powell, I. P. Parkin and C. J. Carmalt, *J. Mater. Chem. C*, 2018, **6**, 588–597.
227 J. H. Kim and S. M. Koo, *Ceram. Int.*, 2015, **41**, 37–42.
228 S. D. Jackson, D. S. Anderson, G. J. Kelly, T. Lear, D. Lennon and S. R. Watson, *Top. Catal.*, 2003, **22**, 173–182.
229 E. S. Peters, C. J. Carmalt, I. P. Parkin and D. A. Tocher, *Eur. J. Inorg. Chem.*, 2005, 4179–4185.
230 S. Basharat, C. J. Carmalt, R. Palgrave, S. A. Barnett, D. A. Tocher and H. O. Davies, *J. Organomet. Chem.*, 2008, **693**, 1787–1796.
231 S. Basharat, C. J. Carmalt, R. Binions, R. Palgrave and I. P. Parkin, *Dalton Trans.*, 2008, 591.
232 C. S. Blackman and I. P. Parkin, *Chem. Mater.*, 2005, **17**, 1583–1590.
233 S. Basharat, C. J. Carmalt, S. A. Barnett, D. A. Tocher and H. O. Davies, *Inorg. Chem.*, 2007, **46**, 9473–9480.
234 P. Marchand and C. J. Carmalt, *Coord. Chem. Rev.*, 2013, **257**, 3202–3221.
235 A. C. Jones, H. C. Aspinall and P. R. Chalker, *Surf. Coat. Technol.*, 2007, **201**, 9046–9054.
236 M. Veith, S. Mathur, A. Kareiva, M. Jilavi, M. Zimmer and V. Huch, *J. Mater. Chem.*, 1999, **9**, 3069–3079.
237 L. G. Hubert-Pfalzgraf, *Appl. Organomet. Chem.*, 1992, **6**, 627–643.
238 T. J. Boyle, R. P. Tyner, T. M. Alam, B. L. Scott, J. W. Ziller and B. G. Potter, *J. Am. Chem. Soc.*, 1999, **121**, 12104–12112.

239 W. Clegg, R. J. Errington, P. Kraxner and C. Redshaw, *J. Chem. Soc., Dalton Trans.*, 1992, **8**, 1431.
240 T. J. Boyle, R. M. Sewell, L. A. M. Ottley, H. D. Pratt, C. J. Quintana and S. D. Bunge, *Inorg. Chem.*, 2007, **46**, 1825–1835.
241 A. L. Catherall, S. Harris, M. S. Hill, A. L. Johnson and M. F. Mahon, *Cryst. Growth Des.*, 2017, **17**, 5544–5551.
242 I. Y. Ahmet, M. S. Hill, A. L. Johnson and L. M. Peter, *Chem. Mater.*, 2015, **27**, 7680–7688.
243 H. S. I. Sullivan, J. D. Parish, P. Thongchai, G. Kociok-Köhn, M. S. Hill and A. L. Johnson, *Inorg. Chem.*, 2019, **58**, 2784–2797.
244 M. A. Malik, M. Afzaal and P. O'Brien, *Chem. Rev.*, 2010, **110**, 4417–4446.
245 M. Veith, S. Mathur, N. Lecerf, V. Huch, T. Decker, H. P. Beck, W. Eiser and R. Haberkorn, *J. Sol-Gel Sci. Technol.*, 2000, **17**, 145–158.
246 M. Veith, A. Altherr and H. Wolfanger, *Chem. Vap. Deposition*, 1999, **5**, 87–90.
247 M. A. Ehsan, R. Naeem, V. McKee, A. S. Hakeem and M. Mazhar, *Sol. Energy Mater. Sol. Cells*, 2017, **161**, 328–337.
248 Y. J. Lee and S. W. Kang, *Thin Solid Films*, 2004, **446**, 227–231.
249 S. C. Buttera, D. J. Mandia and S. T. Barry, *J. Vac. Sci. Technol., A*, 2017, **35**, 01B128.
250 S. Goerke, M. Ziegler, A. Ihring, J. Dellith, A. Undisz, M. Diegel, S. Anders, U. Huebner, M. Rettenmayr and H. G. Meyer, *Appl. Surf. Sci.*, 2015, **338**, 35–41.
251 M. Broas, P. Sippola, T. Sajavaara, V. Vuorinen, A. Pyymaki Perros, H. Lipsanen and M. Paulasto-Kröckel, *J. Vac. Sci. Technol., A*, 2016, **34**, 041506.
252 S. C. Buttera, P. Rouf, P. Deminskyi, N. J. O'Brien, H. Pedersen and S. T. Barry, *Inorg. Chem.*, 2021, **60**, 11025–11031.
253 W. A. Herrmann, N. W. Huber and T. Priermeier, *Angew. Chem., Int. Ed. Engl.*, 1994, **33**, 105–107.
254 P. A. Williams, J. L. Roberts, A. C. Jones, A. C. Jones, A. C. Jones, P. R. Chalker, J. F. Bickley, A. Steiner, H. O. Davies and T. J. Leedham, *J. Mater. Chem.*, 2002, **12**, 165–167.
255 T. Wildsmith, M. S. Hill, A. L. Johnson, A. J. Kingsley and K. C. Molloy, *Chem. Commun.*, 2013, **49**, 8773–8775.
256 P. S. Kubiak, A. L. Johnson, P. J. Cameron and G. Kociok-Köhn, *Eur. J. Inorg. Chem.*, 2019, 3962–3969.
257 H. Liu, Z. Li, H. Sun and Q. Lu, *Energy Technol.*, 2020, **8**, 2000215.
258 R. Winter, M. Quinten, A. Dierstein, R. Hempelmann, A. Altherr and M. Veith, *J. Appl. Crystallogr.*, 2000, **33**, 507–510.
259 H. Lu, V. Andrei, K. J. Jenkinson, A. Regoutz, N. Li, C. E. Creissen, A. E. H. Wheatley, H. Hao, E. Reisner, D. S. Wright and S. D. Pike, *Adv. Mater.*, 2018, **30**, 1804033.
260 S. Eslava, M. McPartlin, R. I. Thomson, J. M. Rawson and D. S. Wright, *Inorg. Chem.*, 2010, **49**, 11532–11540.
261 H. Lu, D. S. Wright and S. D. Pike, *Chem. Commun.*, 2020, **56**, 854–871.
262 M. Veith, *J. Chem. Soc., Dalton Trans.*, 2002, **12**, 2405–2412.
263 M. Veith, *Prog. Phys. Chem.*, 2010, **2**, 63–81.
264 M. Regue, K. Armstrong, D. Walsh, E. Richards, A. L. Johnson and S. Eslava, *Sustainable Energy Fuels*, 2018, **2**, 2674–2686.
265 M. A. Mansoor, M. Mazhar, V. McKee and Z. Arifin, *Polyhedron*, 2014, **75**, 135–140.
266 K. Munawar, M. A. Mansoor, V. McKee, T. Zaharinie, M. N. Mohd Zubir, Z. Aspanut, F. B. Yusof and M. Mazhar, *J. Solid State Chem.*, 2020, **290**, 121552.
267 D. Graf, A. Queraltó, A. Lepcha, L. Appel, M. Frank and S. Mathur, *Sol. Energy Mater. Sol. Cells*, 2020, **210**, 110485.
268 M. Shahid, M. Hamid, A. A. Tahir, M. Mazhar, M. A. Malik and M. Helliwell, *Ind. Eng. Chem. Res.*, 2012, **51**, 16361–16368.
269 K. Munawar, M. A. Mansoor, M. M. Olmstead, T. Zaharinie, M. N. Mohd Zubir, M. Haniffa, W. J. Basirun and M. Mazhar, *Mater. Chem. Phys.*, 2020, **255**, 123220.
270 J. Slaughter, C. Coates, G. Phillips, D. Choudhury, A. D. Bond, C. P. Grey and D. S. Wright, *Inorg. Chem.*, 2022, **61**, 19203–19219.
271 V. Miikkulainen, K. Väyrynen, K. Mizohata, J. Räisänen, M. Vehkamäki and M. Ritala, *J. Vac. Sci. Technol., A*, 2019, **37**, 060911.
272 S. J. A. Moniz, C. S. Blackman, C. J. Carmalt and G. Hyett, *J. Mater. Chem.*, 2010, **20**, 7881–7886.
273 S. Mishra, E. Jeanneau, M. H. Berger, J. F. Hochepied and S. Daniele, *Inorg. Chem.*, 2010, **49**, 11184–11189.
274 D. Boegeat, B. Jousseaume, T. Toupance, G. Campet and L. Fournès, *Inorg. Chem.*, 2000, **39**, 3924–3927.
275 J. D. Parish, M. W. Snook and A. L. Johnson, *Dalton Trans.*, 2021, **50**, 13902–13914.
276 M. A. Melo, H. A. Centurion, T. T. A. Lucas, D. N. F. Muche, F. L. Souza and R. V. Gonçalves, *ACS Appl. Nano Mater.*, 2020, **3**, 9303–9317.
277 C. Li, T. Wang, Z. Luo, S. Liu and J. Gong, *Small*, 2016, **12**, 3415–3422.
278 M. Wang, X. Wu, K. Huang, Y. Sun, Y. Zhang, H. Zhang, J. He, H. Chen, J. Ding and S. Feng, *Nanoscale*, 2018, **10**, 6678–6683.
279 Y. Gao, Y. Li, G. Yang, S. Li, N. Xiao, B. Xu, S. Liu, P. Qiu, S. Hao and L. Ge, *ACS Appl. Mater. Interfaces*, 2018, **10**, 39713–39722.
280 G. Seitz, N. Penin, L. Decoux, A. Wattiaux, M. Duttine and M. Gaudon, *Inorg. Chem.*, 2016, **55**, 2499–2507.
281 K. M. Min, K. S. Park, A. H. Lim, J. C. Kim and D. W. Kim, *Ceram. Int.*, 2012, **38**, 6009–6013.
282 P. H. C. Camargo, G. G. Nunes, G. R. Friedermann, D. J. Evans, G. J. Leigh, G. Tremiliosi-Filho, E. L. De Sá, A. J. G. Zarbin and J. F. Soares, *Mater. Res. Bull.*, 2003, **38**, 1915–1928.
283 P. N. Kapoor, S. Uma, S. Rodriguez and K. J. Klabunde, *J. Mol. Catal. A: Chem.*, 2005, **229**, 145–150.
284 S. Mathur, M. Veith, H. Shen, S. Hüfner and M. H. Jilavi, *Chem. Mater.*, 2002, **14**, 568–582.
285 M. Veith, S. Mathur, N. Lecerf, K. Bartz, M. Heintz and V. Huch, *Chem. Mater.*, 2000, **12**, 271–274.
286 M. Veith and S. Kneip, *J. Mater. Sci. Lett.*, 1994, **13**, 335–337.
287 M. Veith, S. J. Kneip, A. Jungmann and S. Hofner, *Z. Anorg. Allg. Chem.*, 1997, **623**, 1507–1517.

288 T. R. Harris-Lee, E. Della Gaspera, F. Marken, J. Zhang, C. L. Bentley and A. L. Johnson, *Mater. Adv.*, 2023, **4**, 3708–3713.
289 V. Kumar, A. Govind and R. Nagarajan, *Inorg. Chem.*, 2011, **50**, 5637–5645.
290 Y. Zhao, F. T. Rabouw, T. Van Puffelen, C. A. V. Walree, D. R. Gamelin, C. De Mello Donegá and A. Meijerink, *J. Am. Chem. Soc.*, 2014, **136**, 16533–16543.
291 N. Li, P. D. Matthews, H. K. Luo and D. S. Wright, *Chem. Commun.*, 2016, **52**, 11180–11190.
292 A. Chemseddine and T. Moritz, *Eur. J. Inorg. Chem.*, 1999, 235–245.
293 A. Rammal, F. Brisach and M. Henry, *C. R. Chim.*, 2002, **5**, 59–66.
294 J. Liu, Z. Cai, Y. Lv, Y. Zhang, C. Su, M. Ouyang, C. Zhang and D. S. Wright, *J. Mater. Chem. A*, 2015, **3**, 1837–1840.
295 I. Karatchevtseva, D. J. Cassidy, Z. Zhang, G. Triani, K. S. Finnie, S. L. Cram, C. J. Barbé and J. R. Bartlett, *J. Am. Ceram. Soc.*, 2008, **91**, 2015–2023.
296 Y. Lv, M. Yao, J. P. Holgado, T. Roth, A. Steiner, L. Gan, R. M. Lambert and D. S. Wright, *RSC Adv.*, 2013, **3**, 13659–13662.
297 P. D. Matthews, T. C. King and D. S. Wright, *Chem. Commun.*, 2014, **50**, 12815–12823.
298 S. Otsuka-Yao-Matsuo, T. Omata and M. Yoshimura, *J. Alloys Compd.*, 2004, **376**, 262–267.
299 Y. Lv, Z. Cai, D. Yan, C. Su, W. Li, W. Chen, Z. Ren, Y. Wei, O. Mi, C. Zhang and D. S. Wright, *RSC Adv.*, 2015, **6**, 57–60.
300 Y. Lv, W. Du, Y. Ren, Z. Cai, K. Yu, C. Zhang, Z. Chen and D. S. Wright, *Inorg. Chem. Front.*, 2016, **3**, 1119–1123.
301 V. Riesgo-Gonzalez, S. Bhattacharjee, X. Dong, D. S. Hall, V. Andrei, A. D. Bond, C. P. Grey, E. Reisner and D. S. Wright, *Inorg. Chem.*, 2022, **61**, 6223–6233.
302 J. Tucher, L. C. Nye, I. Ivanovic-Burmazovic, A. Notarnicola and C. Streb, *Chem. – Eur. J.*, 2012, **18**, 10949–10953.
303 D. Friebel, M. W. Louie, M. Bajdich, K. E. Sanwald, Y. Cai, A. M. Wise, M. J. Cheng, D. Sokaras, T. C. Weng, R. Alonso-Mori, R. C. Davis, J. R. Bargar, J. K. Nørskov, A. Nilsson and A. T. Bell, *J. Am. Chem. Soc.*, 2015, **137**, 1305–1313.
304 Y. Liu and T. C. Lau, *J. Am. Chem. Soc.*, 2019, **141**, 3755–3766.
305 C. Feng, X. She, Y. Xiao and Y. Li, *Angew. Chem., Int. Ed.*, 2023, **62**, e202218738.
306 Y. Liu, Y. Guo, Y. Liu, Z. Wei, K. Wang and Z. Shi, *Energy Fuels*, 2023, **37**, 2608–2630.
307 M. Mohamed Abouelela, G. Kawamura and A. Matsuda, *J. Energy Chem.*, 2022, **73**, 189–213.
308 M. D. Khan, M. Aamir, M. Sohail, M. Sher, N. Baig, J. Akhtar, M. A. Malik and N. Revaprasadu, *Dalton Trans.*, 2018, **47**, 5465–5473.
309 S. Razzaque, M. D. Khan, M. Aamir, M. Sohail, S. Bhoyate, R. K. Gupta, M. Sher, J. Akhtar and N. Revaprasadu, *Inorg. Chem.*, 2021, **60**, 1449–1461.
310 Q. Wang, L. Huang, Y. Wu, G. Ma, Z. Lei and S. Ren, *Int. J. Hydrogen Energy*, 2022, **47**, 21361–21368.
311 S. L. Benjamin, C. H. De Groot, A. L. Hector, R. Huang, E. Koukharenko, W. Levason and G. Reid, *J. Mater. Chem. C*, 2015, **3**, 423–430.
312 M. Regue, K. Armstrong, D. Walsh, E. Richards, A. L. Johnson and S. Eslava, *Sustainable Energy Fuels*, 2018, **2**, 2674–2686.
313 J. Le Hou, W. Luo, Y. Y. Wu, H. C. Su, G. L. Zhang, Q. Y. Zhu and J. Dai, *Dalton Trans.*, 2015, **44**, 19829–19835.
314 S. Eslava, A. Reynal, V. G. Rocha, S. Barg and E. Saiz, *J. Mater. Chem. A*, 2016, **4**, 7200–7206.
315 T. J. Boyle, B. A. Hernandez-Sanchez, C. M. Baros, L. N. Brewer and M. A. Rodriguez, *Chem. Mater.*, 2007, **19**, 2016–2026.
316 H. Gerung, T. J. Boyle, L. J. Tribby, S. D. Bunge, C. J. Brinker and S. M. Han, *J. Am. Chem. Soc.*, 2006, **128**, 5244–5250.
317 H. Gerung, S. D. Bunge, T. J. Boyle, C. J. Brinker and S. M. Han, *Chem. Commun.*, 2005, 1914.
318 S. Panigrahi and T. Pal, *Chemtracts*, 2005, **18**, 112–119.
319 T. J. Boyle, S. D. Bunge, N. L. Andrews, L. E. Matzen, K. Sieg, M. A. Rodriguez and T. J. Headley, *Chem. Mater.*, 2004, **16**, 3279–3288.
320 W. W. Yu, Y. A. Wang and X. Peng, *Chem. Mater.*, 2003, **15**, 4300–4308.
321 Z. Pan, W. Peng, F. Li and Y. He, *Adv. Funct. Mater.*, 2018, **28**, 1706897.
322 S. J. A. Moniz, S. A. Shevlin, D. J. Martin, Z.-X. Guo and J. Tang, *Energy Environ. Sci.*, 2015, **8**, 731–759.
323 R. Marschall, *Adv. Funct. Mater.*, 2014, **24**, 2421–2440.
324 H. Van Bui, F. Grillo and J. R. Van Ommen, *Chem. Commun.*, 2017, **53**, 45–71.
325 R. W. Johnson, A. Hultqvist and S. F. Bent, *Mater. Today*, 2014, **17**, 236–246.
326 V. Cremers, R. L. Puurunen and J. Dendooven, *Appl. Phys. Rev.*, 2019, **6**, 021302.
327 J. W. F. Innocent, M. Napari, A. L. Johnson, T. R. Harris-Lee, M. Regue, T. Sajavaara, J. L. MacManus-Driscoll, F. Marken and F. Alkhalil, *Mater. Adv.*, 2021, **2**, 273–279.
328 D. Barreca, G. Carraro, A. Gasparotto, C. Maccato, M. E. A. Warwick, K. Kaunisto, C. Sada, S. Turner, Y. Gönüllü, T.-P. Ruoko, L. Borgese, E. Bontempi, G. Van Tendeloo, H. Lemmetyinen and S. Mathur, *Adv. Mater. Interfaces*, 2015, **2**, 1500313.
329 J. Deng, Q. Zhuo and X. Lv, *J. Electroanal. Chem.*, 2019, **835**, 287–292.
330 C. Li, T. Wang, Z. Luo, S. Liu and J. Gong, *Small*, 2016, **12**, 3415–3422.
331 J. H. Kim, Y. Jo, J. H. Kim, J. W. Jang, H. J. Kang, Y. H. Lee, D. S. Kim, Y. Jun and J. S. Lee, *ACS Nano*, 2015, **9**, 11820–11829.
332 B. Y. Cheng, J. S. Yang, H. W. Cho and J. J. Wu, *ACS Appl. Mater. Interfaces*, 2016, **8**, 20032–20039.
333 P. Stathi, M. Solakidou and Y. Deligiannakis, *Nanomaterials*, 2021, **11**, 1–15.
334 M. Rohloff, B. Anke, O. Kasian, S. Zhang, M. Lerch, C. Scheu and A. Fischer, *ACS Appl. Mater. Interfaces*, 2019, **11**, 16430–16442.
335 Y. Tang and W. Cheng, *Sci. Adv. Mater.*, 2012, **4**, 784–797.
336 E. Mustafa, E. A. Dawi, Z. H. Ibupoto, A. M. M. Ibrahim, A. Elsukova, X. Liu, A. Tahira, R. E. Adam, M. Willander and O. Nur, *RSC Adv.*, 2023, **13**, 11297–11310.
337 Z. Zhao, D. E. Schipper, A. P. Leitner, H. Thirumalai, J. H. Chen, L. Xie, F. Qin, M. K. Alam, L. C. Grabow, S. Chen, D. Wang, Z. Ren, Z. Wang, K. H. Whitmire and J. Bao, *Nano Energy*, 2017, **39**, 444–453.

338 L. Tong, W. Wu, K. Kuepper, A. Scheurer and K. Meyer, *ChemSusChem*, 2018, **11**, 2752–2757.
339 N. Boysen, J. L. Wree, D. Zanders, D. Rogalla, D. Öhl, W. Schuhmann and A. Devi, *ACS Appl. Mater. Interfaces*, 2022, **14**, 52149–52162.
340 P. Ji, X. Feng, P. Oliveres, Z. Li, A. Murakami, C. Wang and W. Lin, *J. Am. Chem. Soc.*, 2019, **141**, 14878–14888.
341 J. E. Rorrer, F. D. Toste and A. T. Bell, *ACS Catal.*, 2019, **9**, 10588–10604.
342 H. A. Centurion, M. A. Melo, L. G. Rabelo, G. A. S. Alves, W. S. Rosa, I. Rodríguez-Gutiérrez, F. L. Souza and R. V. Gonçalves, *J. Alloys Compd.*, 2023, **933**, 167710.
343 W. Wang, M. Xu, X. Xu, W. Zhou and Z. Shao, *Angew. Chem., Int. Ed.*, 2020, **59**, 136–152.
344 M. Thangamuthu, Q. Ruan, P. O. Ohemeng, B. Luo, D. Jing, R. Godin and J. Tang, *Chem. Rev.*, 2022, **122**, 11778–11829.
345 R. R. Katzbaer, M. J. Theibault, N. E. Kirchner-Hall, Z. Mao, I. Dabo, H. D. Abruña and R. E. Schaak, *Adv. Energy Mater.*, 2022, **12**, 1–12.
346 I. E. Castelli, D. D. Landis, K. S. Thygesen, S. Dahl, I. Chorkendorff, T. F. Jaramillo and K. W. Jacobsen, *Energy Environ. Sci.*, 2012, **5**, 9034–9043.
347 J. E. Park, Z. J. L. Bare, R. J. Morelock, M. A. Rodriguez, A. Ambrosini, C. B. Musgrave, A. H. McDaniel and E. N. Coker, *Front. Energy Res.*, 2021, **9**, 1–8.
348 M. A. Buckingham, B. Ward-O'Brien, W. Xiao, Y. Li, J. Qu and D. J. Lewis, *Chem. Commun.*, 2022, **58**, 8025–8037.
349 M. A. Buckingham, J. M. Skelton and D. J. Lewis, *Cryst. Growth Des.*, 2023, DOI: **10.1021/acs.cgd.3c00712**.
350 J. Qu, A. Elgendy, R. Cai, M. A. Buckingham, A. A. Papaderakis, H. de Latour, K. Hazeldine, G. F. S. Whitehead, F. Alam, C. T. Smith, D. J. Binks, A. Walton, J. M. Skelton, R. A. W. Dryfe, S. J. Haigh and D. J. Lewis, *Adv. Sci.*, 2023, **10**, 1–11.
351 R. Mohili, N. R. Hemanth, H. Jin, K. Lee and N. Chaudhari, *J. Mater. Chem. A*, 2023, **11**, 10463–10472.
352 D. Lai, Q. Kang, F. Gao and Q. Lu, *J. Mater. Chem. A*, 2021, **9**, 17913–17922.